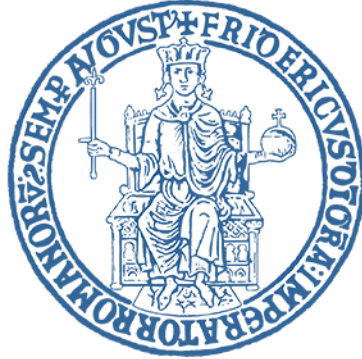


**UNIVERSITÀ DEGLI STUDI DI NAPOLI**  
**“FEDERICO II”**



**Scuola Politecnica e delle Scienze di Base**

**Area Didattica di Scienze Matematiche Fisiche e Naturali**

**Dipartimento di Fisica “Ettore Pancini”**

*Laurea Magistrale in Fisica*

**Design and characterization of dissipationless and  
tunable devices for read-out of superconducting qubits**

**Relatori:**

Prof. Francesco Tafuri

Dr. Davide Massarotti

Dr. Marco Arzeo

**Candidato:**

Pasquale Mastrovito

Matr. N94000571

**Anno Accademico 2020/2021**

# Introduction

In the last decade the properties of superconducting quantum bits have improved enormously, allowing the realization of the first quantum processors [1]. It now becomes of central importance to make a step further by focusing on two crucial points: the scalability of quantum processors and the implementation of an active quantum control framework that allows a dynamic readout of the qubits ensemble during the computational process [2]. In order to achieve both these goals, it is essential to design new quantum devices able to perform such tasks without inflating the number of operations required.

This thesis work fits in this context by introducing an innovative superconducting quantum circuit, called Josephson Digital Phase Detector (JDPD), that introduces a new way to perform Quantum Non Demolition (QND) qubit readout. This new technique, with respect to current procedures, has the potential to improve significantly the scalability. The proposed circuit, in principle, is capable of digitalize the measurement of the qubit state in the same cold environment that contains the qubits ensemble. This feature allows to partially remove the components needed for the dynamic communication between the qubits and the measurement setup at room temperature, which is a key step for the implementation of more compact and efficient control architecture based on superconducting Rapid Single Flux Quantum (RSFQ) electronics [3–6]. This type of solution is essential towards the construction of a fault-tolerant quantum computer [7], given the unavoidable fragility of the quantum states describing the qubits due to decoherence and environment noise effects. In this context, the JDPD device represents a strong example of how the physics of superconducting circuits and of Josephson junctions is the key to address specific tasks in a quantum architecture.

This thesis work represents the first step towards the implementation of the JDPD as a read-out device in a quantum computer architecture. In particular, in this thesis work I have focused on the dynamics of the JDPD with the specific aim of validating the JDPD capability of performing QND read-out of superconducting qubits. The validation has been performed by studying two different JDPD by performing different simulations through different tools (Python scripts, Software simulators). Such simulations prove the feasibility of the QND read-out protocol allowed by the JDPD and create a bridge between the analytical model that describes the circuits dynamics

and the experimental data acquired during the measurements. By comparing the data with the simulations I have experimentally validated the analytical model on which the read-out protocol is based on, thus achieving the prefixed goal of proving the capability of the JDPD to perform superconducting qubit read-out.

The thesis is organized as follows: in the first chapter I will give a brief general description of superconducting quantum circuits and I will define the dynamics of some fundamental superconducting quantum circuits, such as the LC oscillator, the DC SQUID and the superconducting qubit, which allow to better understand the world of quantum circuits. In the second chapter I will deal with superconducting qubit read-out. In particular I will describe how QND read-out can be performed by coupling a microwave cavity to the qubit under test. Moreover, some common read-out techniques that exploit this method will be discussed. Among the various techniques I will introduce also the JDPD and the corresponding read-out protocol. In the third chapter I will illustrate the experimental protocol to study the JDPD dynamics, which is based on performing transmittivity/reflectivity measurements of a circuit that I will call "spectroscopy circuit". The second part of the chapter will focus on the description of the cryogenic and electronic experimental setup to perform the different required operations. In the fourth chapter I will describe all the simulations that I have performed for an accurate design of the JDPD device. The first part of the chapter will focus on the preliminary simulations to prove the possibility of performing QND read-out with the JDPD. The second part deals with the simulations to characterize the spectroscopy circuit component in order to design devices that can be analysed with the available experimental setup. The third part will briefly describe the final designs of the chips. The last part will illustrate further simulations that I have performed to predict the behaviour of the spectroscopy circuit, as a term of reference between the spectroscopy measurements and the JDPD dynamics. In the fifth and final chapter I will outline the various steps and I will show the experimental measurements that allow to validate the capability of the JDPD to perform QND read-out of superconducting qubits.

# Chapter 1

## Introduction to superconducting quantum circuits

In this Chapter I will introduce the fundamental features of superconducting quantum circuits. The first paragraph provides the mathematical formalism employed to study the behaviour of superconducting circuits both in classical and quantum regime. In the second paragraph the main properties of superconducting devices are highlighted, with a special focus on phase-sensitive experiments. In the third and fourth paragraphs an overview of the main superconducting quantum circuits and their use as quantum bits (qubits) will be presented.

### 1.1 Quantum circuits

Quantum mechanics is commonly used for the description of microscopic particles such as electrons, atoms or photons. More recently, thanks to the impressive developments in the fields of superconductivity, material science and nano-fabrication, quantum mechanics has gained additional significance even in the description of macroscopic entities and in the design of innovative devices and circuits [8] [9]. All this paves the way to a multitude of new inspiring applications, in which quantum circuits are commonly employed as the core element of quantum processors, as quantum bits (qubits) [1] [10] [11], as devices to detect the quantum state (read-out devices) [12] [13] [14] or as quantum amplifiers for signal coming from a quantum system [15].

To describe how quantum circuits behave it is useful to start from the classical ones. An electromagnetic circuit is made of multiple branches mutually interconnected and containing different circuital elements. The elements of each branch  $b$  at a time  $t$  are characterized by two variables: the voltage  $V_b(t)$  across the element and the current  $I_b(t)$  flowing through it. The voltage and the current are defined from the underlying electromagnetic fields by the following expressions:

$$V_b(t) = \int_{b_{start}}^{b_{end}} \vec{E}(\vec{r}, t) \cdot d\vec{l} \quad (1.1)$$

$$I_b(t) = \frac{1}{\mu_0} \oint_{b_{around}} \vec{B}(\vec{r}, t) \cdot d\vec{l} \quad (1.2)$$

Considering integral paths such that one field is approximately zero on the integration path related to the other field, the voltages and the currents can be assumed independent [16]. In this approximation it is possible to solve the circuits through the well known classical electromagnetic laws. For a quantum treatment it is useful to introduce the Hamiltonian description of a circuit [16]. An Hamiltonian description of electrical circuits requires the introduction of branch fluxes and branch charges which are defined by branch voltages and branch currents through the equations [16]:

$$\Phi_b(t) = \int_0^t V(t') dt' \quad (1.3)$$

$$Q_b(t) = \int_0^t I(t') dt' \quad (1.4)$$

where at  $t = 0$  the circuit voltages and currents are supposed to be zero. These variables are correlated through the Kirchoff's laws:

$$\sum_{b_l \text{ around } l} \Phi_b = \Phi_l \quad (1.5)$$

$$\sum_{b_l \text{ to } l} Q_b = Q_l \quad (1.6)$$

where  $l$  represents the node in the circuit and  $b_l$  the branches around  $l$  in Eq. 1.5 and the branches to the node  $l$  in Eq. 1.6. This formalism allows to give a general analytical description of capacitive and inductive elements through the canonical variables. A capacitive element will be a dispersive element for which the voltage  $V(t)$  is a function only of the charge  $Q(t)$  and not directly of the time  $t$  or of any other variables:  $V(t) = f(Q(t))$ . The capacitance is thus defined in the following way:

$$C(Q) = \left[ \frac{df}{dQ} \right]^{-1} \quad (1.7)$$

Similarly, an inductive element is a dispersive element for which the current  $I(t)$  is a function only of the flux  $\Phi(t)$  and not directly of the time  $t$  or any other variables,  $I(t) = g(\Phi(t))$ . The inductance will depend only on the flux  $\Phi(t)$  through the following expression:

$$L(\Phi) = \left[ \frac{dg}{d\Phi} \right]^{-1} \quad (1.8)$$

In the case of linear components where capacitance and inductance can be considered constant ( $C(Q) = C$ ,  $L(\Phi) = L$ ), the relative electromagnetic energy is well defined by the following expressions:

Linear Capacity	$\frac{(Q-Q_{offset})^2}{2C}$
Linear Inductance	$\frac{(\Phi-\Phi_{offset})^2}{2L}$

From the relations between branch quantities and node quantities it is possible to find some superfluous variables and thus to reduce the number of the effective degrees of freedom of the system. Two standard methods in circuit theory are commonly used to this aim: the method of nodes and the method of loops. In this discussion I will use the former in order to solve most practical problems. The capacitive sub-network is approximated to contain only linear elements [16]. This is a reasonable assumption for the circuits discussed in this work, given their simplicity. This assumption allows to express the energy associated to a capacitance in terms of voltage, i.e. the derivative of flux. As a consequence, the energy of a capacitive branch can be written as  $E_C = C\dot{\Phi}^2/2$ . The symmetry between charge and flux is thus broken, and it is possible to obtain one from the other [16]. In this case it is possible to introduce a semi-classical model where  $E_C$  can be seen as the kinetic energy of the system and thus the flux becomes a position-like degree of freedom that defines the dynamics of the system. Within this framework it can be introduced a Lagrangian description of the circuits, where the Lagrangian is a function of the fluxes  $\Phi_n$  across the branches and of their derivatives:  $\mathcal{L}(\{\Phi_n\}, \{\dot{\Phi}_n\})$ . From the Lagrangian description it is possible to pass to an Hamiltonian description, where the momenta conjugate of the fluxes is defined by the branch charge:

$$q_n = \frac{\delta \mathcal{L}}{\delta \dot{\Phi}_n}$$

It can be seen that in this context the momentum conjugate is linked to the charge in the branch  $n$  [16]. The Hamiltonian of a circuit can thus be expressed as the sum of the kinetic energy, which has to be expressed in terms of the charge and the equivalent capacity, plus the potential energy expressed in terms of the flux  $\Phi_n$  on the branches and the equivalent inductance, where the index  $n$  represents the branch  $n$  in the circuit. In this model the dynamics of the circuit follows the Hamilton-Jacobi equations:

$$\dot{\Phi}_n = \frac{\delta H}{\delta q_n} \tag{1.9}$$

$$\dot{q}_n = -\frac{\delta H}{\delta \Phi_n} \tag{1.10}$$

The passage from the classical to the quantum description of electrical circuit is achieved by replacing the classical variables with the corresponding operators, leading to an Hamiltonian that is defined by a function of operators:

$$\Phi \rightarrow \hat{\Phi}$$

$$Q \rightarrow \hat{Q}$$

$$H \rightarrow \hat{H}$$

The state of the circuit is likewise represented by the density operator, which lives in the Hilbert space related to the system through a well defined Hamiltonian. In the quantum mechanical description, the dynamical variables  $\{\Phi_n\}$  and  $\{Q_n\}$ , that describe the state of the system, are characterized by the following commutation relations:

$$[\hat{\Phi}_n, \hat{Q}_m] = i\hbar\delta_{nm} \quad (1.11)$$

$$[\hat{\Phi}_n, \hat{\Phi}_m] = 0 \quad (1.12)$$

$$[\hat{Q}_n, \hat{Q}_m] = 0 \quad (1.13)$$

These relations lead to fluctuations of charge and flux in quantum circuits that depend on the temperature of the system.

## 1.2 Superconductivity, Josephson junctions and phase-sensitive effects

In the context of quantum circuits, the superconductivity turns out to be a fundamental ingredient. This particular state, which occurs below a critical temperature  $T_c$ , characteristic of each material [17], is the manifestation of quantum mechanics at a macroscopic level. In the more standard case of low critical temperature superconductors, such as niobium employed in this work, a general theoretical description of superconductivity is based on Bardeen-Cooper-Schrieffer (BCS) microscopic theory [17]. In a few words, the superconducting phase can be described as a state where the electrons in the system tend to couple in the form of spin-singlet pairs due to the phonon interaction that prevails on the electron-electron interaction. This can be phenomenologically understood by considering an electron moving in a lattice. As it is negatively charged, its movement exerts a force on the positively charged ions, which then slightly move towards the electron. The other electron follows the movement of the ions towards the first electron. Thus, an effectively attractive interaction is created which leads to the formation of electron pairs, called "Cooper pairs" [18]. Cooper pairs form a condensate, that can be described by a macroscopic wavefunction  $\psi = |\psi|e^{i\varphi}$ , where  $|\psi|^2$  represents the density of Cooper pairs and  $\varphi$  the phase of the condensate [9]. The two features of the superconducting state are: zero resistance and perfect diamagnetism, also called Meissner effect. All other properties derive from these two and are well explained by BCS theory. Among the others, magnetic flux quantization [19] is a remarkable example of quantization of macroscopic quantities. Consider a ring-shaped superconductor inside a magnetic field that cross the loop. By cooling down the ring below the critical temperature of the superconductor, a condensate of Cooper pairs travel without resistance along the ring, developing a supercurrent that force the magnetic field out of the material, due to the Meissner effect. The generated current will permanently trap some of the magnetic field, even when the external field is removed. This trapped magnetic flux is quantized, and in particular it will always be a multiple of  $\Phi_0 = h/2e$ , called the magnetic flux quantum:

$$\Phi_B = n \frac{h}{2e} = n\Phi_0 \quad n \in \mathbb{N} \quad (1.14)$$

Other intriguing phenomena arise when two superconductors are weakly coupled through a sufficiently thin non superconducting barrier, of the order of 1 or a few  $nm$ , forming a junction. After the system has been cooled down to temperature below the critical temperature of the superconductor that compose the junction, Cooper pairs

can coherently tunnel through it, keeping memory of the phase difference of the two condensates composing the junction. This phenomenon was discovered by Brian Josephson in 1962 (Josephson effect) [20] [21] and, as we will see in the rest of my work, is the core of modern superconducting and quantum technologies. This junction, that exhibits this peculiar phenomenon is called a Josephson junction, depicted schematically in Fig. 1.1. The Josephson fundamental relations are [20]:

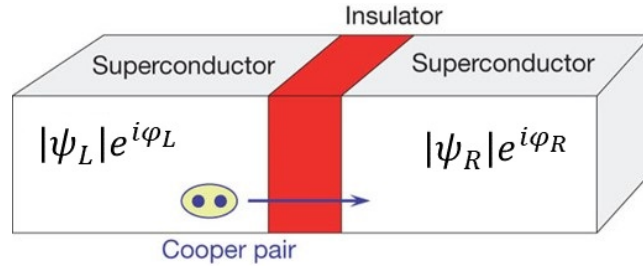


FIGURE 1.1: Typical sketch of a tunnel Josephson junction with an insulating barrier.  $\psi_L = |\psi_L|e^{i\varphi_L}$  and  $\psi_R = |\psi_R|e^{i\varphi_R}$  are the left and right macroscopic wave functions, respectively

$$I_S(\varphi) = I_C \sin(\varphi) \quad (1.15)$$

$$V = \frac{\hbar}{2e} \frac{d\varphi}{dt} = \frac{\Phi_0}{2\pi} \frac{d\varphi}{dt} \quad (1.16)$$

where  $\varphi = \varphi_L - \varphi_R$  is the phase difference between the phases of the two macroscopic wavefunctions and  $V$  is the voltage drop across the junction. In Eq. 1.15, 1.16 it is shown that below a threshold value known as critical current  $I_C$ , the junction manifest a current  $I_S(\varphi)$ , called "supercurrent", without any voltage drop across the junction. The supercurrent is related to the phase difference  $\varphi$  between the phases of the two macroscopic wave functions according to Eq. 1.15. This means that the phase difference across the Josephson junction becomes a *new observable* quantity. Josephson junctions thus represent unique devices to build phase-detection experiments, which are of great impact and utility in superconducting quantum circuits [22] [21]. Considering Eq. 1.16 and the Faraday's law, in a branch that contains a Josephson junction, the phase difference  $\varphi$  across the junction and the flux  $\Phi$  across the branch are linked through the following relation:

$$\Phi = \frac{\Phi_0}{2\pi} \varphi \quad (1.17)$$

Therefore, given the role of the flux in the mechanical analog introduced in the previous section, the Josephson junctions allow to use the phase difference as a new positional degree of freedom, instead of the branches flux. Thus the dynamics of superconducting quantum circuits containing Josephson junctions is defined by the

evolution of the phase difference, which in turn is linked to the canonical electric variable by the two Josephson equations 1.15 1.16.

An effective way to represent the evolution of the system in this context is to introduce the concept of the "phase particle". According to the resistively and capacitively shunted junction (RCSJ) model [20], a current biased Josephson junction can be described by the analog circuit reported in Fig. 1.2(a) where the total current  $I$  is given by the sum of: the tunneling supercurrent  $I_S = I_C \sin(\varphi)$ , the quasi-particle current  $I_n = V/R_n$  that develops in the resistive regime and the displacement current  $I_D = CdV/dt$  due to the capacitance associated to the junction.

$$I = I_S + I_N + I_D \quad (1.18)$$

By applying Eq. 1.15 - 1.17, the Eq. 1.19 that describes the dynamic of the phase difference  $\varphi$  across the junction is obtained [20]:

$$\frac{\Phi_0}{2\pi} C \frac{d^2 \varphi}{dt^2} + \frac{\Phi_0}{2\pi} \frac{1}{R} \frac{d\varphi}{dt} + I_C \sin(\varphi) - I = 0 \quad (1.19)$$

The latter equation points out that the phase dynamics of a current biased Josephson junction is analog to the dynamics of a damped pendulum inside a potential defined as follows:

$$U(\varphi, I) = -\frac{\Phi_0}{2\pi} (I_C \cos(\varphi) + I\varphi) = -E_J (\cos(\varphi) + I\varphi) \quad (1.20)$$

where  $E_J$  is the Josephson energy [21]. The potential  $U(\varphi, I)$  in Eq. 1.20 is called "wash-board potential" due to its peculiar form shown in Fig. 1.2. The phase difference across the Josephson junction can thus be represented by a virtual particle, called phase particle, that slides along the wash-board potential. This concept can be extended to any superconducting quantum circuit containing Josephson junctions, where the phase difference across the branches of the system can be represented by the position of the phase particle in the manifold that represents the potential energy of the circuit [20]. In the context of superconducting quantum circuits, the potential energy is linked to their inductance framework, as previously mentioned. The Josephson junction inside the quantum circuit adds a non linear contribute to the equivalent inductance of the system. Josephson junctions, in fact, represent circuitual elements with a non linear inductance, due to the current-phase relation reported in Eq. 1.15, which brings to the following expression of the Josephson inductance:

$$L(\varphi) = \frac{\Phi_0}{2\pi I_C \cos(\varphi)} \quad (1.21)$$

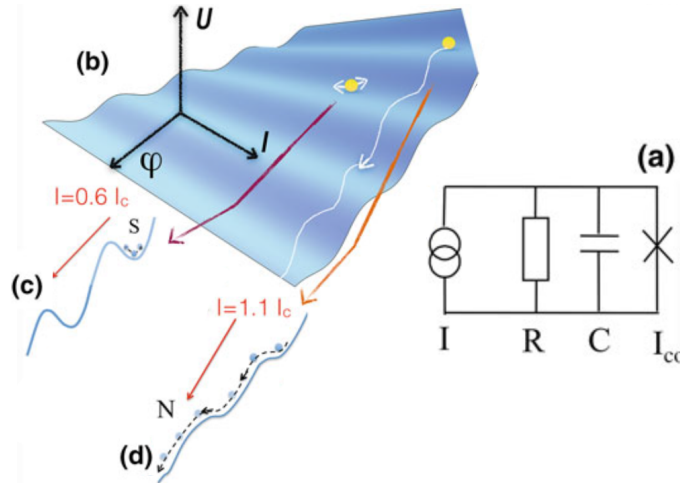


FIGURE 1.2: (a) Equivalent circuit of a current biased Josephson junction according to the RCSJ model. (b) Washboard potential for different values of the bias current. (c) and (d) two dimensional projections for two different values of the bias current ( $0.6I_c$  and  $1.1I_c$ ). [20]

Such a non linear behaviour of the Josephson junction introduces a non linear effective potential in superconducting circuits, as partly illustrated in Fig. 1.2. Through an adequate architecture it is possible to fabricate circuits with very particular potentials and thus capable of behaving in many different ways. In addition the Josephson inductance can be also tuned by an external magnetic field. This peculiarity is a direct consequence of the superconducting regime where the critical current is sensitive to external magnetic fields [18]. A magnetic field parallel to the insulating barrier surface causes a spatial modulation of the supercurrent density along the direction perpendicular to the magnetic field and parallel to insulating barrier surface, which ultimately leads to a modulation of the junction critical current  $I_C$  with respect to the applied magnetic field [20]. Thus the critical current can be tuned by means of an external magnetic field, leading to a tunable junction inductance thanks to its dependence from  $I_C$ , as highlighted by Eq. 1.21. In conclusion the Josephson junctions allow to design circuitual systems with very peculiar and tunable dynamic, being the fundamental cell of superconducting electronics and of superconducting quantum circuits.

## 1.3 Basic superconducting quantum circuits

In order to better understand the dynamics of superconducting quantum circuits, it is useful to introduce some specific devices fundamental for this work, which are: LC oscillator and DC Superconducting Quantum Interference Devices (SQUID).

### 1.3.1 LC oscillator

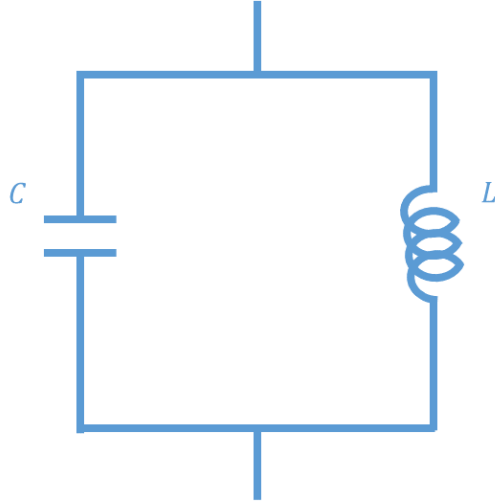


FIGURE 1.3: LC oscillator circuit

LC circuits are defined by the following Hamiltonian:

$$\hat{H} = \frac{\hat{Q}^2}{2C} + \frac{\hat{\Phi}^2}{2L} \quad (1.22)$$

This Hamiltonian resembles the form of the quantum harmonic oscillator with the differences that the canonical operators of position and momentum are replaced by the flux  $\hat{\Phi}$  and the charge  $\hat{Q}$ , respectively, while the capacitance  $C$  and the inductance  $L$  play the role of inertial mass and elastic constant, respectively. It is possible to solve this system in the same way as for the canonic quantum harmonic oscillator by introducing the ladder operators  $\hat{c}$ ,  $\hat{c}^\dagger$  defined by the following relations [16]:

$$\hat{\Phi} = \sqrt{\frac{\hbar Z_0}{2}} (\hat{c} + \hat{c}^\dagger) \quad (1.23)$$

$$\hat{Q} = \frac{1}{i} \sqrt{\frac{\hbar}{2Z_0}} (\hat{c} - \hat{c}^\dagger) \quad (1.24)$$

where  $Z_0 = \sqrt{\frac{L}{C}}$  is the impedance of the circuit. Moreover, it is possible to demonstrate that the ladder operators satisfy the following commutation rule:

$$[\hat{c}, \hat{c}^\dagger] = 1 \quad (1.25)$$

By using Eq 1.23, 1.24 the Hamiltonian in Eq. 1.22 can be rewritten in terms of the ladder operators:

$$\hat{H} = \frac{\hbar}{\sqrt{LC}} \left( \hat{c}^\dagger \hat{c} + \frac{1}{2} \right) = \hbar\omega \left( \hat{c}^\dagger \hat{c} + \frac{1}{2} \right) \quad (1.26)$$

where  $\omega = \sqrt{\frac{1}{LC}}$  is the resonant frequency of the circuit. The quantum behaviour of this circuit shows up in the context of quantum fluctuations of charge and flux. For  $T = 0$  in fact the two degrees of freedom of the system will be characterised by the following expressions:

$$\langle \hat{\Phi}^2 \rangle_0 = \langle 0 | \hbar Z_0 (\hat{c} \hat{c}^\dagger) | 0 \rangle = \hbar Z_0 \quad (1.27)$$

$$\langle \hat{Q}^2 \rangle_0 = \langle 0 | \frac{\hbar}{Z_0} (\hat{c} \hat{c}^\dagger) | 0 \rangle = \frac{\hbar}{Z_0} \quad (1.28)$$

while in the case  $T \neq 0$  the fluctuations will depend on the temperature of the system according to the following relations:

$$\langle \hat{\Phi}^2 \rangle_0 = \frac{\hbar Z_0}{2} \coth \left( \frac{\hbar \omega_0}{2k_B T} \right) \quad (1.29)$$

$$\langle \hat{Q}^2 \rangle_0 = \frac{\hbar}{Z_0 2} \coth \left( \frac{\hbar \omega_0}{2k_B T} \right) \quad (1.30)$$

In the context of superconducting circuits it is important to beware of spurious LC oscillators that can arise from unexpected couplings between the inductances and capacitances inside the circuit layout. These undesired LC oscillators add spurious resonances to the reflectance/transmittivity trend of the superconducting circuit under test at frequencies equal to the resonance frequency  $\omega_0$  of the LC oscillators. The latter feature can significantly perturb the spectroscopy of the superconducting circuit under test depending on the resonances width, that is directly linked to undesired photons losses. These spurious LC oscillators are also potential noise sources in the dynamics of the superconducting quantum circuit under test. The quantum fluctuations reported in Eq. 1.29, 1.30 can in fact bring decoherence effects that inevitably lead to a relaxation of the quantum behaviour of the whole circuit. At the same time, in the context of superconducting circuit design the quantum fluctuations of the LC oscillator are not just a negative effect but can be also employed in a controlled way

to couple electronic devices, such as qubits and electromagnetic cavities [13].

### 1.3.2 DC SQUID

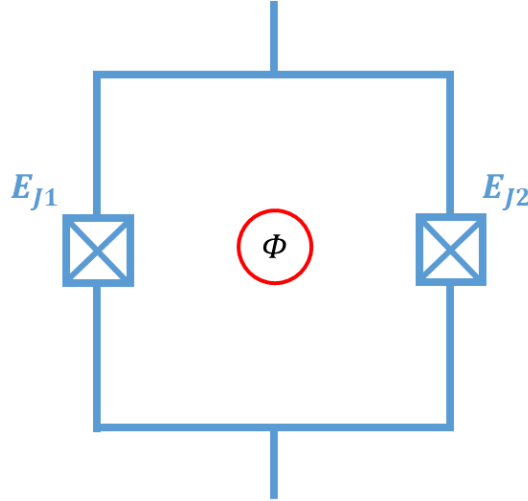


FIGURE 1.4: SQUID circuit. The crossed squares on the sides represent two Josephson junctions of Josephson energy  $E_{J1}$  and  $E_{J2}$ . The circuit can be probed by a current source that provides a bias current  $I$  to the SQUID and also manipulated through an external magnetic flux  $\Phi$  across the central loop.

The DC SQUID consists of two Josephson tunnel junctions in parallel forming a loop threaded by a flux  $\Phi_{ext}$ . In order to write the Hamiltonian of this circuit it is first necessary to evaluate the energy of Josephson junctions. The junctions store magnetic energy that can be evaluated on the basis of the characteristic relations in Eq. 1.15, 1.16 as in the underlying expression:

$$E_J(\varphi) = \int IV dt = -\frac{\Phi_0 I_C}{2\pi} \cos(\varphi) = -E_J \cos(\varphi) \quad (1.31)$$

Therefore the Hamiltonian of the DC SQUID in the approximation of negligible loop inductance is given by:

$$H_{SQUID} = -E_{J1} \cos(\varphi_1) - E_{J2} \cos(\varphi_2) \quad (1.32)$$

$E_{J1}$  and  $E_{J2}$  are the Josephson energies of the two junctions, respectively, and  $\varphi_1$  and  $\varphi_2$  are the phases across them. The flux quantization brings the following relation between the phases across the branches that made up the loop:

$$\varphi_1 + \varphi_2 = \frac{\Phi_{ext}}{\Phi_0} \quad (1.33)$$

The dynamics of the system can thus be described by a single variable  $\varphi_{1,2}$  and also tuned by an external magnetic flux  $\Phi_{ext}$ . Moreover it is possible to demonstrate that the Hamiltonian of the DC SQUID can be rewritten in the following form [16]:

$$H_{SQUID} = -E_{J+} \cos\left(\frac{\Phi_{ext}}{2\Phi_0}\right) \sqrt{1 + \left(\frac{E_{J-}}{E_{J+}}\right)^2 \tan^2\left(\frac{\Phi_{ext}}{2\Phi_0}\right)} \cos(\varphi) = -E_{J_{SQUID}}(\Phi_{ext}, E_{J+}, E_{J-}) \cos(\varphi) \quad (1.34)$$

where  $E_{J\pm} = E_{J1} \pm E_{J2}$  are the sum and difference between the Josephson energies of the junctions involved in the DC SQUID loop. The latter expression shows that a DC SQUID can be seen as a Josephson junction with a Josephson energy that can be tuned through an external magnetic flux inside its loop [16].

## 1.4 Superconducting qubits

Superconducting qubits are the basic elements of superconducting quantum processors [23]. A qubit is the quantum counterpart of the bits in classical computer and constitutes the fundamental logic unit of the modern quantum computer architecture. Qubits are quantum two level systems, like the two spin states of a spin 1/2 particle, like the ground and the first excited state of an atom, or like the vertical and horizontal polarization of a single photon. The generic notation for a qubit state denotes the ground state as  $|g\rangle$  and the excited state as  $|e\rangle$ . The essential feature that distinguishes a qubit from a bit is that, according to the laws of quantum mechanics, the permitted states of a single qubit fills up a two-dimensional complex vector space. The general state is the superposition of the basis states and is written as  $a|g\rangle + b|e\rangle$ , where  $a$  and  $b$  are complex numbers, and a normalization convention  $|a|^2 + |b|^2 = 1$  is normally adopted. In order to build a qubit system able to perform quantum computation processes, the latter system has to satisfy the DiVincenzo's criteria [24]:

1. A scalable physical system with well characterized qubits
2. The ability to initialize the state of the qubits to a simple fiducial state
3. Long relevant decoherence times, much longer than the gate operation time
4. A “universal” set of quantum gates
5. A qubit-specific measurement capability

The decoherence time, mentioned in point 3), is one of the indicator of a qubit quality and efficiency in a quantum computer architecture. In a qubit ensemble, in fact, multiple sources of decoherence could be present, such as the environment noise

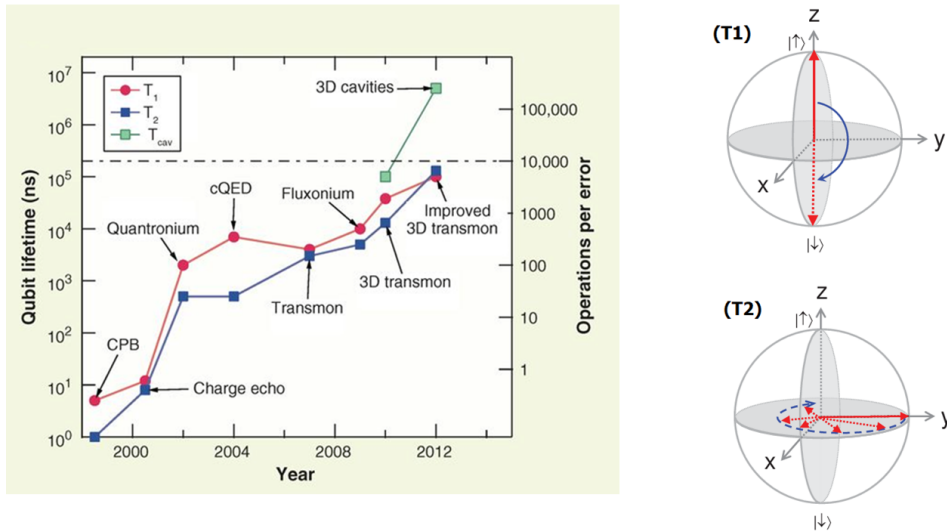


FIGURE 1.5: Trend of superconducting qubit performance during time in terms of qubit lifetime and number of computation operations able to perform before incurring into an error. The different points on the left trend indicate the characteristic time  $T_1$  (circle) and  $T_2$  (square) for each kind of superconducting qubit [2]. The right figures show the relaxation and dephasing phenomena linked to  $T_1$  and  $T_2$ , respectively, on the Bloch sphere used to represent the qubit state. [26]

coming from the spurious LC fluctuations mentioned in Sec. 1.3.1 or external electromagnetic fields. These decoherence sources lead to a loss of the qubit quantum behaviour and thus to the impossibility of its use in computation processes after a certain period of time. Two experimental quantities linked to the qubit decoherence are: the relaxation time  $T_1$  and the dephasing time  $T_2$ . The former is related to the time that the qubit state takes to spontaneously decay from the excited state to the ground state, while the latter, i.e. the dephasing time, depends on the time that passes before the qubit loses coherence and thus its quantum behaviour due to phase randomization, as shown in Fig. 1.5. Relaxation is caused by the unavoidable coupling of qubits with the environment, with whom they can exchange energy, inducing the collapse of the qubit in the ground state; dephasing is related to undesired coupling of the qubit with other quantum systems, such as: spurious LC oscillators, nuclear spins and photons due to quantum fluctuations [25]. In addition to the decoherence time, there are also other features that make a qubit type more or less suitable for implementation in quantum computer architecture, such as: capacity of coupling with multiple qubits and external devices, structural properties and production costs. As reported in Fig. 1.5, superconducting qubits constitute a promising platform, whose efficiency constantly develops in time. The continuous enhancement of superconducting qubits properties allows to perform computation processes much faster than

with other platforms [23]. Additionally, the fabrication technology behind superconducting qubits can take advantage of existing methods and processes (such as printable circuits) that have already been used and improved over time. As a result it is much easier to envisage a scalable superconducting quantum computer than with other existing methods [27] [28].

To introduce the qubits it is useful to start from the simplest quantum system: the quantum harmonic oscillator, defined by the LC oscillator introduced in Sec. 1.3.1. Its energy spectrum, obtained by the correspondent eigenvalues equations, has an harmonic trend where the different energy levels are characterized by the same energy separation of  $\Delta E = \hbar\omega$ , as shown in Fig. 1.6(a) [20]. This property represents a strong limitation for the realization of a qubit because it is impossible to separate a two-level system from all the other excited states. Therefore, in order to realize a superconducting qubit, a non linear component is necessary to provide anharmonicity to the energy spectrum. A non dissipative component that matches this requirement is the Josephson junction, which can be viewed as a non linear inductance, as shown in Sec. 1.2. The replacement of a Josephson junction in place of the linear inductance inside the superconducting LC circuit introduces anharmonicity between the different energy levels of the system, as shown in Fig 1.6(b). The first realized su-

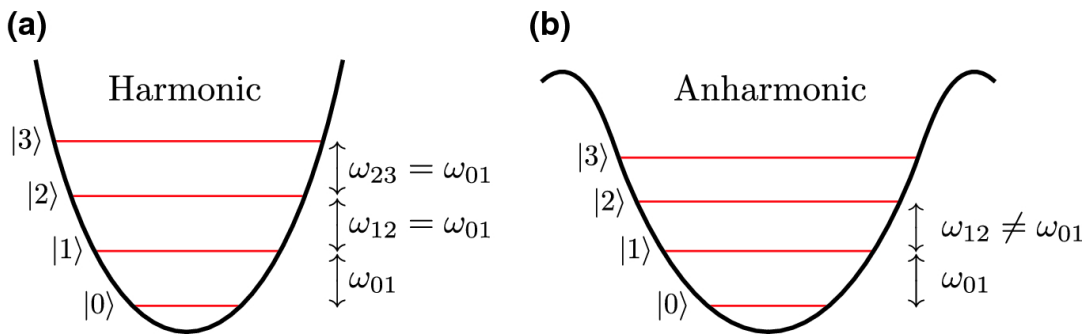


FIGURE 1.6: (a) Harmonic spectrum of the superconducting LC oscillator. (b) Anharmonic spectrum of the superconducting LC oscillator with a Josephson junction as a non linear inductance.

perconducting qubit was the charge qubit [2], also known as "Cooper pair box". The charge qubit is composed by a Josephson junction connected to a voltage source  $V_g$  through a capacitance  $C_g$ , as shown in Fig. 1.7(a). This last part of the circuit determines a background charge  $n_g = C_g V_g / (2e)$  induced on the superconducting island. The Hamiltonian of this circuit is [20]:

$$\hat{H} = 4E_C(\hat{n} - n_g)^2 - E_J \cos(1 - \hat{\phi}) \quad (1.35)$$

where  $\hat{n} = \hat{Q}/2e$  represents the number of Cooper pairs on the island, while  $\hat{\phi}$  describes the phase difference seen by the Josephson junction. These two operators

are the conjugate variables of the system and satisfy the following commutation relations:

$$[\hat{\phi}, \hat{n}] = i \quad (1.36)$$

Thus, it is possible to demonstrate that the Hamiltonian of the circuit can be rewritten using the  $\hat{n}$  basis [20]:

$$\hat{H} = \sum_n 4E_C(\hat{n} - n_g)^2 |n\rangle \langle n| - \frac{1}{2}E_J(|n\rangle \langle n+1| + |n+1\rangle \langle n|) \quad (1.37)$$

The dynamics of the charge qubit is described by a tight binding system where

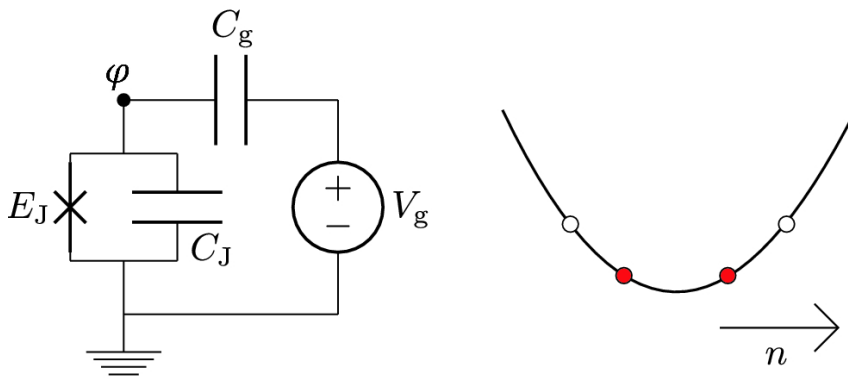


FIGURE 1.7: (a) Circuitual representation of a Cooper pair box. The circuit is composed of a Josephson junction of Josephson energy  $E_J$  and capacity  $C_J$ . A voltage generator is coupled to the Josephson junction through the capacitor  $C_g$  that defines the background charge  $n_g$  through the generator  $V_g$ . (b) Potential energy landscape related to the charge qubit. The red dots indicate the two lowest energy levels of the system [20].

the on site energy depends on  $E_C$  and  $n_g$  while the hopping term depends on  $E_J$ . The tunability of  $n_g$  through the potential source  $V_g$  allows to have a control on the system energy. If the Josephson junction is replaced by a DC SQUID it is even possible to tune the Josephson energy  $E_J$  and thus the hopping term. The energy levels of the system can be calculated through the following differential equation obtained by the application of the correspondence  $\frac{\hbar}{2e}\hat{Q} \rightarrow -i\hbar\frac{\delta}{\delta\phi}$  into the eigenvalues equation of the system with the Hamiltonian expressed by Eq. 1.35 [29]:

$$-4E_C \frac{\delta^2 \psi_n}{\delta \phi^2} + E_J(1 - \cos(\phi))\psi_n = E_n \psi_n \quad (1.38)$$

The values of  $E_n$  can be modified through a variation of the background charge  $n_g$ , as shown in Fig. 1.7(b). This property provides an easy way to change the

energy of the system, but unavoidably introduces charge noise, since the energy spectrum is very sensitive to  $n_g$ . Although charge qubits have large anharmonicity  $\alpha = \omega_{12}/2\pi - \omega_{01}/2\pi > 10 \text{ GHz}$ , relaxation and dephasing time are strongly limited by the charge noise, due to the presence of free charges in the system that are able to fill the unbonded orbitals of the atoms on the Josephson junction border surface, inducing unpredictable fluctuations of  $n_g$  [23]. The charge noise problem can be partially solved by choosing adequate values of  $n_g$  such that charge fluctuations induce negligible effects. By solving the Eq. 1.38 for  $E_J/E_C = 1$  it is possible to see from Fig. 1.8(a) that the values  $n_g = m + 1/2$  with  $m \in \mathbb{Z}$  are the best choices, because they correspond to the flat region of the energy bands.

To remove the effect of charge noise on the dynamics of the system it is possible to act on the energy parameters  $E_C$  and  $E_J$  of the system. As shown in Fig. 1.8(a-d), by increasing the ratio of  $E_J/E_C$  the energy bands become progressively flat, therefore insensitive to the value of  $n_g$ . The transmon qubit is based upon this principle [30]. From Fig. 1.8 it can be seen that the transmon qubit consists of a charge qubit shunted by a strong capacitor  $C_B$ , while the Josephson junction is replaced by a DC SQUID. The shunt capacitor has the role of decreasing the charge energy  $E_C = Q^2/2C$  to make the system operate in the charge noise insensitive regime ( $E_J/E_C \simeq 50$ ). The mere addition of the additional capacitor  $C_B$  leads to enhanced relaxation and dephasing times in the range of  $50 \mu\text{s}$  to  $100 \mu\text{s}$ , as shown in Fig. 1.5.

With the aim of preserving the quantum state of the qubit, it becomes essential to have an efficient and a non destructive read out system for the qubits that allows to measure the state of the qubit and to verify the related quantum computational operation. In this thesis work, an innovative device has been studied, designed and characterized, in order to perform a quantum non destructive read-out by using the phase detection of the qubit state which, in principle, can overcome some long standing problems that characterize the modern read-out methods described in the following chapter.

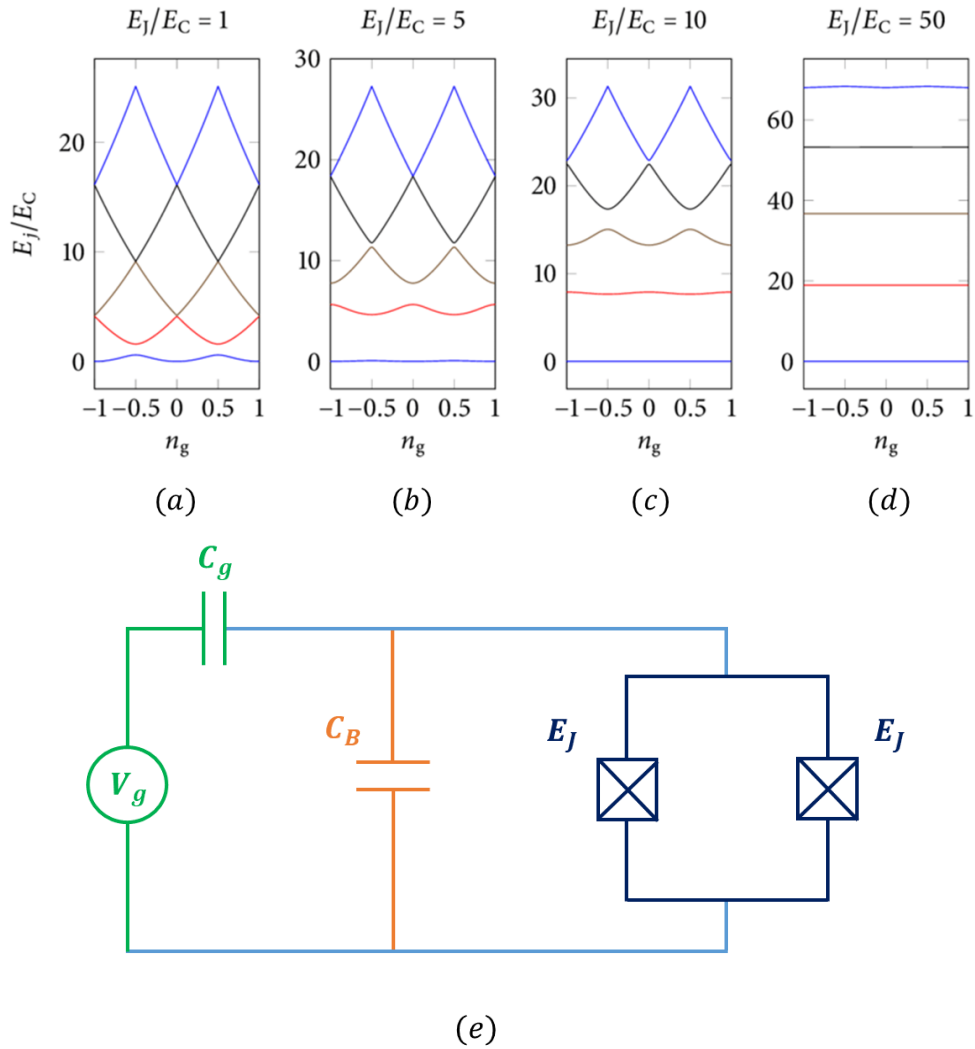


FIGURE 1.8: (a-d) Bands related to the charge qubit energy spectrum for different values of the ratio  $E_J/E_C$  [31]. (e) Schematic representation of the Transmon qubit circuit. The transmon is made up of a DC SQUID (dark blue) with two Josephson junction with Josephson energy  $E_J$ , a capacitor  $C_B$  (orange) that boosts the equivalent capacity of the circuit, and a voltage source  $V_g$  capacitively coupled with a capacitor  $C_g$  to the rest of the circuit (green), that plays the same role of the voltage source in the Cooper pair box.

## Chapter 2

# Non destructive read-out of superconducting qubit

In the previous chapter the fundamental properties of superconducting qubits have been introduced.

This thesis work aims at the design and characterization of alternative devices in order to perform Quantum Non Demolition (QND) read-out of superconducting qubits through a protocol that may overcome some limitations offered by the main currently employed QND read-out methods. A read-out method is said to be QND when the measure of the qubit state does not lead to the collapse of its wave function.

The second Chapter is divided as follows. In the first paragraph I will describe how QND read-out of superconducting qubit can be achieved through the principles of Cavity Quantum ElectroDynamics (CavityQED). To further enhance the understanding of this topic I will illustrate one of the main QND read-out protocol currently employed in most laboratories and a second innovative technique which has been recently validated [14]. In the second paragraph I will introduce the read-out circuit studied in this thesis work, the Josephson Digital Phase Detector, and the main features which allow to perform QND read-out of superconducting qubits.

## 2.1 Circuit quantum electrodynamics and quantum non demolition read-out

The fragility of qubit quantum state and the recent developments of quantum error correction protocol for fault-tolerant quantum computing [32] have made the qubit read-out an essential process towards the design of the first functioning quantum computer [2]. The measurement of quantum systems, such as qubits, can be a very delicate process due to the qubit sensitivity to external actions, that can ultimately lead to the collapse of the wave function that describes the sample under test. The collapse leads to a loss of the quantum properties, which in a quantum computer framework are needed to carry out the logical operations between qubits. Moreover, the QND technique can be used only when the desired dynamical variable is related to another physical feature with whom it does not hold an indetermination relation [33].

On the basis of this general rule several ways to perform QND read-out of superconducting qubit have been validated [13]. Most of these techniques exploit the peculiar functioning of each superconducting qubit and thus are specific of the particular kind of superconducting qubit under test. In addition, there is a general way of performing QND read-out of any kind of superconducting qubit, which is based on Cavity Quantum ElectroDynamics (CavityQED) [31]. CavityQED studies the interaction between light confined in a reflective cavity and atoms in order to control the latters. The capability of quantum circuits of recreating systems comparable with the ones of CavityQED leads to the development of the field of Circuit Quantum ElectroDynamics (CQED), from which the following QND read-out technique is extracted.

The idea is to replace a typical CavityQED configuration with the superconducting quantum circuit embedded in a cavity. Following the representation in Fig. 2.1, the atoms can be replaced by superconducting qubits, such as the Cooper pair box and the transmon, that can be seen as "artificial atoms" [13] given their dynamics described in Chapter 1; the optical cavity can be replaced by resonators for microwave photons, which operate in the same frequency range of actual modern superconducting qubits [23]. These resonators can be represented by LC oscillators or microwave waveguides that respectively work as single mode and multiple mode resonators with fixed adequate border conditions [34] [13]. By coupling a superconducting qubit to a resonator, the whole system will be described by the following Hamiltonian:

$$\hat{H} = \hat{H}_{resonator} + \hat{H}_{qubit} + \hat{H}_{interaction} \quad (2.1)$$

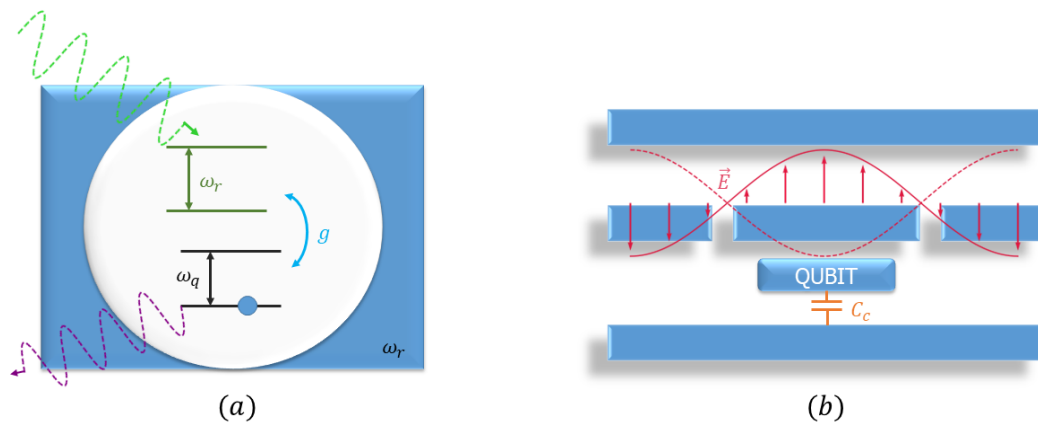


FIGURE 2.1: Analogy between cavity quantum electrodynamics and circuit quantum electrodynamics. (a) Typical CavityQED system with a quantum system, like an atom, inside an optical cavity of resonance frequency  $\omega_r$ . The atomic levels separated by  $\omega_q$  couple with the electromagnetic signals entering the resonator. The coupling intensity is represented by the coefficient  $g$  and depending on the detuning  $\omega_q - \omega_r$  the atom will interact with the electromagnetic radiations in different ways through photons exchange. Photons of frequency  $\omega_q$  and  $\omega_r$  arise in the cavity from the atom emissions and the external radiations trapped in the cavity, respectively. (b) CQED analog of the previous setup. The cavity is replaced by a waveguide that carries microwave radiations. The atom is replaced by the superconducting qubit capacitively coupled to the wave guide through a capacitor  $C_c$ . The microwave photons and the qubit develop the same kinds of interactions of the previous system.

The third term shows that the overall system is different from the direct sum of the two due to the interaction between the qubit and the resonator. Both systems will interact through an exchange of photons in the microwave spectrum region (4 – 20 GHz) [13]. This exchange develops thanks to the continuous excitations and de-excitations of the two systems and also because of the quantum fluctuations of the electromagnetic field in LC oscillators shown in Eq. 1.29, 1.30 that provide an interaction even in the absence of real photons [13]. Under the following conditions:

- Qubit is a perfect two level system, namely, the probability of incurring in transitions other than the one from the ground state to the excited state and viceversa is negligible.
- Rotating Wave Approximation (RWA): The interactions that don't preserve the number of photons, and thus the energy of the system, are negligible.
- The resonator is a single mode resonator, which means that even if it allows other modes, only the fundamental one is relevant in the system dynamics.

the Hamiltonian of the coupled system can be rewritten as the Jaynes-Cummings Hamiltonian [12], which in CQED describes the dynamics of an oscillator linked to a two level system:

$$\hat{H} = \hbar\omega_r \left( \hat{a}^\dagger \hat{a} + \frac{1}{2} \right) + \frac{\hbar\omega_q}{2} \hat{\sigma}_z + \hbar g (\hat{\sigma}_+ \hat{a} + \hat{\sigma}_- \hat{a}^\dagger) \quad (2.2)$$

$g$  is the coupling coefficient between the qubit and the resonator,  $\omega_r$  and  $\omega_q$  are the resonance frequency of the cavity and the qubit, respectively,  $\hat{a}$  and  $\hat{a}^\dagger$  are the annihilation and creation operators that represent the excitations in the cavity, respectively, while  $\hat{\sigma}_+ = |e\rangle \langle g|$  and  $\hat{\sigma}_- = |g\rangle \langle e|$  have the same role but for the qubit ground state  $|g\rangle$  and excited state  $|e\rangle$ . The representation of the cavity through ladder operators is possible thanks to the analogy between an LC circuit and a quantum harmonic oscillator, as described in Sec. 1.3.1. Creation and annihilation operators are defined by the following expressions [35]:

$$\hat{a}^\dagger = \frac{(L_r C_r)^{1/4}}{\sqrt{2\hbar}} \left( \frac{\hat{\phi}}{\sqrt{L_r}} + i \frac{\hat{q}}{\sqrt{C_r}} \right) \quad (2.3)$$

$$\hat{a} = \frac{(L_r C_r)^{1/4}}{\sqrt{2\hbar}} \left( \frac{\hat{\phi}}{\sqrt{L_r}} - i \frac{\hat{q}}{\sqrt{C_r}} \right) \quad (2.4)$$

The third term in the Jaynes-Cummings Hamiltonian describes the electrical-dipole coupling between a qubit and a resonator field, where the qubit can be excited by absorbing a photon, or return to the ground state by emitting a photon. Thus, the

coupling only connects the states  $|g\rangle|n+1\rangle$  and  $|e\rangle|n\rangle$ , where  $|n\rangle$  ( $n = 0, 1, \dots$ ) are the Fock states of the resonator field. The Hamiltonian in Eq. 2.2 can thus be diagonalized in the subspace  $\{|0, n+1\rangle, |1, n\rangle\}$  with the eigenvalues [13]

$$E_n^\pm = \omega_r \left( n + \frac{1}{2} \right) \pm \frac{1}{2} \sqrt{\Delta^2 + \Omega_n^2} \quad (2.5)$$

and the corresponding eigenstates are:

$$\begin{aligned} |+, n\rangle &= \cos\left(\frac{\theta_n}{2}\right) |e\rangle|n\rangle + \sin\left(\frac{\theta_n}{2}\right) |g\rangle|n+1\rangle \\ |-, n\rangle &= -\sin\left(\frac{\theta_n}{2}\right) |e\rangle|n\rangle + \cos\left(\frac{\theta_n}{2}\right) |g\rangle|n+1\rangle \end{aligned} \quad (2.6)$$

where  $\Omega_n = \Omega_0 \sqrt{n+1}$  is the n-photon Rabi frequency with  $\Omega_0 = 2g$  that corresponds to the vacuum Rabi frequency and the angle  $\theta_n$  is defined by  $\tan\theta_n = \Omega_n/\Delta$  with  $\Delta = \omega_r - \omega_q$  that represents the detuning between the qubit and the resonator. The eigenstates in Eq. 2.6 are called "dressed states" and are fundamental for the explanation of many experimental results in CQED [36] [37]. Their importance is mainly linked to their employment in quantum information processing in the domain of superconducting quantum circuits [38]. In Fig. 2.2, detailed energy-level diagrams for the bare and dressed states of the Jaynes-Cummings Hamiltonian are shown. The Jaynes-Cummings model is based on the RWA approximation, that is valid when  $(\omega_q + \omega_r) > \{g, |\omega_q - \omega_r|\}$ , namely when the qubit and the resonator are not too far from resonance and the coupling is below the sum of the two characteristic frequencies. Under this condition, there are different coupling regimes between the qubit and the cavity, that lead to different interactions, as highlighted in Fig. 2.2(b).

The first regime is the resonant one ( $\omega_r = \omega_q$ ), where a quantum of energy bounces back and forth between the qubit and the resonator at a rate given by the Rabi frequency  $\Omega_n$ . From the definition of the Rabi frequency it can be noted that the more photons there are in the cavity, the faster is the single-photon exchange between the qubit and the resonator. If the quantized resonator field is replaced by a classical field, then Rabi oscillations can be observed. By adequately tuning the energy and the time length of the classical field it is possible to exploit the Rabi oscillations to manipulate the state of the qubit coupled to the resonator. This makes the resonant regime essential for quantum information processing and quantum communication in a quantum computer framework [36] [39].

When the ratio  $g/\Delta \ll 1$  the system enters in a second regime called "dispersive regime" [13]. In this case, there is no resonant photon absorption or emission and thus no direct communication between the qubit and the resonator, but there are other

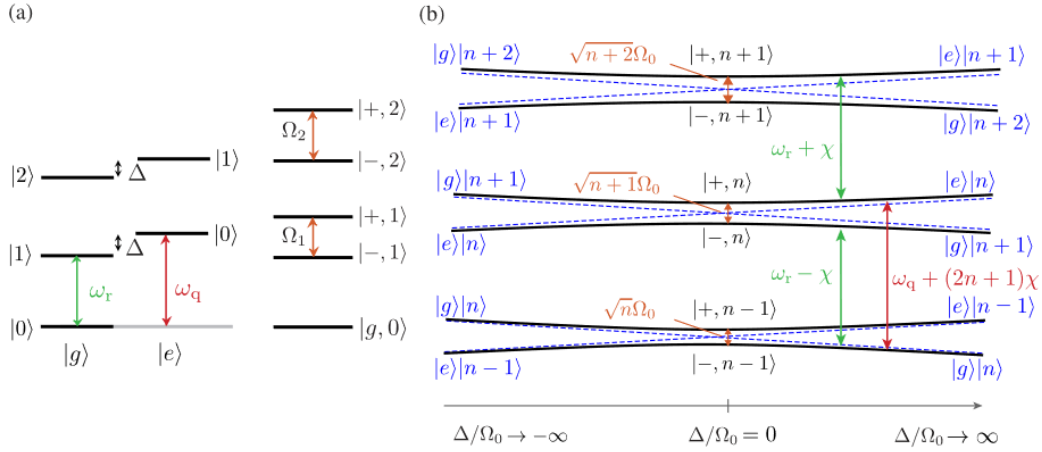


FIGURE 2.2: Energy-level diagrams for the bare and dressed states in the Jaynes–Cummings model. (a) Bare and dressed states. To the left, the bare states are represented in two ladders for  $|g\rangle$  and  $|e\rangle$ . The states  $|g\rangle|n+1\rangle$  and  $|e\rangle|n\rangle$  are close in energy, separated by  $\Delta = \omega_q - \omega_r$ , but without any coupling there are no possible transitions between these states. To the right, the coupling  $g$  is switched on and the nearby states hybridize, forming a new ladder with level spacings  $\Omega_n = \sqrt{\Delta^2 + (n+1)\Omega_0^2}$ . (b) Energy levels as a function of detuning. The characteristic  $\sqrt{n}$  non linearity of the Jaynes–Cummings ladder occurs at the resonance  $\Delta = 0$  (orange). In the dispersive regime  $|\Delta| \gg 2g$ , the dressed states in the asymptotic limit correspond to the unperturbed states with shifted energies (blue). The effective resonator frequency (green) is  $\omega_r \pm \chi$ , where  $\chi = g^2/\Delta$ , depending on the qubit state. The qubit (red) experiences a shift  $\chi_s = 2n\chi$ , called "Stark shift", due to the photons in the resonator and another shift  $\chi_l = \chi$ , called "Lamb shift", due to the vacuum fluctuations in the resonator [13].

extremely intriguing useful phenomena. The read-out protocol studied in this thesis work, in fact, takes advantage of the dispersive regime. For  $g/\Delta$  small enough, the Hamiltonian in Eq. 2.2 can be expanded to the  $2^{nd}$  order in  $g$ , obtaining the following expressions [13]:

$$\hat{H} \approx \hbar(\omega_r + \chi\sigma_z)(\hat{a}^\dagger\hat{a} + \frac{1}{2}) + \frac{\hbar\omega_q}{2}\hat{\sigma}_z \quad (2.7)$$

$$\hat{H} \approx \hbar\omega_r(\hat{a}^\dagger\hat{a} + \frac{1}{2}) + \frac{1}{2}(\omega_q + \chi + 2\chi\hat{a}^\dagger\hat{a})\sigma_z \quad (2.8)$$

where  $\chi$  depends on the coupling  $g$ , the detuning  $\Delta$  and also on the anharmonicity  $\alpha = \omega_{12} - \omega_{10}$  of the qubit spectrum, where  $\omega_{12}$  and  $\omega_{10}$  are the frequencies related to the transitions between the first and second excited state and between the first excited state and the ground state of the qubit, respectively.

$$\chi = \frac{g^2}{\Delta} \frac{1}{1 - \Delta/\alpha} \quad (2.9)$$

The coupling term from Eq. 2.2 becomes a shift on the resonance frequency of the resonator and the qubit, as shown in Eq. 2.7 and 2.8, respectively. Specifically, the shift on the resonator  $\chi_r = \chi\sigma_z$ , represented by the green arrow in Fig. 2.2, depends on the state of the qubit, while the shift on the qubit is made up of two terms:  $\chi_s = 2\chi\hat{a}^\dagger\hat{a}$ , called "Stark shift", represented by the blue arrow in Fig. 2.2, that depends on the photons number in the cavity;  $\chi_l = \chi$ , called "Lamb shift", that takes place even in the absence of cavity excitation. The fact that  $\chi_r$  depends on the state of the qubit opens to the possibility of performing QND read-out of the qubit state by evaluating the resonance frequency of the cavity coupled to it, that will be  $\omega_r + \chi$  ( $\omega_r - \chi$ ) in the excited state (ground state) of the qubit, as shown in Fig. 2.3(a). The conclusion is thus that to perform QND read-out of superconducting qubits it is possible to engineer the coupling between the qubit under test and the resonator in order to enter the dispersive regime, where the qubit state can be obtained through spectroscopy measurements of the resonator. To better understand the functioning of this technique, it is possible to make a further optical analogy with the measurement of the refractive index through the Mach–Zehnder interferometer, where the states of the qubit are referred to two different value of the refractive index, as shown in Fig. 2.3.

This technique is employed in the "Heterodyne detection", which is one of the main method employed for QND read-out of superconducting qubits [13] [35]. Another innovative and efficient method based on the dispersive regime, exploits a Josephson Photomultiplier (JPM) [40] to obtain the qubit state in a QND way [14].

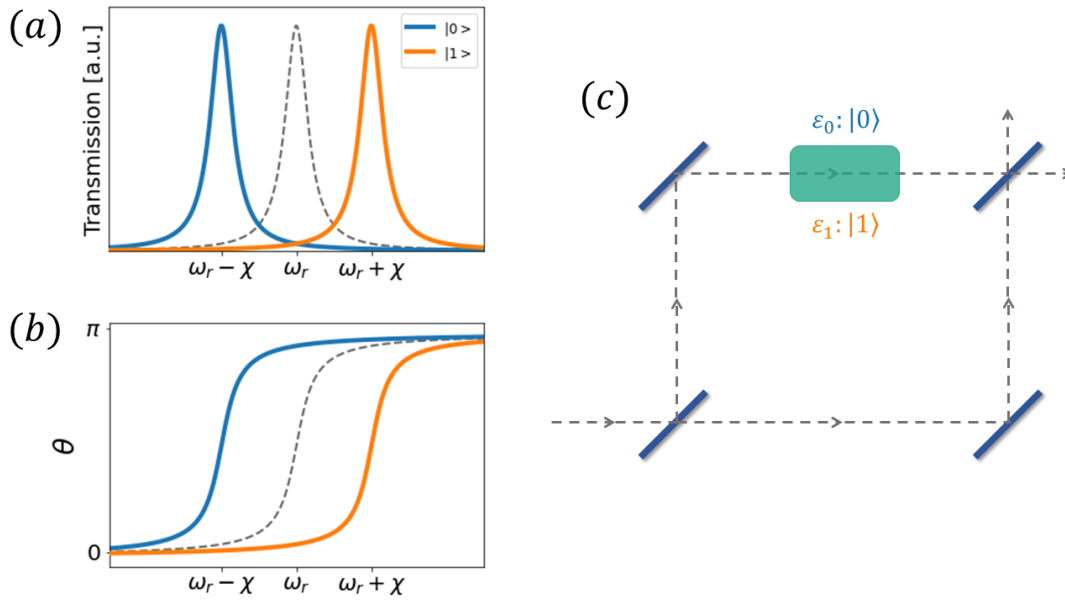


FIGURE 2.3: (a-b) Variation caused by the dispersive coupling between the resonator and the qubit. (a) Change of the transmission trend of the cavity depending on the state of the qubit. (b) Variation of the phase of the signal depending on its frequency and the state of the qubit. (c) Analogy between QND read-out of superconducting qubit through dispersive coupling with a microwave cavity and refractive index read-out of a sample through a Mach–Zehnder interferometer. In this analogy the two qubit states correspond to two different refractive index.

### 2.1.1 Heterodyne detection

Heterodyne detection is based on sending in input to the resonator coupled to the qubit under test a signal  $s_{in}(t)$  with a certain amplitude  $a_{in}(t)$  and frequency  $\omega_s$  and evaluating the change in amplitude and phase of the output signal  $s_{out}(t)$  that depends on the qubit state [13]. Neglecting the unavoidable attenuation, both signals can be described by the following definitions [35]:

$$s_{in}(t) = a_{in}(t)\cos(\omega_s t) \quad (2.10)$$

$$s_{out}(t) = a'_{out}(t)\cos(\omega_s t + \theta') \quad (2.11)$$

To illustrate how the read-out is performed, it is firstly important to analyse how the input signal can be generated. The main issue in this step is that generally a superconducting qubit is characterized by a resonance frequency of  $[4 - 20]$  GHz, which is a range of frequency hard to reach with standard modern signal generators. To overcome this problem the "IQ mixing" is generally employed. As discussed in the Appendix, the IQ mixing allows to accomplish the necessary up-conversion and a down-conversion of an input signal in a much more affordable way rather than using expensive and inefficient signal generators. Thanks to this tool it is possible to perform the heterodyne detection with the experimental set-up depicted in Fig. 2.5 in the following way [35]: an input signal of intermediate frequency  $\omega_{IF}$  and envelope  $a(t)$  is produced through a high frequency digital to analog converter (DAC). This signal is then fed to an IQ mixer that performs an up-modulation to the frequency  $\omega_q$ , which corresponds to a frequency near the resonance frequency of the isolated cavity, coupled in a dispersive regime to the qubit under test. The signal is then sent to the cavity, whose phase and amplitude will be modified depending on the state of the qubit according to the trends in Fig. 2.3(a,b). Therefore, from an input signal defined by Eq. 2.10, an output signal defined by Eq. 2.11 is obtained. The output is then down-converted, obtaining:

$$s_{out}(t) = \frac{a'(t)}{2}\cos(\omega_{IF}t + \theta') \quad (2.12)$$

The down-conversion is performed in order to bring the signal to a readable range for the analog to digital converter (ADC). Before entering the ADC, the signal is multiplied by a complex signal  $e^{i\omega_{IF}t}$  and rectified by a low frequency filter, thus

obtaining to the following complex signal:

$$d_{out}(t) = \frac{a'(t)}{2} \cos(\omega_{IF}t + \theta') e^{i\omega_{IF}t} = \frac{a'(t)}{4} [e^{i(2\omega_{IF}t + \theta')} + e^{-i\theta'}] \rightarrow \frac{a'(t)}{4} [\cos(\theta') - i\sin(\theta')] \quad (2.13)$$

The output signal  $d_{out}(t)$  is then averaged over a certain period of time  $[t_0, t_1]$  to obtain a single shot measurement that neglects any possible transients. Finally, a software extracts the real and imaginary part of the output signal defined by the underlying expressions:

$$I = \int_{t_0}^{t_1} a'(t) \cos(\theta') \quad (2.14)$$

$$Q = \int_{t_0}^{t_1} a'(t) \sin(\theta') \quad (2.15)$$

These two components represent a point on the complex plane  $(I, Q)$  that depending on the qubit state will go inside one of two coloured areas in Fig. 2.4 [35]. This means that by the position of the point on the complex plane it is possible to extract the state of the qubit. To decrease the electrical and thermal noise, other circuitual components are added between the latter link, as shown in Fig. 2.5. By repeating the measurement described above a certain amount of times, it is possible to obtain the quantum state of the qubit by the distribution of points on the complex plane.

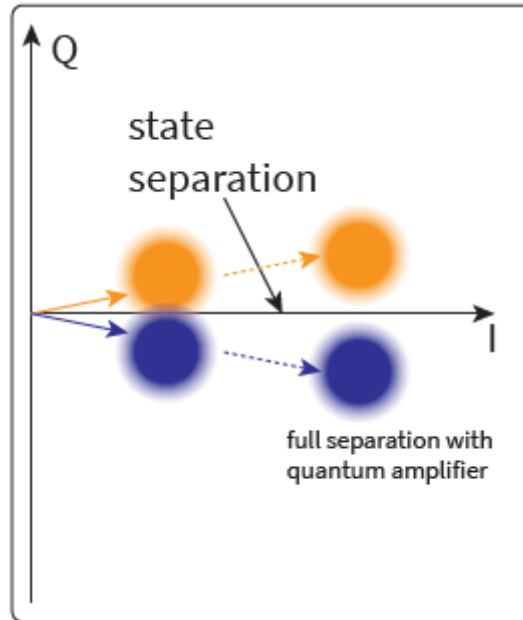


FIGURE 2.4: Qubit state separation on the I-Q plane. A quantum amplifier [15] is able to increase the separation between the two states and thus increase the precision of the measurement [35]

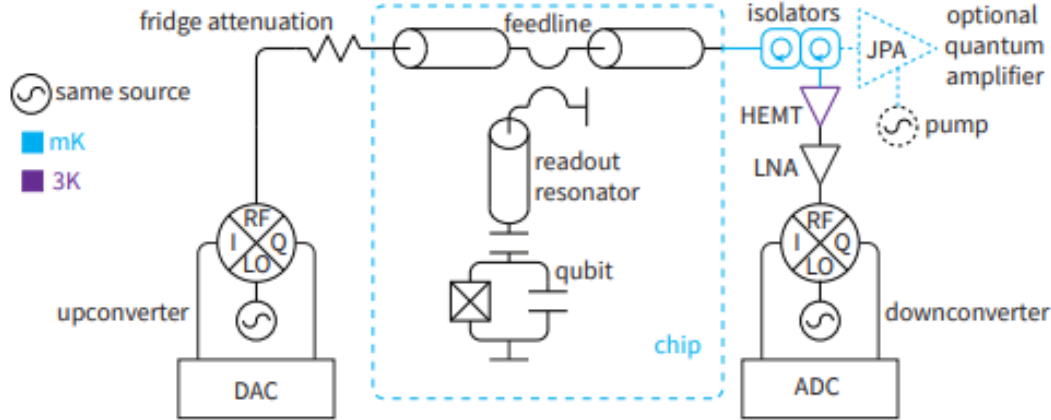


FIGURE 2.5: Example wiring diagram for heterodyne detection. A readout pulse is generated in a DAC and mixed up to the readout frequency. The heavily attenuated signal passes through a feedline coupled to the readout resonator. The output signal passes through a sequence of components, such as: circulators [13] and amplifier [41] [42] that improve the measurement. At room temperature the signal gets down-converted and an high-speed digitizer acquires the down-converted signal and process its IQ data in software. [35]

## 2.1.2 Josephson Photomultiplier method

A recently validated [14] second method performs QND read-out of superconducting qubits by exploiting a Josephson PhotoMultiplier (JPM). The set-up employed to perform the read-out protocol is shown in Fig. 2.6 where a JPM is probed at the output of a microwave resonator of frequency  $\omega_r$ , coupled in a dispersive way to the qubit under test that brings a shift  $\chi$  to the resonance frequency of the cavity. The JPM [40] is made up of a phase qubit [10] with a current bias that allows to tilt its potential energy trend. The photons generation is triggered in a narrow range of energies around a certain value, that I will call "switching energy". The potential energy of the JPM is described by the following expression [40]:

$$U(\hat{\varphi}) = -\frac{\Phi_0 I_C}{2\pi} \cos(\hat{\varphi}) - \frac{\Phi_0 I_B}{2\pi} \hat{\varphi} \quad (2.16)$$

where  $I_C$  is the critical current of the junction with a current bias  $I_B$  and  $\varphi$  is the superconducting phase difference across the junction, which is the variable that describes the dynamics of the JPM in the phase particle virtual representation. The circuitual parameters of the JPM are dimensioned in order to manipulate the potential energy so that its trend is similar to the one shown in Fig. 2.6, where the metastable minimum is characterized by two levels separated by the switching energy  $\hbar\omega_d = \hbar\omega_r + \chi$  and the highest state has an escape probability near 100%. Before the read-out protocol is initiated, the phase particle is positioned in the lowest energy state of the metastable

minimum through an appropriate current bias, as shown in the panels of Fig. 2.7(a,b). At this point a microwave signal of frequency equal to the switching frequency  $\omega_d$  is sent into the read-out circuit. The circuit will behave in one of the two underlying ways depending on the state of the qubit:

- Excited state  $|e\rangle$ : The signal is in resonance with the cavity that transmits the signal to the JPM. The signal has an energy equal to the switching energy and it is thus able to excite the JPM and leads to the escape of the phase particle from the metastable state to the states in the adjacent minimum. After the tunneling event the phase particle is going to fall to the state with the minimum energy through a sequence of spontaneous emissions. Because of this photons emission the state of the cavity related to the excited state of the qubit is called the "Bright State"
- Ground state  $|g\rangle$ : The signal is reflected by the cavity because the latter is characterized by a frequency of  $\omega_r = \omega_q - \chi \neq \omega_d$ . The phase particle of the JPM will thus remain in the metastable minimum and no absorption or spontaneous emissions take place. In contrast with the previous case, the state of the cavity correspondent to the ground state of the qubit is called the "Dark State"

Thanks to the characteristic relation in Eq. 1.16, 1.17, the different values of the phase difference  $\varphi$  between the bright and dark state leads to different magnetic flux across the JPM loop containing the Josephson junction. By measuring the flux is thus possible to read the state of the qubit under test. The just described method is a working and tested read-out method [14] and it also offers a natural digitalization of the measurement, as shown in Fig. 2.6, where depending on the qubit state the flux across the JPM loop will have a different direction. The fidelity brought by this first raw method, though, is just of 65% [35].

In the field of quantum metrology, the fidelity is a fundamental parameter used to measure the distance between two quantum states belonging to the Hilbert space of the quantum system under test. In particular, the fidelity measures how close one is to achieving the required quantum states that are utilized at a given stage in a quantum process [43], namely, the probability that one state will pass a test to identify as the other. Considering two states  $\rho$  and  $\sigma$ , their fidelity is defined [26]:

$$F(\rho, \sigma) = \text{Tr} \sqrt{\rho^{1/2} \sigma \rho^{1/2}} \quad (2.17)$$

Assuming that  $\sigma$  is a pure state  $\sigma = |\psi\rangle\langle\psi|$ , like the ground state  $|g\rangle$  and the excited state  $|e\rangle$  of a qubit, the fidelity can be rewritten through the following explicit formula [26]:

$$F(\rho, \sigma) = \sqrt{\langle\psi|\rho|\psi\rangle} \quad (2.18)$$

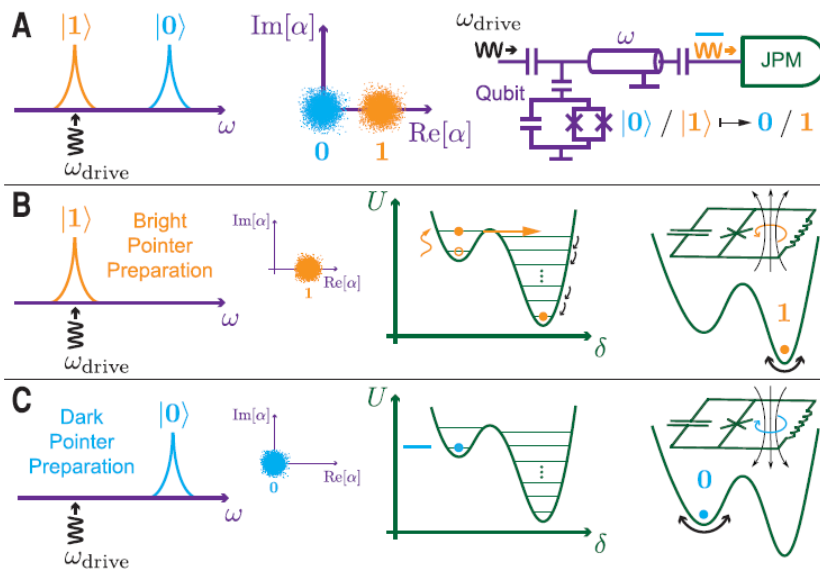


FIGURE 2.6: (A) Schematic representation of a JPM readout circuit and the bright/dark state of the cavity. The JPM is schematically represented by the green circuit in (B) and (C). The capacity is the intrinsic capacitance of the Josephson junction due to the oxide layer between the two superconducting electrodes of the junction; the inductance represents the inductive coupling with an external inductance that provides current bias to the circuit. (B) Schematic representation of what happens in the case the qubit is in its excited state. (C) Schematic representation of what happens in the case the qubit is in its ground state [14].

Namely, the fidelity is equal to the square root of the overlap between  $|\psi\rangle$  and  $\rho$ . In the context of qubit read-out, the fidelity is linked to the probability that the obtained result is correct and it can be evaluated by preparing a qubit in a well known state and applying multiple times the read-out method in order to obtain a statistic which corresponds to the fidelity of the read-out method [26]. The main cause of fidelity loss is due to the photons reflecting off the JPM and consequently travelling back to the qubit cavity causing back-action [35] [14]. To mitigate this phenomenon an auxiliary resonator capacitively coupled to the JPM is added to the circuit. This cavity, whose resonance frequency can be tuned through an external magnetic field applied to the JPM, allows to connect and disconnect the JPM circuit from the qubit. With this addition it is possible to perform the QND read-out by following the steps shown in Fig. 2.7. Compared to the previous protocol, in this case rather than directly detect photons in the qubit resonator, the JPM cavity is tuned on resonance with the readout resonator in order to transfer some of the photons, as shown in Fig. 2.7(c). After some time, the JPM cavity is detuned from the qubit resonator. In this way the photons are 'captured', preventing possible back travelling towards the qubit resonator. At this point, the JPM is tuned on resonance with the cavity and the

detection is performed, as depicted in the panels (d-f) of Fig. 2.7. Because of its role, the cavity coupled with the JPM is named "capture cavity". This improved protocol allows to achieve a fidelity of 92% [14], where the little fidelity loss are due to the qubit relaxation during the measurement followed by dark counts due to imperfect pointer state preparation [14].

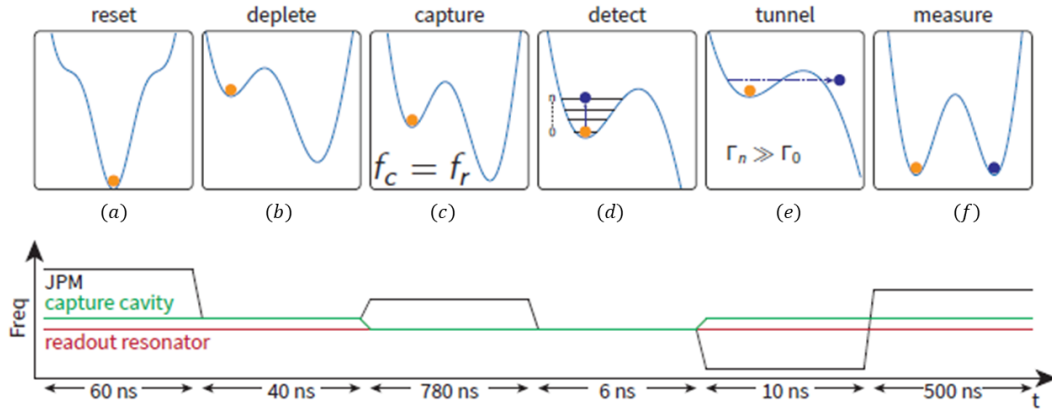


FIGURE 2.7: (a) JPM is reset into a single deep well, maximally detuned from the rest of the system. (b) The JPM potential energy is adequately tilted in order to trap the phase particle in the metastable minima. Simultaneously the JPM is tuned on resonance with the capture cavity to deplete any photons left over from last detection. (c) Capture cavity is tuned on resonance with the readout resonator, as the pointer-states are prepared. (d) JPM is tuned on resonance with the capture cavity and the readout resonator. If the qubit is in the excited state, the photons entering the cavity induce excitations to higher states in the initial well. (e) JPM is then tuned to a shallow bias point, so that higher energy states tunnel into the adjacent well. (f) Finally, the JPM is brought to a point where the two wells are maximally separated, allowing for microwave reflections to distinguish the two states [14].

## 2.2 Josephson Digital Phase Detector

In this section I will introduce an innovative method to perform QND read-out of superconducting qubits that exploits the physics of the superconducting quantum circuit shown in Fig. 2.8. The circuit has been called Josephson Digital Phase Detector (JDPD), and it is extremely similar to the Quantum flux parametron [44], a superconducting circuit designed for potential implementation in ultra-fast classical computing framework. The aim of this thesis work is to study the dynamics of the JDPD with the specific goal of demonstrating that it is capable of performing the protocol to carry out QND read-out of superconducting qubits.

The JDPD circuit shown in Fig. 2.8 is composed of two loops containing two Josephson junctions linked through a central inductor. On the sides of the loops there are two lines, called "DC line" that are inductively coupled to the circuit, as well as a line below the loops, called "Fast flux line". By connecting these lines to a current source, they can be exploited to provide the fluxes  $\Phi_1$  and  $\Phi_2$  across the loops, which allow to tune the dynamics of the system. The protocol is based on two fundamen-

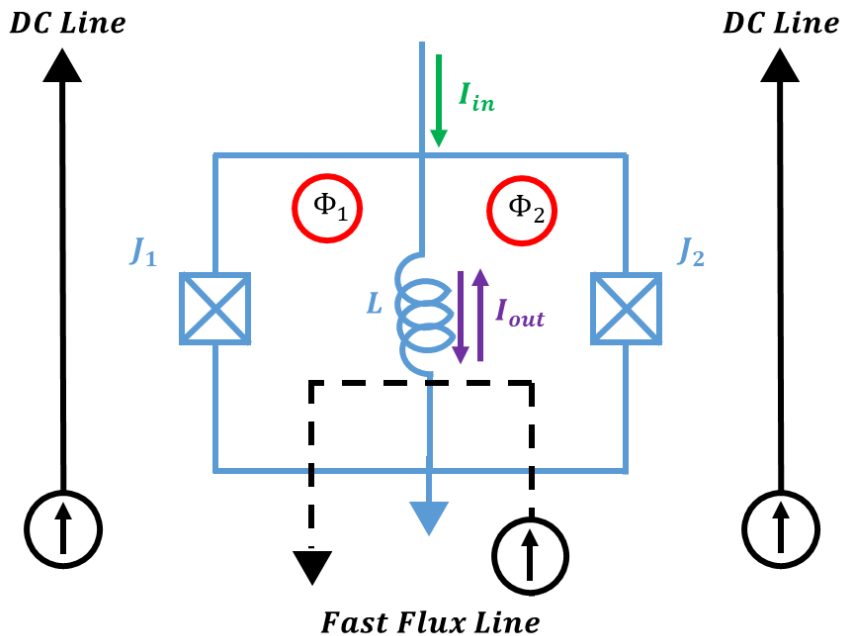


FIGURE 2.8: Circuit representation of the JDPD. The crosses represent the Josephson junctions with Josephson energy  $E_{J1}$  and  $E_{J2}$ . The critical currents are chosen such that  $J_1 = J_2$ . The inductors on the sides correspond to the flux lines inductively coupled to the circuit, which provide the fluxes  $\Phi_1$  and  $\Phi_2$  inside the loops. The fast flux line that goes below the circuit is coupled equally to both loops and thus provide the same amount of  $\Phi_1$  and  $\Phi_2$ .  $I_{in}$  is the current of the input signal while  $I_{out}$  is the output current that depends on the phase  $\varphi$  across the linear inductor  $L$ .

tal features of the superconducting quantum circuits: the phase detection allowed by the Josephson junctions and the tunability of their inductance through an external magnetic field. Given the fact that the potential energy of superconducting quantum circuits is a function of the fluxes across its branches and depends parametrically on the inductance of the system, the latter features allow to tune the potential energy of superconducting quantum circuits containing Josephson junctions, and thus their dynamic, through an external magnetic flux. This specific tunability is exploited in the read-out protocol, where the potential energy trend of the circuit is adequately changed through the fluxes  $\Phi_1$  and  $\Phi_2$  across the two loops provided by the flux lines on the sides. To understand how the manipulation of the JDPD potential energy trend can lead to the QND read-out of superconducting qubits, it is first necessary to obtain the analytical expression of the JDPD potential energy. Neglecting the kinetic inductance of the connection between the different circuital components, the JDPD potential energy is defined by the underlying expression:

$$U(\varphi) = \frac{E_L \varphi^2}{2} - E_{J+} \cos(\Phi_+) \cos(\varphi - \Phi_-) - E_{J-} \sin(\Phi_+) \sin(\varphi - \Phi_-) \quad (2.19)$$

where  $E_L$  is the energy of the central linear inductor,  $E_{J\pm} = (E_{J1} \pm E_{J2})/2$  and  $\Phi_{\pm} = \pi(\Phi_1 \pm \Phi_2)/\Phi_0$  represent the sum and difference between the Josephson energies of the two Josephson junctions and the fluxes across the two loops, respectively, and  $\varphi$  is the phase difference across the central linear inductor as well as the chosen dynamical variable of the JDPD. More details on the derivation of Eq. 2.19 can be found in the Appendix. In the case where there are no differences in the critical currents ( $J_- = 0$ ), the JDPD potential energy is represented by the underlying more compact expression:

$$U(\varphi) = \frac{E_L \varphi^2}{2} - E_J \cos(\Phi_+) \cos(\varphi - \Phi_-) = \frac{E_L}{2} [\varphi^2 - \beta \cos(\Phi_+) \cos(\varphi - \Phi_-)] \quad (2.20)$$

where  $\beta = 2E_J/E_L$  is a characteristic parameter of a symmetric JDPD related to the circuital components that compose it. Both Eq. 2.19, 2.20 show that in general the potential energy of the circuit in Fig. 2.8 depends on the sum and difference between the critical currents of the Josephson junctions,  $J_+$   $J_-$ , and between the fluxes across the two loops,  $\Phi_+$   $\Phi_-$ .

Assuming that the circuit is symmetric ( $J_- = 0$ ) and that the ratio  $\beta = \frac{2E_J}{E_L} > 1$ , the potential energy of the JDPD will show the behaviours depicted in Fig. 2.9 for different values of the flux  $\Phi_+$ . These different trends can be exploited to perform QND read-out of superconducting qubit with the set up shown in Fig. 2.10 in the

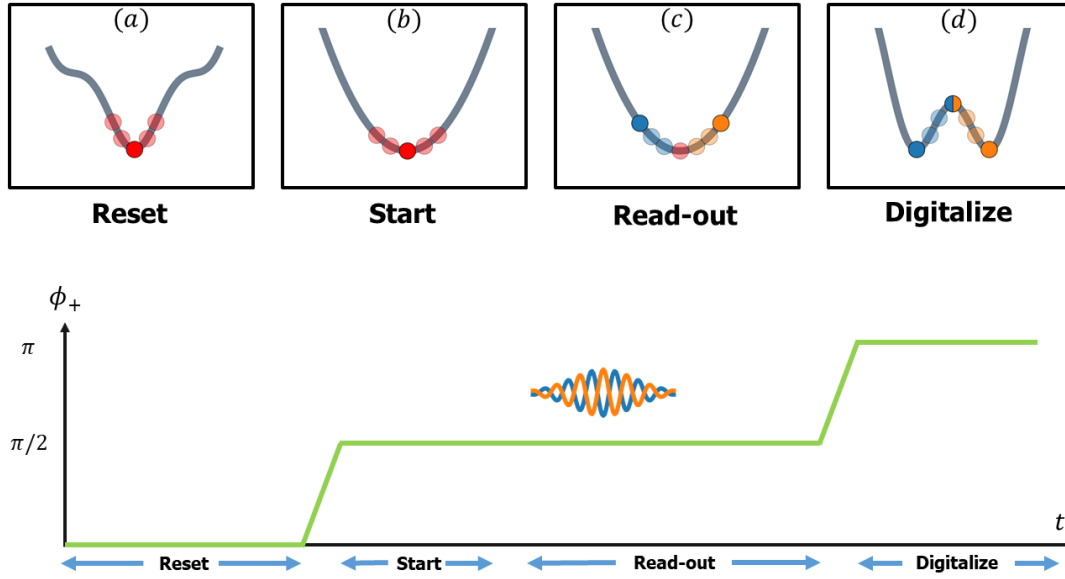


FIGURE 2.9: JDPD potential energy trends for different values of  $\Phi_+$  in the case there are no asymmetries ( $J_- = 0, \Phi_- = 0$ ) and  $\beta > 1$ . (a) JDPD potential energy in its unperturbed state with the phase particle that oscillates at the plasma frequency of the circuit. (b) To initiate the readout protocol the flux lines bring the potential energy in the harmonic state. (c) The readout signal enters the circuit and depending on the qubit state the phase particle will have a different phase offset. (d) In order to read the state of the qubit the potential energy is forced in its bistable state where the phase particle will fall in one of the two minima depending on the offset given by the readout signal.

following way: the read-out circuit is linked to the qubit coupled to a resonator; the coupling between the qubit and the resonator is engineered in order to enter the dispersive regime introduced in the previous section. To prepare the system to perform the read-out protocol, a flux of  $\Phi = \pi/4$  will be applied in both loops of the circuit, bringing its potential energy in the harmonic state, as shown in Fig. 2.9(b). In this condition the phase particle that represents the phase state across the linear inductance will just oscillate with a frequency equal to the plasma frequency of the system. The read-out is then initialized by sending a microwave signal to the resonator dispersively coupled to the qubit. The frequency of the microwave signal is chosen to be as near as possible to the resonance frequency of the isolated cavity. This choice maximizes the difference in the dephasing acquired by the output microwave signal depending on the state of the qubit, as shown in Fig. 2.3(b). The output signal will then enter the JDPD and force its phase particle to oscillate with a phase offset that depends on the qubit state due to the acquired dephasing, as shown in Fig. 2.9(c). To read the qubit state encoded in the oscillation another flux of  $\Phi = \pi/4$  is applied in both loops of the circuit to drive its potential energy in the bistable state. The phase

particle will fall in one of the two wells depending on the acquired phase offset and thus on the state of the qubit, see Fig. 2.9(d). The central inductance will show a different current direction output depending on the well in which the phase particle fall, allowing the read-out through a simple current measurement. The method just

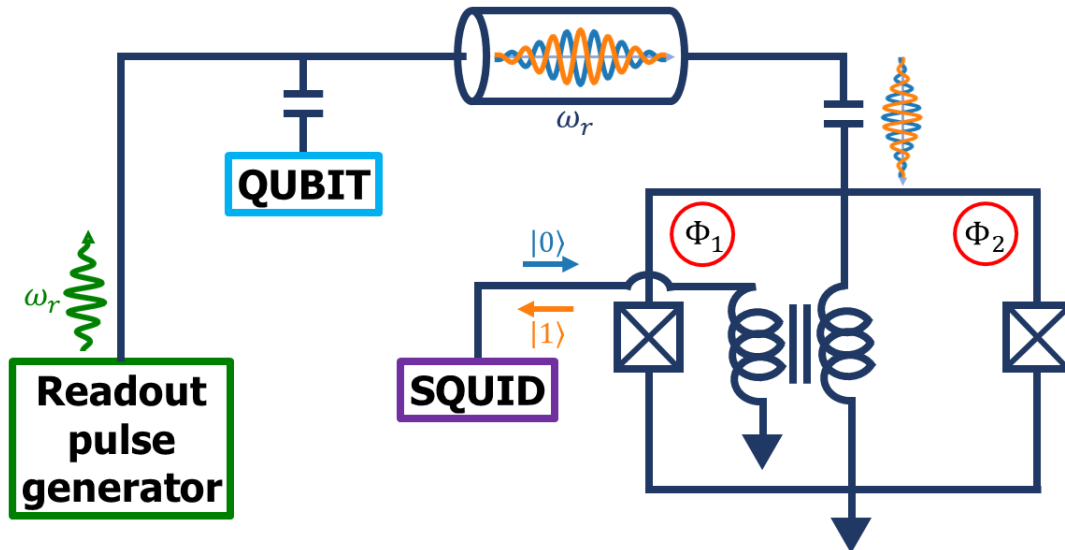


FIGURE 2.10: Schematic representation of the read-out experimental set up with the JDPD. The readout pulse generator generates the microwave signal of frequency  $\omega$  and sends it to the cavity represented by the cylindrical form in the schematic. Due to the coupling with the qubit, the resonator will add a different dephasing to the output microwave signal, that is thus characterized by two possible states, represented by the blue and orange signals in the resonator. The output signal will then enter the JDPD that gives in output a different current direction across the central inductance, depending on the qubit state. The signal can then be digitalized in the form of flux quanta through a SQUID inductively coupled to the linear inductance of the JDPD.

presented shows that the JDPD is in principle able to digitalize the qubit state and also to perform the measurement in the same cryogenic environment that contains the qubit. Additionally, the JDPD read-out protocol can be performed in a really simple way just through a sequence of quarter of flux quanta across the loops of the circuit, under the condition that the backaction is negligible. The read-out protocol that can be performed through the latter circuit allows to remove two crucial obstacles relative to the Heterodyne detection and the JPM method previously described:

- The connections to room temperature setup needed in the Heterodyne detection, that strongly decrease the scalability and are also potential noise sources.
- The complex timing of the JPM protocol needed to have the control on the read-out, as well as the complex resetting that requires the phase particle to be in the metastable minima.

The advantage of the JDPD read-out protocol made this circuit of great interest for application in the context of quantum computer, such as quantum buses [45] [46]. Quantum buses are circuitual cavities which can be used to store or transfer information between independent qubits in a quantum computer. Through these devices it is possible to create a parallel configuration with different qubits inserted in the circuit Fig. 2.10 and attached to a common feed-line through cavities with different resonance frequencies. In this way the cavities act as quantum buses that allow to detach each qubit from others and to communicate with a specific circuit by sending an electromagnetic signals in the feed-line in resonance with the corresponding cavity. It is thus possible to measure the state of each qubit attached to the feed-line just by sending signals of adequate frequencies that initiate the read-out protocol allowed by the circuit in Fig. 2.10, as shown in Fig. 2.11. The ultimate scope of this thesis work is to validate experimentally the dynamics of the JDPD in order to assure that it is able to reproduce the read-out protocol.

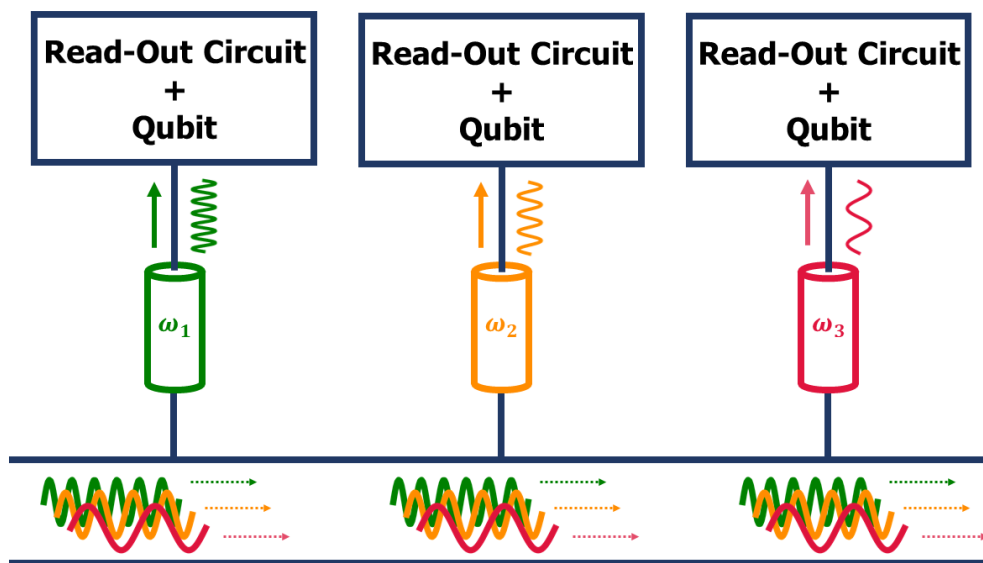


FIGURE 2.11: Schematic representation of the read-out circuit in Fig. 2.10 employed in a parallel configurations inside a quantum computer. The cavity coupled to the JDPD in each read-out circuit must be resonant to the relative quantum bus in order to initiate the QND read-out of the qubit as shown in Fig. 2.10.

# Chapter 3

## Experimental protocol and setup

In this chapter I will illustrate the experimental methods and the instrumentation.

The first section gives a description of the measurement technique to validate the Josephson Digital Phase Detector (JDPD) feasibility for a QND read-out protocol. The second section gives a brief description of the architecture and the functioning of the cryostat used to cool down the system to the range of temperatures required for quantum measurements with superconducting devices. The third part focuses more on the electronic set-up employed to perform the measurements. The final section describes how the experimental set-up can be used to supply  $\Phi_+$  and  $\Phi_-$  to the JDPD in different configurations.

### 3.1 Experimental planning

The experimental validation of the JDPD capability of performing QND read-out requires a precise measurement plan. The need to bring the circuit into its superconducting state down to sufficiently low temperatures of the order of  $10 - 20 \text{ mK}$ , the quantum behaviour of the circuit and the consequent sensitivity to external noise are all features that must be accounted in the planning of the various experimental steps. Given the mentioned experimental hurdles, the chosen way to analyse the JDPD dynamics is based on the study of the transmittivity and the reflectivity of electromagnetic signals sent in input to a circuit that contains the JDPD.

To understand how these spectroscopy measurements are linked to the JDPD dynamics, the first feature to notice is that, in a good approximation, the JDPD is made up of only inductive components. Neglecting the capacitance of the Josephson junctions, the JDPD can be represented as a single inductor of inductance  $L_{JDPD}$  equal to the equivalent inductance of the whole device. Following this approximation, let's consider the circuit portrayed in Fig. 3.1, where the JDPD is connected to an electromagnetic signal generator through a transmission line capacitively coupled to the latter. In this configuration the transmission line acts as a  $\lambda/4$  resonator thanks to the chosen border conditions. The coupling capacity  $C_c$  leads to a maximum of the

electric field (node of the current), while the JDPD brings a node for the electric field (maximum of the current) due to its inductor-like behaviour [34]. Assuming that the

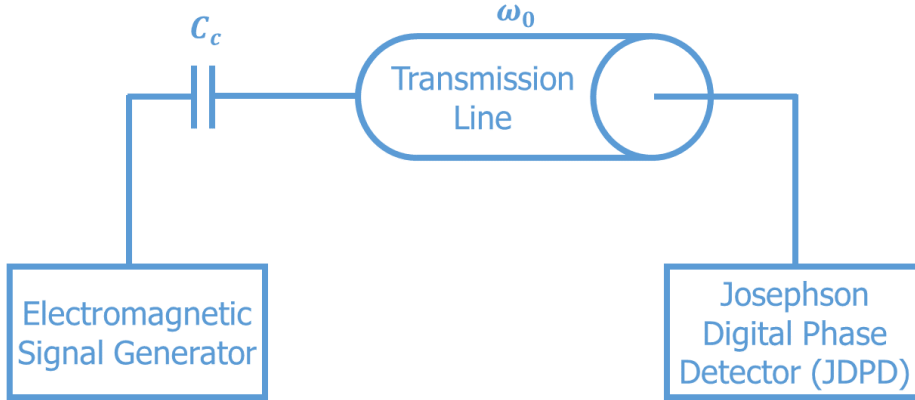


FIGURE 3.1: Schematic representation of the spectroscopy circuit used to simulate the dynamic of the JDPD during the read-out protocol. The capacity  $C_c$  couples the electromagnetic signal generator with the resonator of resonance frequency  $\omega_0$ . The JDPD together with the capacity set specific border condition at the ends of the transmission line, that leads the latter to be a  $\lambda/4$  resonator.

transmission line is made of superconducting material, the whole system acts as an LC oscillator for temperature near the critical current of the employed superconductors. The system is thus characterised by a resonance, whose spread and position depend on its capacitance and inductance according to the following definition:

$$\omega_{res} = \frac{1}{\sqrt{(C_c + C_r)(L_r + L_{JDPD})}} = \frac{1}{\sqrt{LC}} \quad (3.1)$$

The capacitance  $C$  depends on the coupling capacity  $C_c$  and on the transmission line capacitance  $C_r$ , while the inductance  $L$  depends on the JDPD equivalent inductance  $L_{JDPD}$  and on the transmission line inductance  $L_r$ . The connection between the resonance frequency  $\omega_{res}$  and the JDPD inductance  $L_{JDPD}$ , highlighted in Eq. 3.1, can be exploited to experimentally analyse the dynamics of the JDPD for different applied fluxes  $\Phi_+$ ,  $\Phi_-$ . To see how, let's consider first a generic superconducting LC oscillator. Following the mechanical treatment of electromagnetic circuits in Sec. 1.1, it is possible to associate to the LC oscillator a potential energy that depends on its inductance framework. By applying the phase-flux relation of Eq. 1.17 to the LC oscillator Hamiltonian, defined in Eq. 1.22, the following potential energy can be

extracted:

$$U(\varphi) = \left(\frac{\Phi_0}{2\pi}\right)^2 \frac{\varphi^2}{2L} \quad (3.2)$$

where  $\varphi$  represents the phase difference between the ends of the linear inductor in the LC oscillator. Let's assume that the phase  $\varphi$  plays the role of the dynamical variable of the quantum circuit, whose dynamic can be represented through the virtual representation of the phase particle. In this hypothesis, Eq. 3.2 allows to obtain the inverse relation that links the inductance to the position of the phase particle along the potential energy trend:

$$\frac{1}{L} = \left(\frac{2\pi}{\Phi_0}\right)^2 \left[ \frac{d^2U}{d\varphi^2} \right]_{\varphi=\varphi_{\text{Phase particle}}} \quad (3.3)$$

The latter relation states that the equivalent inductance of a quantum circuit can be obtained from the potential energy of its mechanical analog. Applying this notion to the circuit in Fig. 3.1, its equivalent inductance  $L$  can be extracted from its potential energy. The potential energy of the circuit depends on its inductive components, namely the JDPD and the passive inductance of the resonator. Assuming that the latter acts as a linear inductor, the potential energy of the circuit is defined by the JDPD potential energy in Eq. 2.19 plus the energy of a linear inductor. The equivalent inductance of the circuit, according to Eq. 3.3, is thus defined by the concavity of the JDPD potential energy trend in correspondence of the phase particle plus a constant related to the transmission line inductance. Given Eq. 3.1 that defines the relation between the equivalent inductance  $L$  of the circuit and its resonance frequency  $\omega_{res}$ , this latter result creates a bridge between the  $\omega_{res}$  and the JDPD dynamics. In conclusion, the JDPD phase particle position can be traced on the potential energy curve by studying the spectroscopy of the circuit in Fig. 3.1. Consequently, from the latter measurements it is possible to evaluate the effects of external fluxes  $\Phi_1, \Phi_2$  on the JDPD potential energy trend and validate the QND read-out protocol in Sec. 2.2. To ease the illustration of my thesis work I will call the circuit in Fig. 3.1 "spectroscopy circuit" from now on.

In the following sections I will introduce and describe the main instrumentation employed to perform the proposed experimental plan.

## 3.2 Cryogenic system

An essential step in the analysis of superconducting quantum circuits, such as the JDPD, is the thermalization of the system to values well below its critical temperature, that for standard superconductors is of the order of a few Kelvins or  $10\text{ K}$  [17]. The reaching of temperatures as low as  $10\text{ mK}$  is a fundamental requirement, not only to enter the superconducting regime, but also to minimise the effects of thermal noise during the measurements. For high enough temperature, in fact, thermal energy can lead to undesired transitions between energy levels separated by an energy below  $k_B T$ , where  $k_B$  is the Boltzmann constant and  $T$  is the circuit temperature. At the working temperature of  $10\text{ mK}$  the thermal energy in terms of frequency is equal to  $\nu_T = k_B T = 0.208\text{ GHz}$  that prevents most of the transitions in the superconducting devices. The creation of an environment with ultra-low temperatures that overcome the mentioned obstacles is allowed by designated devices called dilution cryostats. The dilution fridge is a device capable of reaching temperature near the absolute zero through cold temperature technology based on the thermodynamic properties of a mixture of  $^3\text{He}$ - $^4\text{He}$  that keeps that keeps a sufficiently high vapor pressure also in this low range of temperatures. The feature that differentiate cryostats from one to another is the way they reach their minimum temperature. From this point of view the cryostats can be divided into two main categories: wet cryostats and dry cryostats. These two types differ from each other for the pre-cooling part, namely the way they get to an intermediate temperature before reaching the lowest temperature allowed by the instruments. The wet type exploits an  $^4\text{He}$  bath to reach pre-cool temperatures of the order of  $4.2\text{ K}$ . The dry cryostats, instead, make use of a compressor, called "pulse tube refrigerator", which cools down the mixture through a sequence of compressions that brings the system to a temperature of  $10\text{ K}$ . Later on the mixture is passed through a sequence of pressure impedance that exploits the Joule-Thomson effect to lower the temperature of the mixture to values of the order of  $1\text{ K}$ . The cryostat employed in this thesis work is the Triton XL of the Oxford Instruments, which belongs to the latter type of cryostat, ideal to perform the long measurements required to study the dynamics of the JDPD. The Triton has a cylindrical form where on the head there are several connectors that allow to link the instrumentation at room temperature to the devices inside the Triton at cryogenic temperature. Below the cryostat head there are a sequence of gold-plated copper plates that present different holes which can be exploited to mount several components depending on the particular measurement that needs to be performed. As indicated in Fig. 3.2, each plate has a different temperature, that is constantly monitored through semiconducting resistors thermometers positioned on each plate. Between the first two plates

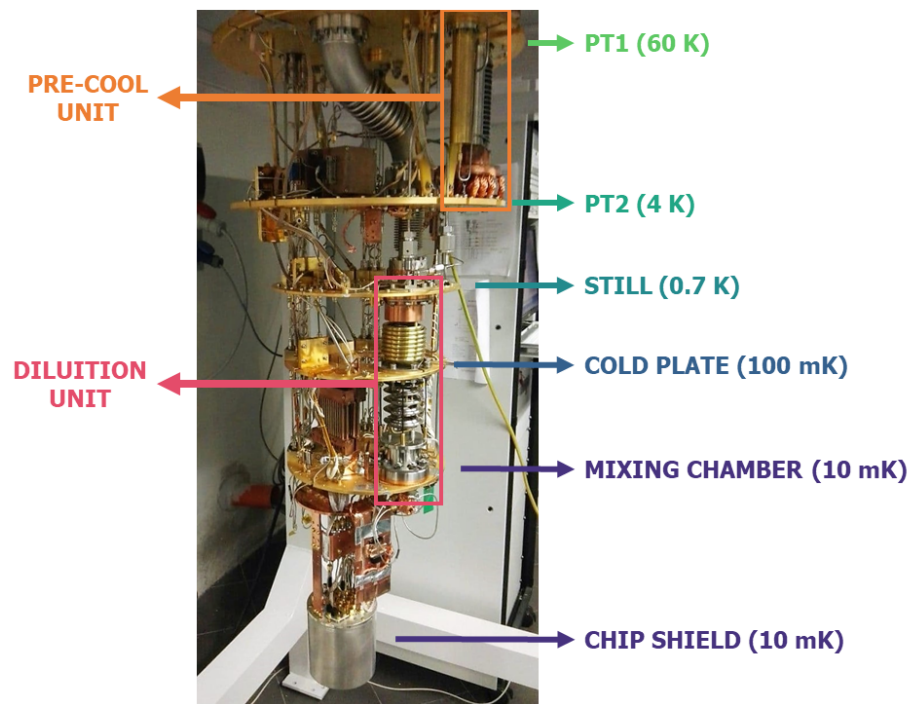


FIGURE 3.2: The core of the Triton dry dilution refrigerator. The labels indicate the different plates with the minimum temperature that they can reach, the orange and red rectangles indicate the pre-cool unit and the dilution unit, respectively, which are the fundamental units of the Triton cooling procedure. At the bottom, anchored to the mixing chamber there is a copper extension and the tin plated copper shield containing the device under test.

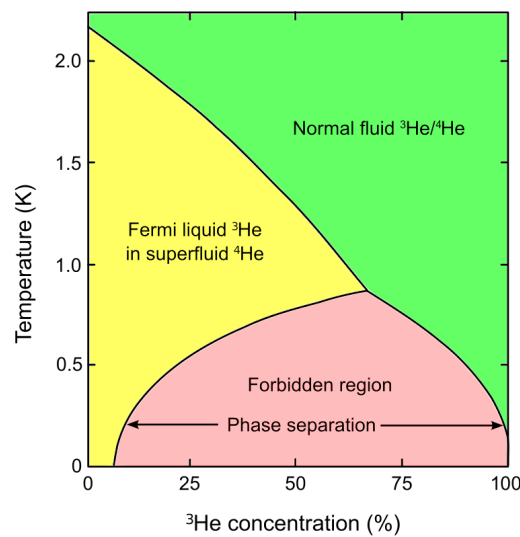


FIGURE 3.3: Phase diagram of  ${}^3\text{He}/{}^4\text{He}$  in terms of temperature and  ${}^3\text{He}$  concentration of the mixture. The region exploited by dry cryostat is the forbidden region where a phase separation occurs between the diluted and concentrated phases of  ${}^3\text{He}$ .

called PT1 and PT2 there is the pre-cool unit which works as previously explained. PT1 is at 60 K while PT2 works at 4 K. After that the system temperature is further lowered to the temperature of 0.7 K on the Still plate by exploiting the series of pressure impedance previously mentioned. From there the system is able to reach the temperature of 10 mK on the last plate, called mixing chamber. The mixture thanks to a pumping system can reach the mixing chamber by passing through a sequence of heat exchangers that decrease the temperature of the mixture below 0.7 K. The mixture is characterised by the phase diagram in Fig. 3.3 that highlights the tendency of the mixture to separate in a concentrated phase of  ${}^3\text{He}$  and a diluted phase of  ${}^3\text{He}$  for temperature below 1 K. The diluted phase, heavier than the concentrated phase, remains at the bottom of the mixing chamber while the remaining gas of  ${}^3\text{He}$  is pumped to the still plate where the procedure is repeated. The continuous reduction of  ${}^3\text{He}$  gas in the mixing chamber, lowers the temperature of the mixture according to the diagram in Fig. 3.3, which allows to reach the temperature of 10 mK. At the same time, the cyclic path that the  ${}^3\text{He}$  traverse, allows to never heat up the mixing chamber plate thanks to the work of the heat exchangers along the path, and also to avoid losses of the  ${}^3\text{He}$  gas, which is an extremely rare isotope. The stage containing the sample is thermally anchored to the mixing chamber through a copper extension, as shown in Fig. 3.4. The whole stage is then enclosed in a copper-coated box which screens from the environmental magnetic fields and is thermally anchored to the mixing chamber. Inside this box, the chip is placed on the chip-holder shown in Fig. 3.4,

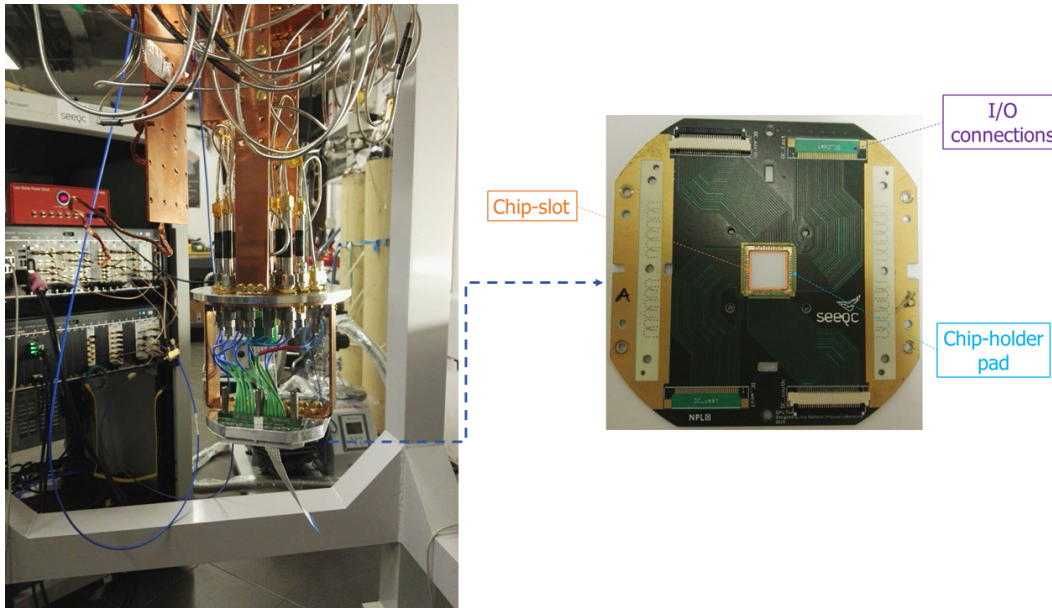


FIGURE 3.4: (Left) Copper extension anchored to the Triton mixing chamber containing the chip and the connections to the head of the cryostat. (Right) Chip holder provided by SeeQC. The orange area in the figure indicate the chip-slot where the chip under test is positioned; the pads on the sides allow to create connections between the chip and the room temperature set-up.

where the border pads allow to connect the pads on the chip to the room temperature set-up attached to the head of the cryostat. The upper plates are also screened from the environment through copper-coated cryoperm shields and a second metallic cover, both mounted before initiating the cool down procedure.

### 3.3 Electronic set-up

The electronic set-up employed to measure and analyse the dynamics of the JDPD is made up of a large variety of instruments at room temperature that play different roles.

The Vector Network Analyzer (VNA), which has been employed to perform spectroscopy measurements. The VNA is a multi-port instrument able to measure the amplitude and phase of an electromagnetic signal sent and received through any of its ports thanks to the inherent signal generators and receivers. This makes the VNA capable of measuring the network parameters of the electronic system under test over the range of frequencies allowed by its generators and receivers. The network parameters, also called S-parameters, are the elements of the scattering matrix, which is a square matrix of dimension equal to the VNA number of ports, that defines the relation between the voltage amplitude  $V_i^-$  and  $V_j^+$  of the reflected and incident waves

on the different ports respectively:

$$\begin{bmatrix} V_1^- \\ V_2^- \\ V_3^- \\ \vdots \\ V_n^- \end{bmatrix} = \begin{bmatrix} S_{11} & S_{12} & S_{13} & \dots & S_{1n} \\ S_{21} & S_{22} & S_{23} & \dots & S_{2n} \\ \vdots & \vdots & \vdots & \ddots & \vdots \\ S_{n1} & S_{n2} & S_{n3} & \dots & S_{nn} \end{bmatrix} \begin{bmatrix} V_1^+ \\ V_2^+ \\ V_3^+ \\ \vdots \\ V_n^+ \end{bmatrix} \quad (3.4)$$

The elements of the scattering matrix are the S parameters, which are defined by the following expression:

$$S_{ij} = \left[ \frac{V_i^-}{V_j^+} \right]_{V_k^+ = 0 \text{ for } k \neq j} \quad (3.5)$$

In words, Eq. 3.5 says that  $S_{ij}$  is found by driving port  $j$  with an incident wave of voltage  $V_j^+$  and measuring the reflected wave amplitude  $V_i^-$  coming from port  $i$ . The incident waves on all ports except the  $j$ th port are set to zero, which means that all ports should be terminated in matched loads to avoid reflections. Thus,  $S_{ii}$  is the reflection coefficient seen looking into port  $i$  when all other ports are terminated in matched loads, and  $S_{ij}$  is the transmission coefficient from port  $j$  to port  $i$  when all other ports are terminated in matched loads [34]. Through the acquisition of the reflection and transmission trends for signal of different frequencies, it is possible to look for the system resonance and thus obtaining the spectroscopy of the circuit under test. Two different VNA have been employed in this thesis work. The first one correspond to a slot of the PXI chassis shown in Fig. 3.5 which is a multi-slot system produced by Keysight Technologies, where each slot plays a different role. The first slot is occupied by an embedded controller which allows to manage the different modules through a direct communication with computer programs. One of the slots works as a two port VNA, which is the one exploited to perform the spectroscopy measurements. Additionally, there are other modules that carry out different operations, such as: the arbitrary waveform generators, signal generator, IQ mixers and attenuators that allow to perform the heterodyne detection of qubit described in Chapter 2. A second type of VNA that has been employed is the Rohde&Schwarz Vector Network Analyzer ZVL6 (R&S ZVL) [47], which is a two port VNA. As shown in Fig. 3.6, differently from the previous one, this VNA presents a physical interface that allows to set different features related to the measurements and a display that shows the acquired data. Just as the previous one, it is possible to remotely control the VNA through an external computer linked to it.

Another important task in the experimental validation is to provide the fluxes  $\Phi_1$

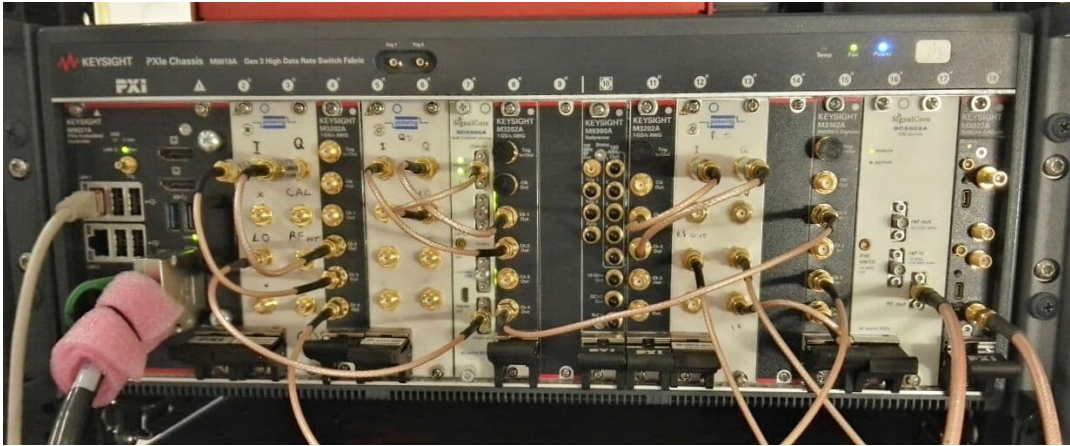


FIGURE 3.5: PXI chassis with 18 slots plus one dedicated to the control unit. Each slot plays a different role: 2,3,5,6,12,13 (IQ Mixer), 4,8,11 (AWG), 15 (Digitizer), 18 (2 ports VNA). In this thesis work only the VNA has been used.

and  $\Phi_2$  to the JDPD. The instrument that played this role is the Keithley SourceMeter. The SourceMeters are electronic device capable of supplying and measuring the voltage or the current through their input/output lines. These devices have been connected to the input on the Triton head to the flux lines of the JDPD in order to generate a current across them. The DC currents ultimately develop a magnetic field proportional to the current traversing the lines that couples with the loops of the JDPD, providing the required fluxes  $\Phi_1$ ,  $\Phi_2$ . By adequately tuning the current sent through the SourceMeter, multiple sweeps of the fluxes  $\Phi_1$ ,  $\Phi_2$  can be performed with a good resolution allowing to study the JDPD behaviour for different applied fluxes. Both the VNA and the SourceMeters can be remotely controlled through an external computer linked to them. All the measurements performed and described in Chapter 5 have been done by executing Python scripts on a computer linked to the electronic set-up. The Python scripts contain various strings of code that are sent to the electronic device with the aim of setting and querying different commands to dynamically set different features required by the experimental protocols.

### 3.4 Connections to the device under test

In Sec. 3.2 and 3.3 I have described the role and the functioning of the main instruments employed in this thesis work. Another fundamental part in the experimental setup are the connections between the mentioned devices, which are essential for the readability and the accuracy of the output results.

The Triton provides two sets of lines with specific filtering components dedicated



FIGURE 3.6: Front view of the Rohde&Schwarz Vector Network Analyzer ZVL6, which is a two ports VNA. The electronic connection with the device under test can be created through the ports at the bottom. The various buttons allows to set different features of the VNA, as well as changing its functioning modality. The results of the measurements are shown on the display.

to DC measurements and spectroscopy measurements of the device under test, respectively. The DC set involve current lines and voltage lines that allow a 4-point probe configuration of the device under test at the bottom of the cryostat. The lines are made of different materials along the different temperature stage of the cryostat. Each component is chosen with the aim of minimizing the thermal dissipation, which could disturb the measurement as well as the cryostat functioning. The current lines are made of copper between the room temperature stage and the 4 K stage due to the small resistivity of copper, and superconducting Nb-Ti alloy at temperatures below 4 K to exploit the zero resistance of superconductors at such temperatures. The voltage lines are made of manganin (Cu-Mn-Ni alloy) that has a low thermal conductivity. These lines pass through several filtering stages, located on some of the cryostat plates, before reaching the device under test, in order to filter the external electromagnetic noise. An initial filtering stage positioned on the head of the cryostat is defined by a pair of EMI filters that suppress electromagnetic high frequency peaks coming from the external environment. Inside the cryostat, the first filtering stage that the DC lines find is composed by a pair of low-pass RC filter with a cut-off frequency of  $f_c = 100 \text{ kHz}$ . After this preliminary filtering, the DC lines pass through a second filter component called "Cu Powder Filter" anchored to the cold-plate at 100 mK. The latter component, shown in Fig. 3.7 further blocks the passage of high frequency components in the signal by exploiting the skin effect.

For spectroscopy measurements, instead, the lines set is made up of coaxial cables, called RF lines, that carry the microwave signals produced by an external microwave

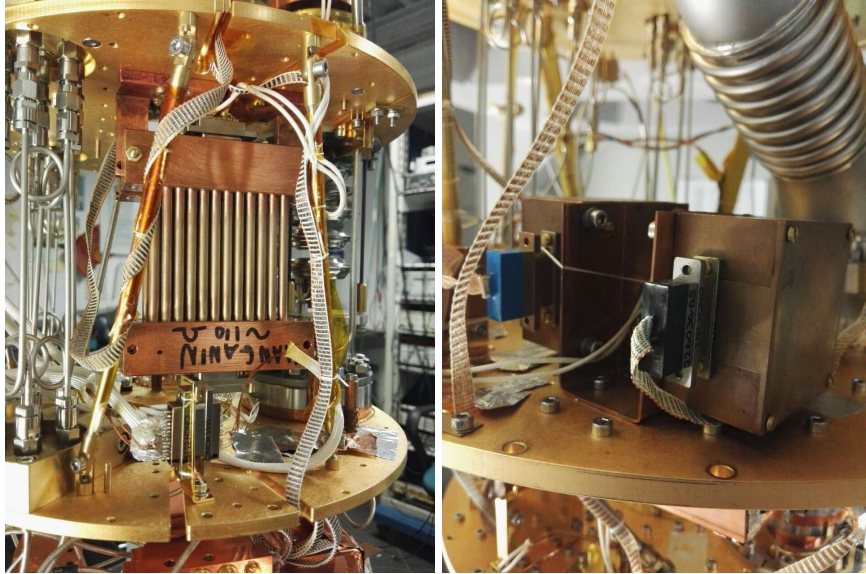


FIGURE 3.7: Photos of the Cu Powder Filter (Left) and the low pass RC filter (Right) used for the DC lines in the Triton cryostat.

signal generator inside the VNA. There are twelve input lines, made of stainless steel, split on two different paths, and two output lines made of Cu-Ni, from room temperature to 4 K, and superconducting Nb-Ti, from 4 K to the mixing chamber. Like the DC lines, the coaxial cables are thermally anchored to the different plates of the cryostat in order to favor a progressive thermalization of the lines. Along the cryostat, the microwave signals go through various components, as shown in the scheme of Fig. 3.8. The input lines pass through a series of attenuators that limits the signal power, allowing to get near the single photon limit to reduce dissipations effect [36]. In particular, the input cables pass through a total attenuation of  $-50$  dBm, that can be further increased by adding other attenuators at room temperature. The output readout signal passes through a cryogenic high electron mobility transistor (HEMT) amplifier produced by Low Noise Factory and biased using DC lines, consisting of a home-made copper loom. The amplifier is an active element and therefore it generates thermal noise, which becomes significant at the characteristic temperature  $T_n = 1.5$  K. For this reason, the device is placed at the 4 K stage in order to reduce the heat load. This device amplifies the previously attenuated signal in order to make it more readable for the VNA. Both input and output lines are connected to the I/O ports on the chip-holder shown in Fig. 3.4 through secondary connections that ultimately link the device under test to the electronic set-up at room temperature. Before entering the latter connections, the read-out signal generated by the VNA passes through a pair of circulators. A circulator is a three ports device where the input on one port is routed to become output from the next port in the sequence. Two circulators have been mounted on a copper extension anchored to the mixing chamber in

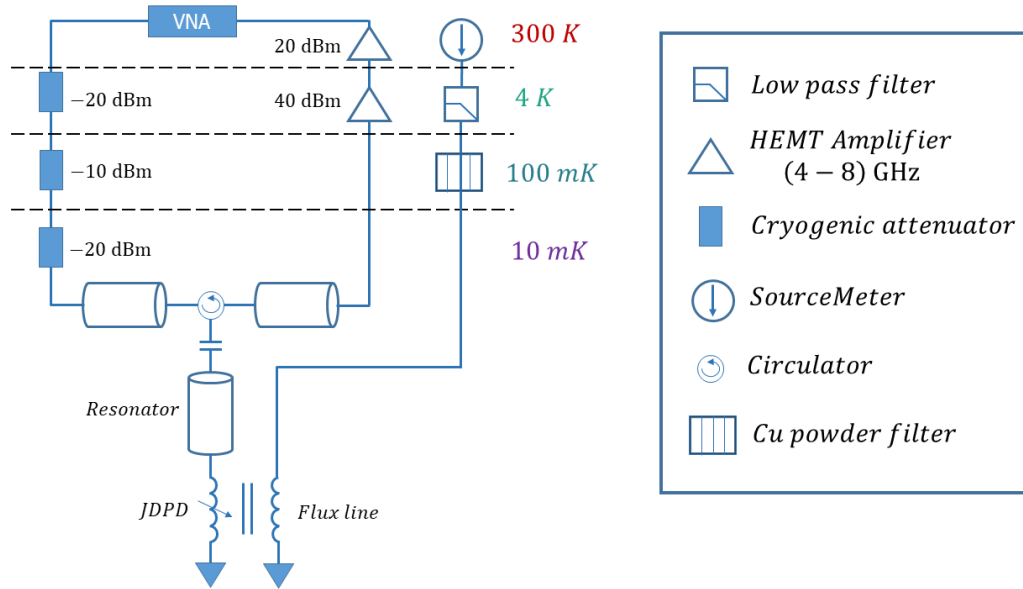


FIGURE 3.8: Schematic of the experimental setup. The different components are labelled.

order to prevent backaction from the attenuators and amplifiers along the system. Both VNAs have been employed for the characterization of the various connections in order to detect possible sources of losses or mismatch in the system. SourceMeters, instead, have been used to evaluate the impedance of the various lines. This latter analysis is essential in the calibration of the currents produced by the SourceMeter in order to generate the flux  $\Phi_1$  and  $\Phi_2$ .

### 3.5 Flux supply

To explore the dynamic of the JDPD, it is necessary to have control on the magnetic fluxes  $\Phi_{1,2}$ . In particular, by controlling  $\Phi_+ = \Phi_1 + \Phi_2$  and  $\Phi_- = \Phi_1 - \Phi_2$  it is possible to manipulate the JDPD potential energy and thus its dynamics, as shown in Eq. 2.19, 2.20. A significant part of the JDPD experimental validation has thus been dedicated to the calibration part in order to find the best way to provide  $\Phi_+$  and  $\Phi_-$  through the SourceMeters. To provide the magnetic fluxes inside the JDPD loops, the DC lines and the fast flux line have been probed to Keithley SourceMeters.

The calibration consists in defining the relation between the current or the voltage provided by the SourceMeter and the magnetic fluxes  $\Phi_+$  and  $\Phi_-$  induced into the JDPD. Due to some connection problems, the spectroscopy circuit tested and measured during my thesis work presented different working components. The first device presented a faulty DC line, while in the second one every component worked

fine. Each case thus required different ways to provide the fluxes  $\Phi_+$  and  $\Phi_-$ . Both employed methods are illustrated hereafter.

### 3.5.1 1<sup>st</sup> device calibration

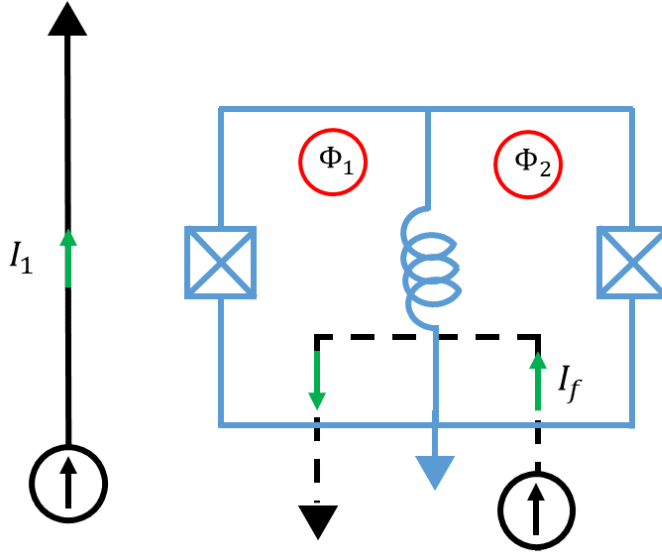


FIGURE 3.9: Schematic representation of the JDPD in the first measurement run.

To understand how the flux can be provided in the situation depicted in Fig. 3.9, let's consider the relation that defines the coupling between the fluxes  $\Phi_1$  and  $\Phi_2$  across the loops of the JDPD, and the current  $I_1$  and  $I_f$  provided by the DC lines, as labelled in Fig. 3.9. Assuming as convention that the positive direction of the flux is the one getting out of the loop, the coupling relations are defined as below:

$$\begin{aligned}\Phi_1 &= -M_d I_1 + M_{f1} I_f \\ \Phi_2 &= -M_c I_1 + M_{f2} I_f\end{aligned}\tag{3.6}$$

where  $M_d$  and  $M_c$  are the direct coupling and the cross coupling coefficient of the DC line, respectively, while  $M_{f1}$  and  $M_{f2}$  are the coupling coefficients of the fast flux line with the two loops, respectively. Given the geometry of the system shown in Fig. 3.9, it is possible to assume in a good approximation that  $M_{f1} = M_{f2} = M_f$ . To obtain a definition of  $\Phi_+ = \Phi_1 + \Phi_2$  and  $\Phi_- = \Phi_1 - \Phi_2$ , the two previous equations can be summed and subtracted, obtaining:

$$\begin{aligned}\Phi_+ &= -(M_d + M_c) I_1 + 2M_f I_f = -M_+ I_1 + 2M_f I_f \\ \Phi_- &= -(M_d - M_c) I_1 = -M_- I_1\end{aligned}\tag{3.7}$$

where for simplicity the following coefficients have been introduced:  $M_+ = M_d + M_c$ ,  $M_- = M_d - M_c$ . By measuring the resistance of the lines through the SourceMeter it is possible to define a similar relation also between the fluxes  $\Phi_{\pm}$  and the voltages  $V_1, V_f$  across the DC line and the Fast DC line, respectively:

$$\begin{aligned}\Phi_+ &= -\frac{M_+}{R_1}V_1 + \frac{2M_f}{R_f}V_f = -a_+V_1 + a_fV_f \\ \Phi_- &= -\frac{M_-}{R_1}V_1 = -a_-V_1\end{aligned}\quad (3.8)$$

where  $a_{\pm} = M_{\pm}/R_1$  and  $a_f = 2M_f/R_f$  are the new coupling coefficients that take the place of  $M_{\pm}$  and  $M_f$ . An inverse relation that links the fluxes  $\Phi_{\pm}$  to the voltages can be extracted from Eq. 3.8. To do so the inverse of the matrix that links the voltages to the fluxes must be calculated:

$$\begin{bmatrix} \Phi_+ \\ \Phi_- \end{bmatrix} = \begin{bmatrix} -a_+ & a_f \\ -a_- & 0 \end{bmatrix} \begin{bmatrix} V_1 \\ V_f \end{bmatrix} \rightarrow \begin{bmatrix} V_1 \\ V_f \end{bmatrix} = \begin{bmatrix} 0 & -1/a_- \\ 1/a_f & -a_+/a_f a_- \end{bmatrix} \begin{bmatrix} \Phi_+ \\ \Phi_- \end{bmatrix} \quad (3.9)$$

From the latter matrix expression it is possible to provide separately the fluxes  $\Phi_+$  and  $\Phi_-$ . Assuming that  $\Phi_- = 0$  or  $\Phi_+ = 0$  the previous expressions provide respectively the following relations:

$$\begin{aligned}\Phi_+ \neq 0 \quad ; \quad \Phi_- = 0 &\rightarrow V_1 = 0 \quad ; \quad \Phi_+ = a_f V_f = a_+ V_+ \\ \Phi_+ = 0 \quad ; \quad \Phi_- \neq 0 &\rightarrow V_1 = \frac{a_f}{a_+} V_f \quad ; \quad \Phi_- = -a_- V_1 = -\frac{a_- a_f}{a_+} V_f = m a_- V_- \end{aligned}\quad (3.10)$$

Through these relations it is possible to supply the desired fluxes  $\Phi_{\pm}$  to the JDPD and thus drive the spectroscopy circuit as requested by the experimental protocols.

### 3.5.2 2<sup>nd</sup> device calibration

In this situation there are more degrees of freedom that can be used to drive the JDPD, as shown in Fig. 3.10, allowing to exploit the full circuit. Assuming as before

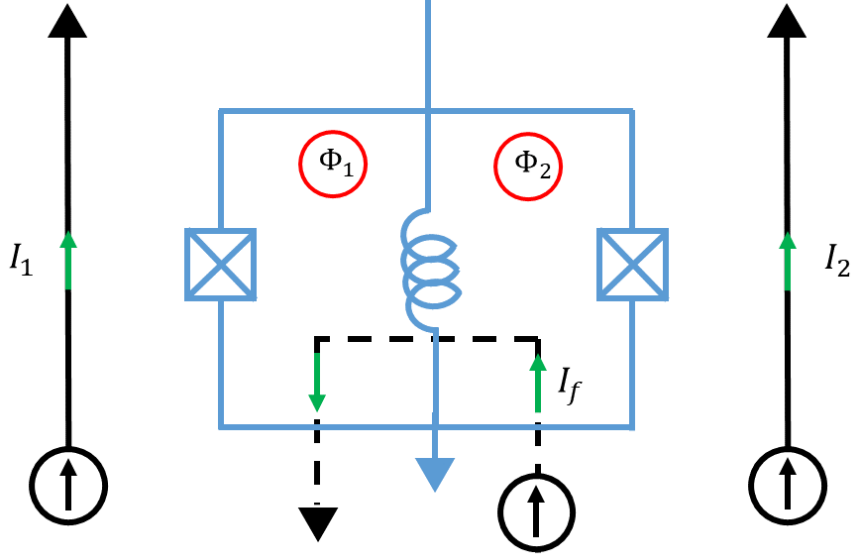


FIGURE 3.10: Schematic representation of the JDPD in the second measurement run.

that the positive direction of the fluxes is the one getting out of the loop, the coupling relations are defined as below:

$$\begin{aligned}\Phi_1 &= -M_d I_1 + M_c I_2 + M_f I_f \\ \Phi_2 &= -M_c I_1 + M_d I_2 + M_f I_f\end{aligned}\quad (3.11)$$

Through summing and subtracting each member of the expression, the following definition of  $\Phi_+$  and  $\Phi_-$  are obtained:

$$\begin{aligned}\Phi_+ &= -(M_d + M_c)I_1 + (M_d + M_c)I_2 + 2M_f I_f = M_+ I_+ + 2M_f I_f \\ \Phi_- &= -(M_d - M_c)I_1 - (M_d - M_c)I_2 = -M_- I_-\end{aligned}\quad (3.12)$$

where the new coefficients are defined:  $M_{\pm} = M_d \pm M_c$ ,  $I_{\pm} = I_2 \mp I_1$ . As done in previous case, it is convenient to consider also the link to the voltages. Assuming that the resistance across the DC lines and the fast flux line is  $R$  and  $R_f$  respectively, the relation is defined as follows:

$$\begin{aligned}\Phi_+ &= M_+ I_+ + 2M_f I_f = \frac{M_+}{R} V_+ + 2 \frac{M_f}{R_f} V_f = a_+ V_+ + a_f V_f \\ \Phi_- &= -M_- I_- = -\frac{M_-}{R} V_- = -a_- V_-\end{aligned}\quad (3.13)$$

with  $V_{\pm} = V_2 \mp V_1$  and the new coefficients  $a_{\pm} = M_{\pm}/R$  and  $a_f = 2M_f/R_f$  defined as before. The presence of a second DC line in this case allows to drive the flux  $\Phi_{\pm}$  in an easier way. It is in fact possible to use separately the fast flux line and the DC lines to respectively provide  $\Phi_+$  and  $\Phi_-$  to the JDPD, as highlighted by the underlying conditions:

$$\begin{aligned} \Phi_+ \neq 0 \quad ; \quad \Phi_- = 0 &\quad \rightarrow \quad V_1 = V_2 = 0; \Phi_+ = a_f V_f \quad \text{or} \quad V_- = V_f = 0; \Phi_+ = a_+ V_+ \\ \Phi_+ = 0 \quad ; \quad \Phi_- \neq 0 &\quad \rightarrow \quad V_+ = V_f = 0; \Phi_- = -a_- V_- \end{aligned} \tag{3.14}$$

The latter expressions highlight the ease with whom the JDPD can be driven and thus execute the read-out protocol proposed in Sec. 2.2. In principle,  $\Phi_-$  can be permanently set to a certain value by linking the DC lines to a pair of DC generators that provide an adequate pair of fixed voltages in order to eliminate the effect of potential geometric asymmetries in the circuit. After taking care of the asymmetries,  $\Phi_+$  can be individually controlled through a separate voltage generator that provides the voltage pulses needed to perform the read-out protocol, that relies exclusively on the action of  $\Phi_+$  in the absence of asymmetries.

## Chapter 4

# Preliminary simulation and experimental preparation

In order to design each component of the whole readout circuit and to realize optimal devices, a fundamental step has been the study of the electrodynamics of the Josephson Digital Phase Detector (JDPD) through different types of simulations. The aim of these simulations was not only to check the capability of the JDPD to perform the mentioned QND read-out protocol, but also to create some reference points and predictions regarding the spectroscopy behaviour of the circuit to optimize the design of the circuit in terms of readability. In this chapter I will briefly discuss the models used to perform the simulations and their main outcomes. In the first section I will describe the simulation of the read-out protocol through the PSCAN2 simulator. The second section will be dedicated to the characterization of the components of the circuit of Fig. 3.1 and to the description of the chip fabrication. The last part will cover all the simulations regarding the spectroscopy behaviour of the circuits in the chips, thus providing a set of predictions, to be compared with experimental outcomes.

## 4.1 Protocol simulation

To test the correctness of the read-out protocol in Sec. 2.2, I have collaborated to simulate the response of the JDPD to the flux sequence planned in the read-out protocol by using the simulator PSCAN2<sup>1</sup> (Portable Superconductor Circuit ANalyzer) [49] [50]. The dynamics of the Josephson junctions in the simulated circuits is described by the Tunnel Junction Microscopic (TJM) model. TJM is the most appropriate model to describe the behavior of a Josephson junction in a circuit and it is based on Werthamer model [51], thus employing Dirichlet series approximation of its integral kernels [52].

To initiate the mentioned simulation, I have written a *.cir* file and a *.hdi* file that define the components connections and the components properties, respectively. The simulated circuit consists of a JDPD connected to a current source, as shown in the schematic of Fig. 4.1. The current source allows to reproduce the two phase-shifted signals that come out from the transmission of an electromagnetic signal through the cavity coupled to the qubit, according to Fig. 2.3(b). In this way it is possible to test the JDPD actually provide two different and distinguishable outcomes depending on the phase of the input signal and thus on the state of the qubit. The simulated JDPD compared to the circuit in Fig. 2.8 presents two additional inductors  $L_1$  and  $L_2$ . These inductors, neglected in the analytical description of the JDPD, represent the kinetic inductance of the superconducting branches linking the components of the JDPD. The simulation thus plays a double role: it allows also to prove the JDPD capability of performing the read-out protocol and if the kinetic inductance of the branches can significantly affect the process.

The results of the simulations are depicted in Fig. 4.2. The profile of the input electromagnetic signal and the evolution of the provided flux  $\Phi_+$  have been defined in the *.hdi* file. The chosen signals produced by the current source are sinusoidal wave packets of fixed amplitude and duration but with different phase offset. The  $\Phi_+$  sequence emulates the sequence of the protocol in Fig. 2.9 with the switching time and rise time indicated in Fig. 4.2.

As shown in the  $I_L$  and  $\varphi$  plots of Fig. 4.2, depending on the phase offset of the input signal, the superconducting phase across the central inductor, as well as the current along it, acquires two equal and opposite values that allow to distinguish between the two cases. This means that by sending a sinusoidal envelope signal to the cavity, the JDPD is able to distinguish between the two states of the qubit, dispersively coupled to the cavity, by providing two current outputs with different direction. This

<sup>1</sup>PSCAN2 is a superconductor circuit simulator that comprises a Python module and a KLU-library-based linear equation system solver [48]. The Python part of the program performs netlist, parameters and prepares the sparse matrix for the solver.

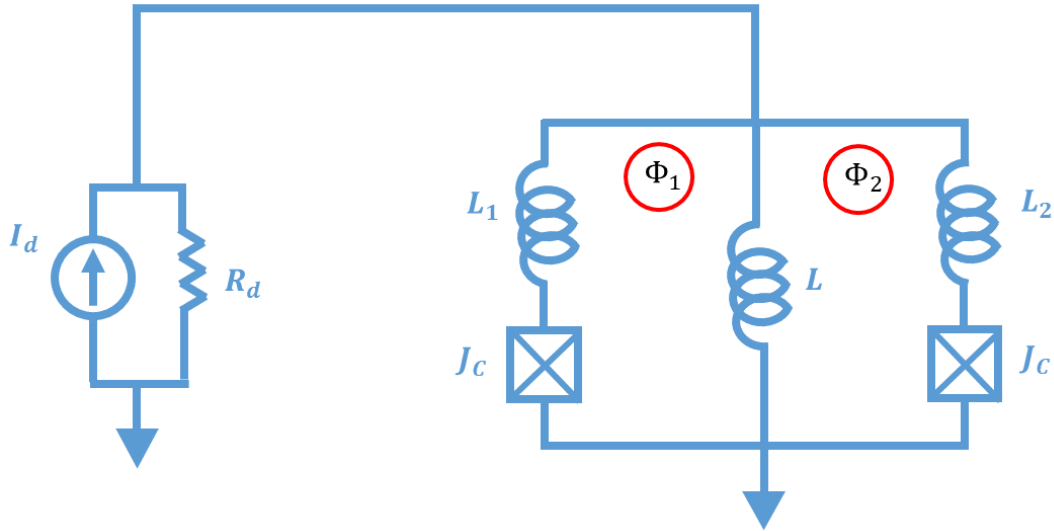


FIGURE 4.1: Schematic of the circuit simulated with PSCAN2. All the various component and their links have been declared in the `.cir` file related to the simulation.  $I_d$  is the driving current source that produces the input signals and  $R_d$  is the related resistance with a value set to  $R_d = 30 \Omega$ . The crossed squares on the sides of the JDPD are TJM Josephson junctions  $J_c$  described by the following set of properties: critical current  $J_c = 10 \mu A$ ; Stewart-McCumber parameter  $\beta_c = 60$ ; gap voltage  $\Delta V_g = 2.64 mV$ ; Ambegaokar-Baratoff ratio  $J_c R_n / V_g = 0.8$ ; normal-to-subgap resistance ratio  $R_n / R_{sg} = 0.01$ . The central linear inductor  $L$  and the passive kinetic inductance on the sides  $L_1, L_2$  are set to  $L = 65.8 pH$  and  $L_{1,2} = 32.9 pH$ . This leads to a ratio between the central inductance and the passive inductance of  $L / L_{1,2} = 2$ , which represents a large underestimate of the ratio expected in the real JDPD. This choice was made to check that the passive inductance would not perturb significantly the read-out protocol, even in such cases. All these properties have been set in the `.hdi` file related to PSCAN2 simulation.

confirms that the JDPD is able in principle to perform QND read-out of superconducting qubits and also that the kinetic inductance of the branches does not affect the mentioned process.

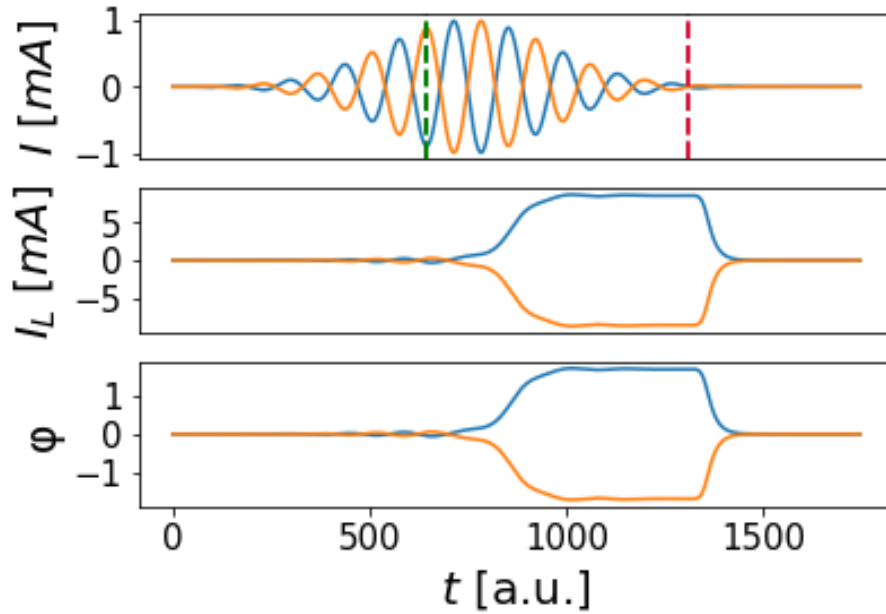


FIGURE 4.2: PSCAN2 read-out protocol simulation. The upper plot shows the shape of the input signals sent to the JDPD. The middle plot portrays the evolution of the current that develops across the central inductor depending on the input signal. The bottom plot depicts the evolution of the superconducting phase between the ends of the central inductor depending on the input signal. The dashed lines in the upper plot indicate when  $\Phi_+$  is being set to  $\Phi_+ = \pi$  (green) and to  $\Phi_+ = 2\pi$  (purple). The rising time of both pulses is of  $50 \text{ a.u.}$ .

## 4.2 Circuit characterization

After testing the correctness of the read-out protocol, I have characterized the components in the circuit reported in Fig. 3.1. This step is essential for the optimization of the spectroscopy circuit towards a better readability of the experimental data acquired by using the cryogenic and electronic setup described in Chapter 3.

I have performed some simulations where, by tuning the circuital parameters, I have searched for the spectroscopy circuit layout that better satisfy the above mentioned goal. The conditions to be satisfied are summarized in the following points:

- a. Circuit resonance frequency in the range of  $[4 - 8]$  GHz, which is the frequency range of the HEMT amplifier.
- b. Maximise the resonance frequency shift between the different JDPD states in order to distinguish them.
- c. Making the circuit capable of sustaining relatively high powers in the whole frequency range, without an excessive use of attenuators, in order to avoid the switching of the Josephson junctions to the resistive state.
- d. Maximise the quality factor of the circuit in order to have a narrow resonance that does not cause significant losses.

The simulations are performed both numerical, through Python scripts, and by employing the circuit simulator QUCS<sup>2</sup> (Quite Universal Circuitual Simulator) [53] [54]. It offers the ability to set up a circuit with a graphical user interface and simulate its dynamics from different points of view, such as the S parameters, which are the features mainly exploited in this thesis work.

Currently QUCS library does not allow the simulation of superconducting circuit and consequently does not contain the typical elements of a superconducting circuit, such as the Josephson junctions. To overcome this issue, I have emulated the spectroscopy circuit in the QUCS environment by replacing the JDPD with a tunable linear inductor, as shown in Fig. 4.3. In this approximation the different JDPD states are linked to different values of the inductance, following the arguments of Sec. 3.1. To simplify the simulations, I have focused on the two most important JDPD states for the read-out protocol: the zero state ( $\Phi_+ = 0$ ) in Fig. 2.9(a), characterised by a single

---

<sup>2</sup>QUCS is a free-software electronics circuit simulator software released under the General Public License (GPL). QUCS supports a growing list of analog and digital components as well as SPICE sub-circuits, that can be inserted in the simulation netlist. The simulation and the data processing are both performed through OCTAVE with the numerical analysis packages based on classical numerical mathematics routines for the solution of linear and non-linear, real and complex, algebraic equations and time domain algebraic and differential equations.

absolute minimum, and the bistable state ( $\Phi_+ = \pi$ ) in Fig. 2.9(d), characterised by two absolute minima symmetrical with respect to the origin.

### 4.2.1 Transmission line length and JDPD $\beta$

The first circuit component that I have characterised is the transmission line that links the JDPD to the VNA through a capacitive coupling. The schematic of the simulated circuit is portrayed in Fig. 4.3, which is similar to the spectroscopy circuit in Fig. 3.1 with the JDPD replaced by a linear inductor. As mentioned in Sec. 3.1, the transmission line acts as a  $\lambda/4$  resonator, which allows to achieve a maximum of the current in correspondence of the JDPD, in order to maximize the signal transfer and decrease the potential losses. Assuming that the JDPD is perfectly symmetric ( $E_{J-} =$

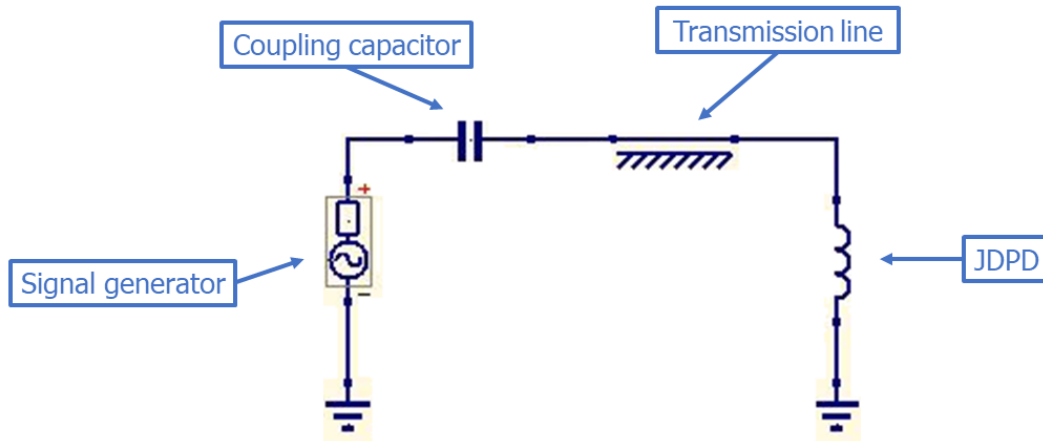


FIGURE 4.3: Spectroscopy circuit schematic in QUCS environment. The various components that make up the circuit are labelled in the figure.

0), the first numerical simulation that I have performed aims at the understanding of how the resonance frequency of the circuit, and the spectroscopic difference between the zero state and the bistable state of the JDPD is influenced by the length of the transmission line and the ratio  $\beta = 2E_J/E_L$  of the JDPD. The ratio  $\beta$  is a parameter used to differentiate the JDPD from each other, and it is linked to the influence of the sinusoidal term in the potential energy formula in Eq. 2.20 and thus on the effect of the Josephson junctions on the JDPD dynamics. To ease the analytical treatment, the transmission line is approximated to be a single mode  $\lambda/4$  resonator where the only mode  $f_0$  corresponds to the fundamental one, defined [34]:

$$f_0 = \frac{c_l}{4l} \quad (4.1)$$

where  $c_l$  is the speed of light along the transmission line and  $l$  is the length of the latter. Assuming that  $c_l = c$  and fixing the characteristic impedance to  $Z_0 = 50 \Omega$ , which is the required value to have an impedance match with the VNA, the capacity and inductance of the resonator are defined by the following relations [34]:

$$C_r = \frac{1}{2\pi Z_0 f_0} \quad (4.2)$$

$$L_r = \frac{Z_0}{2\pi f_0} \quad (4.3)$$

Neglecting for now the influence of the coupling capacitor, the similarities of the circuit with an LC oscillator allows to define its resonance frequency through the following expression

$$\omega = \frac{1}{\sqrt{C_r(L_r + L_{JDPD})}} \quad (4.4)$$

As mentioned in Sec. 3.1, the inductance  $L_{JDPD}$  will depend on the fluxes  $\Phi_+$  and  $\Phi_-$ . Through the JDPD potential energy defined in Eq. 2.20 and Eq. 3.3, I have extracted the following expressions of  $L_{JDPD}$  in the zero state ( $\Phi_+ = 0$ ) and in the bistable regime ( $\Phi_+ = \pi$ ), respectively:

$$L_0 = L_{lin} = \frac{\Phi_0 \beta}{4\pi I_C} \quad (4.5)$$

$$\frac{1}{L_{bist}} = \left(\frac{2\pi}{\Phi_0}\right)^2 \frac{d^2 U}{d\varphi^2} = \frac{1}{L_{lin}} - \left(\frac{2\pi}{\Phi_0}\right)^2 \beta \cos(\varphi) = \frac{1}{L_{lin}} - \frac{1}{L_{JJ}} \quad (4.6)$$

By employing all the previous expressions, the numerical simulations can be summarized in the plots in Fig. 4.4, that show the average resonance frequency (a) and the frequency shift (b) between the zero and bistable regime in terms of the transmission line length and the JDPD  $\beta$  ratio.

These outcomes point out that a decrease of the transmission line length leads an increase of the system resonance frequency and of the spectroscopic shift, while an increase of the  $\beta$  ratio leads to an increase of the spectroscopic shift but does not affect the resonance frequency. Inside the borders set by conditions (a.) and (b.) it is thus possible to design JDPD with different  $\beta$  ratios while keeping the circuit in the desired frequency range with a high and constant frequency shift between the zero and bistable state by following the arrow in Fig. 4.4(b). Further simulations that confirm this behaviour are portrayed in Fig. 4.5, where the profile of the resonance frequency is reported as a function of the transmission line length is shown, for different values of the  $\beta$  ratio in different JDPD states.

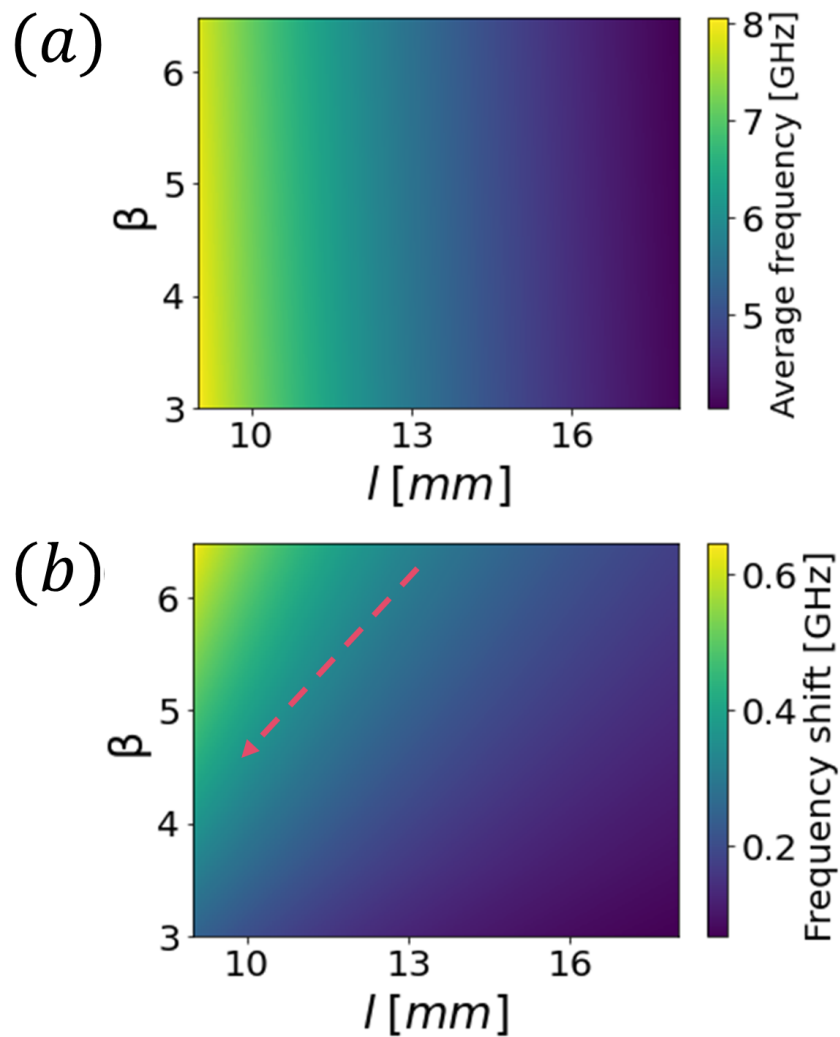


FIGURE 4.4: Spectroscopy simulation of the circuit in Fig. 4.3. (a) Average resonance frequency of the system for different combination of the length  $l$  and  $\beta$ . Average resonance frequency is defined by the average between the resonance frequency showed in the harmonic and the bistable state of the JDPD. (b) Resonance frequency shift when the JDPD is in the harmonic or bistable state. The orange arrow represents the direction to tread in order to keep the difference constant.

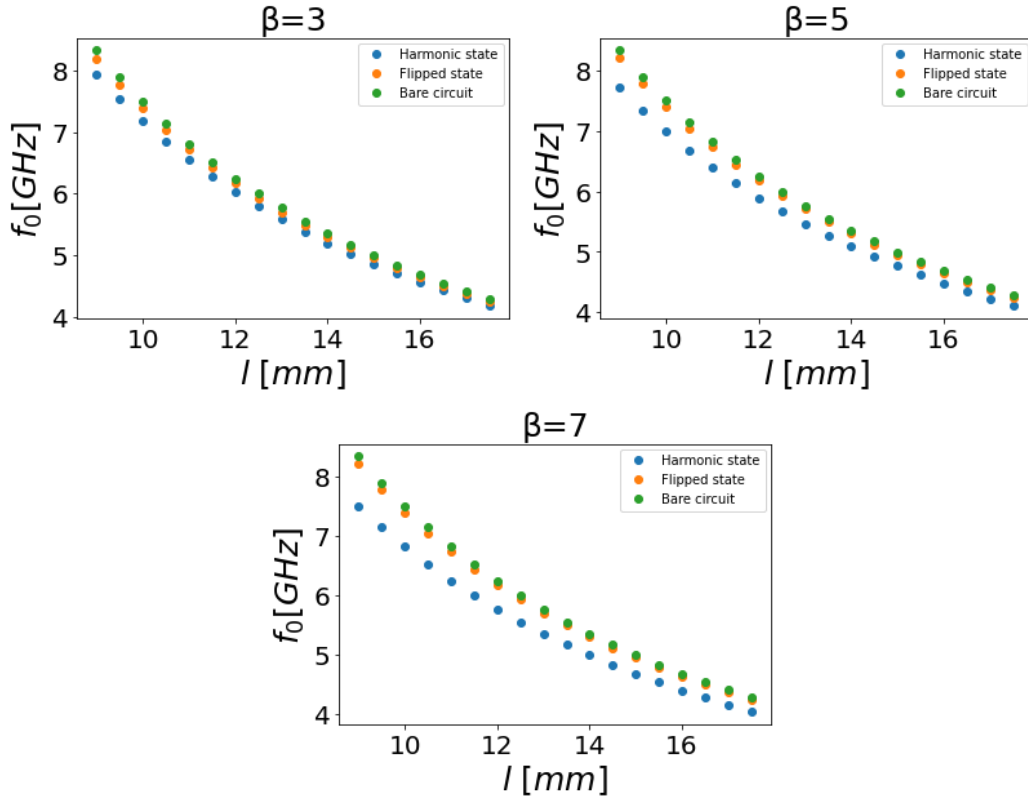


FIGURE 4.5: Plots of the system resonance frequency as a function of the transmission line length for different  $\beta$  and JDPD states. Each colour is related to a different condition or state of the JDPD: bare circuit without the JDPD (green), circuit with JDPD not perturbed by external fluxes (blue), circuit with JDPD in the bistable regime (orange). The plots show that an increase of  $\beta$  leads the harmonic curve to be more and more distant from the other two. This happens because in these simulations a  $\beta$  variation is achieved by modifying the JDPD linear inductance energy  $E_L$  while keeping the critical currents and thus the Josephson energy  $E_J$  fixed. Consequently, a variation of  $\beta$  leads to a change of the concavity in the harmonic state, leaving the bistable state unperturbed.

Keeping these results in mind, I have made a step towards a more efficient and realistic circuitual model by replacing the simple transmission line with a Coplanar Waveguide (CPW) [55]. Coplanar waveguides are a type of electrical planar transmission line which can be fabricated using the well known printed circuit board technology, and are used to convey microwave-frequency signals. Conventional coplanar waveguides consist of a single conducting electrode deposited above a dielectric substrate, together with a pair of return electrodes, one to either side of the central electrode, as shown in Fig. 4.6. All three conductors are on the same side of the substrate, and hence are coplanar. The return conductors are separated from the central electrode by a small gap, which has a fixed width along the length of the line. CPWs play an important role in the field of CQED, where they allow for high field strength and thus strong coupling to superconducting qubits by confining a microwave photon to a volume that is much smaller than the cube of the wavelength [56]. In addition to that, they can also be employed as quantum buses to couple multiple qubits to each other thanks to their high quality factors [57] that allow to reduce possible interferences effects [13].

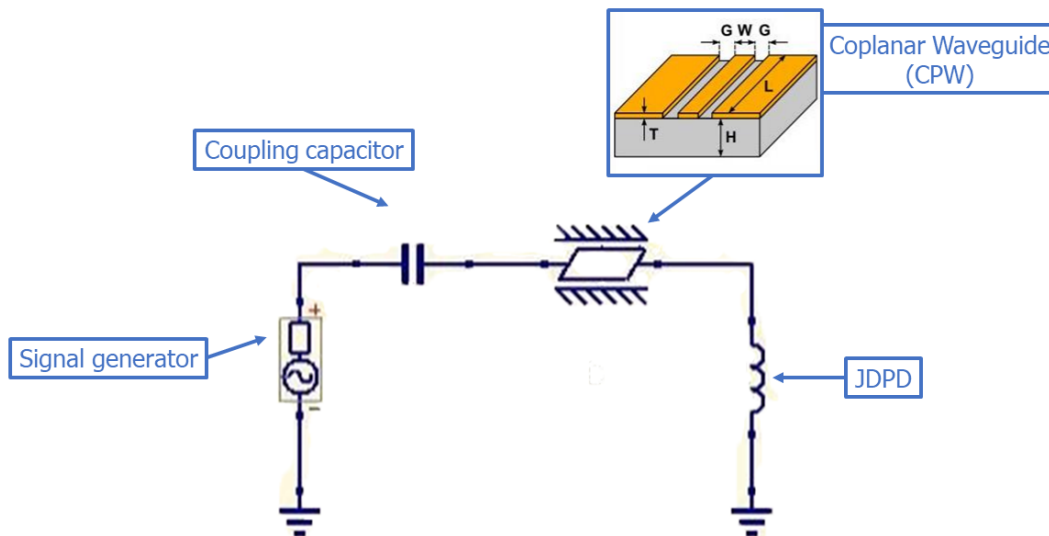


FIGURE 4.6: QUCS circuit schematic with a CPW. The chosen CPW geometric parameters for the simulations are the following: width of the central conductor ( $W = 11 \mu m$ ); dielectric gap ( $G = 7 \mu m$ ); conductor thickness ( $T = 0.135 \mu m$ ); substrate height ( $H = 200 \mu m$ ); electric permittivity ( $\epsilon_r = 11.9$ ); conductors resistivity ( $\rho = 1.72 \cdot 10^{-8} \Omega m$ ); losses tangent ( $\tan \delta = 10^{-7}$ ); roughness ( $\Theta = 0.1 \mu m$ ). These choices allow to have an impedance match with the signal generator fixed at  $Z_0 = 50 \Omega$ . The length  $l$  of the CPW electrode depends on the desired resonance frequency.

I have started looking for different spectroscopy circuits that can be connected to the same feed-line in the final chip in order to test the JDPD feasibility in a parallel configuration, like the one depicted in Fig. 2.11, where different JDPD through different quantum buses are linked to the same feed-line. These various circuits have to satisfy the mentioned criteria (a.), (b.) and simultaneously possess resonances that do not overlap with each other in any of the JDPD state. An overlap, in fact, not only makes two ports resonant to the same signal, but can also lead to interference between the two circuits.

To achieve the mentioned goals I have conducted S parameters simulations of the circuit in Fig. 4.6 both numerically and through the QUCS simulator. Differently from the previous circuit in Fig. 4.3, the transmission line is replaced by a CPW with the properties indicated in Fig. 4.6.

The numerical simulations are aimed to evaluate the effects of replacing the transmission line with a CPW. The results are shown in Fig. 4.7 where the resonance frequency and of the spectroscopic shift are reported as a function of the CPW track length. Comparing the plots in Fig. 4.7 with those reported in Fig. 4.4, 4.5 an overall consistency between the various numerical approaches can be noticed. Nonetheless there are some slight variation due to the particular geometrical structure of the CPW. The CPW replacement, in fact, lowers the length  $l$  needed to reach a certain frequency range, due to the dielectric gap between the conductive walls that leads to a  $c_l = c/\epsilon_r \neq c$ . Additionally, the spectroscopic shift curve is shifted to lower values of the CPW length  $l$  in different ways depending on the  $\beta$  ratio.

Further simulations have been executed through the QUCS simulator in order to extract some possible configurations that better satisfy the above mentioned conditions. After checking that the numerical results reproduce with a good approximation the spectroscopy behaviour of the circuit, three different circuit configurations have been extracted. In Fig. 4.8 the estimated resonances for the two different JDPD states under study are reported for fixed values of  $\beta$  and  $l$ . All the three layouts satisfy conditions (a.), (b.) and are also characterised by different  $\beta$  ratio. This means that it is possible to fabricate and analyse various JDPDs characterised by various  $\beta$  ratio, in order to evaluate the significance of this parameter on the circuit performance.

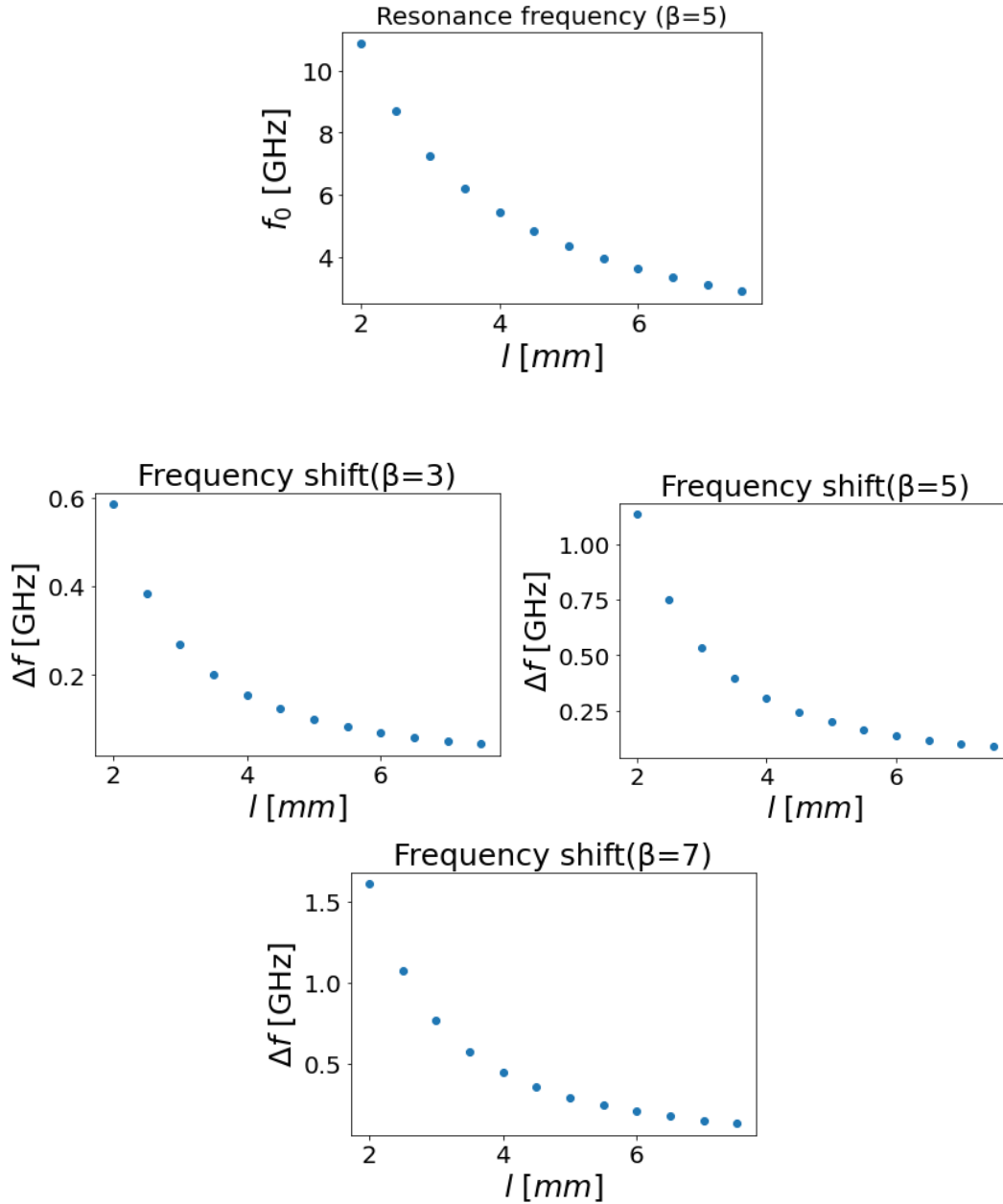


FIGURE 4.7: Numerical simulation of the circuit with CPW characterised by the parameters listed in Fig. 4.6. The upper plot shows the circuit resonance frequencies for different values of the CPW length, that is independent from the ratio  $\beta$ ; the lower plots represent the spectroscopic shift between the harmonic and bistable regimes of the JDPD for different values of the CPW length and of the  $\beta$  ratio. The latter plots highlight that in order to design circuits with various  $\beta$  ratios, while keeping similar spectroscopic shift, it is necessary to adequately decrease the CPW length if the  $\beta$  ratio increases.

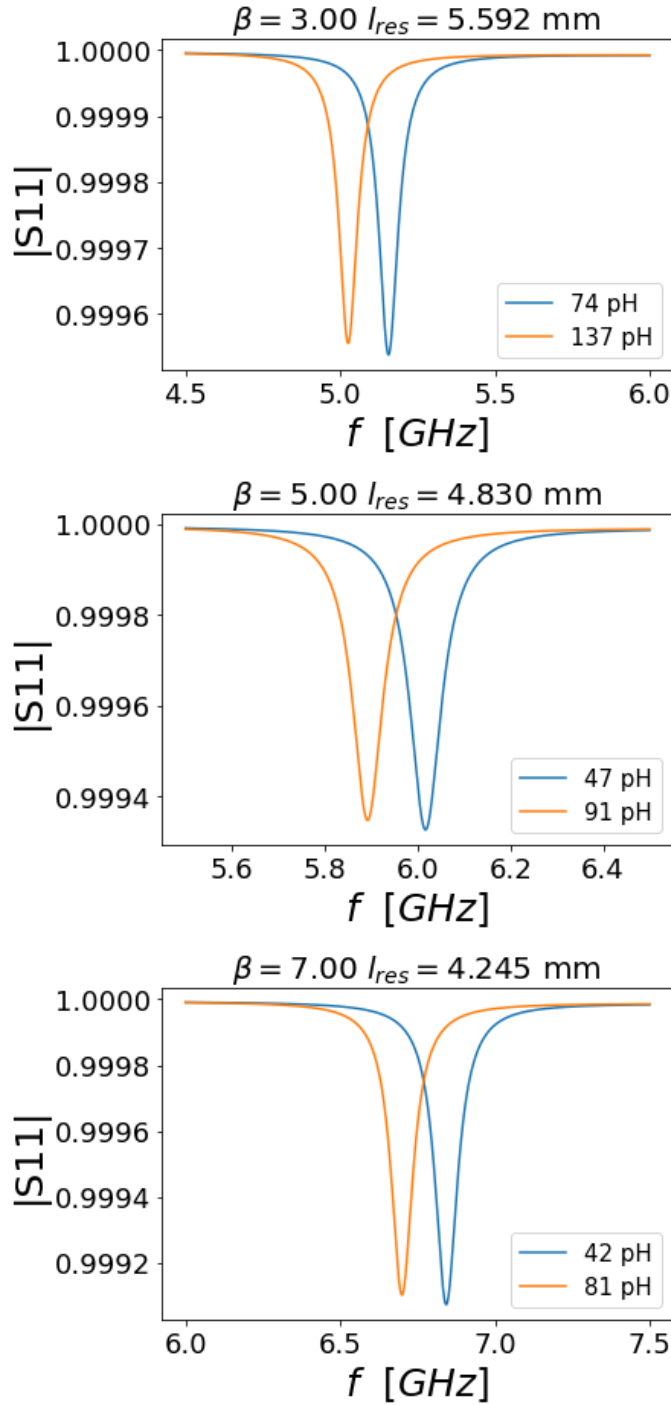


FIGURE 4.8: QUCS simulation of the circuit in Fig. 4.6. The plots show the resonances in the harmonic and bistable state for fixed values of CPW length and beta ratio of the JDPD chosen to be realized in the final chip. The shift in the frequency domain between the dips related to each pair  $(l_{CPW}, \beta)$  is always near  $150\text{MHz}$ , which is a shift that in principle allows to experimentally distinguish the two states with the available measurement set-up. The resonance frequencies as well as the spectroscopic differences that result from the QUCS simulations are slightly lower than the values obtained in the numerical simulations. This discrepancy is caused by approximating the CPW as an LC oscillator in the numerical simulations, which gives an underestimate of its effective capacity and inductance.

## 4.2.2 Interdigitated capacitor

Another component that I have estimated is the coupling capacitor that links the signal generator to the rest of the circuit. Given the dimensions and the geometry of the circuit, the ideal kind of capacitor is the interdigitated capacitor [58]. The interdigitated capacitor is an element made up of microstrip lines arranged as depicted in Fig. 4.9 in order to produce a capacitor-like behaviour between the fingers that compose the system. The coupling capacitor is linked to the current that gets to

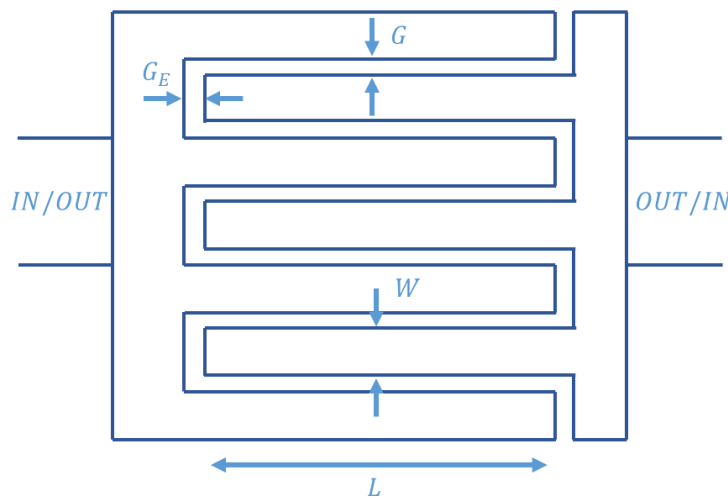


FIGURE 4.9: Schematic representation of an interdigitated capacitor. The long conductors or “fingers” provide coupling between the input and output ports across the gaps. Typically, the gaps  $G$  between fingers and at the end of the fingers  $G_E$  are the same. The length  $L$  and width  $W$  of the fingers are also specified. Since the conductors are deposited on a substrate, its characteristics will also affect the performances.

the JDPD and to the external quality factor of the system. The external quality factor is a fundamental parameter of the cavity resonator; it represents the coupling strength between the cavity resonator and waveguide carrying the input signal. In particular, it determines the electromagnetic power radiated from the cavity to the waveguide. In the case of superconducting cavities, the external  $Q$  is especially important because the internal loss of signal power is negligible in comparison to the radiated power, and the bandwidth of the system is determined by the external quality factor [59].

The best capacity value is thus the one that maximizes the quality factor while maintaining the current across the JDPD below the critical current of the Josephson junctions, considering the attenuation across the Triton lines in Fig. 3.8. By using QUICS, I have simulated the current passing across the JDPD and the quality factor of the

system for different values of the coupling capacity. The results of the QUCS simulations for a fixed attenuation of  $-90\text{ dBm}$  are shown in Fig. 4.10, which reports the plots of the current (a) as a function of the frequency for different values of the coupling capacity, of the maximum current (b) across the JDPD and of the external quality factor (c) as a function of the coupling capacity. In particular, the plot in Fig. 4.10(b) shows that with an attenuation of  $-90\text{ dBm}$ , no value of the coupling capacity leads to the passage of a current higher than  $2.2\ \mu\text{A}$ . An attenuation of  $-90\text{ dBm}$  can be easily reached through the VNA considering also the attenuators along the input lines. Additionally, given the JDPD form, the input current splits along the two independent branches of the circuit leading to a further reduction of the risk of incurring in a Josephson junction switch. This means that according to the plot of the external quality factor in Fig. 4.10(c), it is convenient to choose the lowest possible value of capacity in order to have the highest quality factor. By taking into account the dimensions of the chip allowed by the fabrication process and the typical values of interdigitated capacitors [60] the minimum feasible capacity is of  $10\text{ fF}$ . Before starting with the conclusive design of the chip, the circuit parametrization has been tested through additional simulations performed by using Ansys HFSS. Ansys HFSS is a 3D electromagnetic simulation software for designing and simulating high-frequency electronic products such as microwave components, high-speed interconnects, filters, connectors and printed circuit boards. The program has been employed to simulate the electric field inside the CPW with the border conditions given in the previous simulations (Fig. 4.11(Top)) and its resonance frequency as a function of the JDPD inductance (Fig. 4.11(Down)). The results further prove that the border condition set on the CPW leads the latter to act as a  $\lambda/4$  resonator and that the resonances are consistent with the results in Fig. 4.8(Down) for a difference in the order of hundreds of  $\text{MHz}$ , which still keep the resonance in the desired range of  $[4 - 8]\text{ GHz}$ .

All the simulations performed in this section do not take into account the superconductivity behaviour of the circuit components. Both QUCS and HFSS, in fact, do not allow to simulate superconducting quantum circuits and thus some slight difference are expected between the simulations and the circuit at temperature below the critical temperature of its superconducting components. Nonetheless, the room temperature behaviour predicted by the simulations guarantee that the conditions initially mentioned should be respected even with the variation occurring when the circuit enters its superconducting state, allowing the start of the chip fabrication.

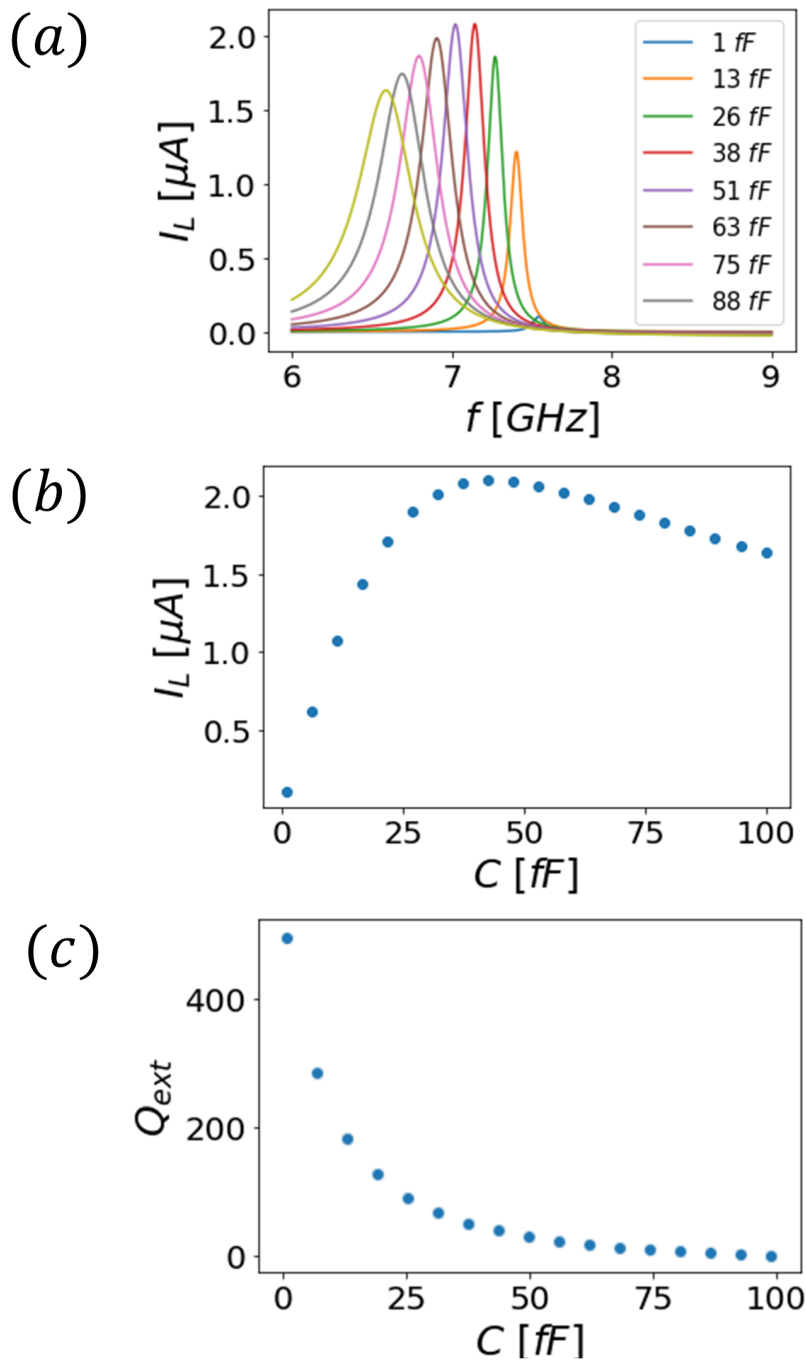


FIGURE 4.10: QUCS simulations of the circuit in Fig. 4.6 for an attenuation of the signal source of  $-90$  dBM, which is a typical value that can be used in the experiments. (a) Plots in the frequency range of the current  $I_L$  entering the JDPD for different values of the coupling capacitance. (b) Trend of the  $I_L$  maxima for different values of the coupling capacitance. This simulation proves that given the initial attenuation, for no values of the coupling capacitance the current exceeds the threshold of  $5\mu A$ . (c) Curve of the external quality factor [34] related to the CPW for different values of the coupling capacitance.

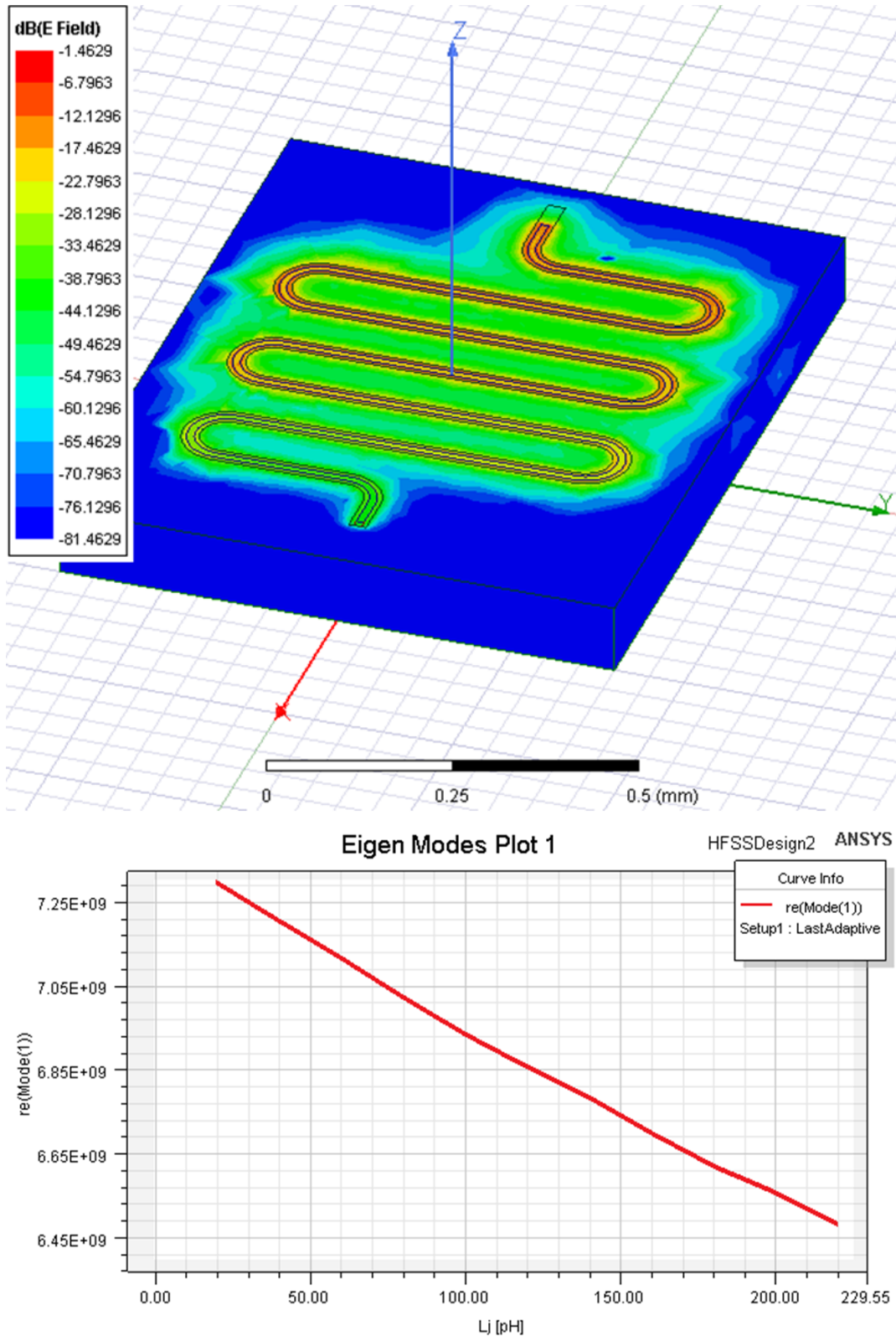


FIGURE 4.11: HFSS simulations of the CPW in the spectroscopy circuit with  $l = 4.245 \text{ mm}$ . (Up) Simulation of the electric field distribution along the CPW. A maximum of the electric field is expected at the capacitive pole and a node at the inductive pole. (Down) Simulation of the spectroscopy circuit resonance for different values of the JDPD inductance. The resonance values are coherent with the values obtained from QUCS simulations.

### 4.3 Layout and fabrication

Taking into account the previous simulations it was possible to produce four chips layout through Klayout, an open source editor specific for circuit design. The general architecture of these chips is shown and described in Fig. 4.12 where it is possible to distinguish the fundamental units that made up the chips. The chosen value of CPW length and JDPD  $\beta$  ratio are the one depicted in Fig. 4.8, taken in various combination, as shown in Fig. 4.12. Differently from the simulations reported in Section 4.2, in this case the  $\beta$  ratio is changed by adequately tuning the Josephson junctions critical current while keeping the equivalent inductances fixed for every JDPD in the chip. The linear inductance has been fixed at  $200 \text{ pH}$ , while the critical currents for the various JDPDs are  $I_C = 2.4 \mu\text{A}$  for  $\beta = 3$ ,  $I_C = 4 \mu\text{A}$  for  $\beta = 5$  and  $I_C = 5.5 \mu\text{A}$  ifor  $\beta = 7$ , which are the values indicated in the plots of Fig. 4.8. Different combinations of the pair  $(l, \beta)$  are arranged into the chip, where it is possible to note that there are circuits isolated from the others and multiple circuits linked to each other through a unique feed-line. This architecture allows to analyse the functioning of the JDPD both as a stand-alone circuit and in a parallel arrangement. The design of the circuit can vary also for the DC line configuration employed to drive the JDPD from one state to the other. There are two types of DC line configurations: the first type is the "U configuration" where the two ends of the line are linked to two different pads, and the second type is the "L configuration" where one end of the line is linked to a pad and the other to the ground plane of the chip through an hole inside the metallic layers. Different DC line configurations have been inserted in order to test which layout offer the better maneuverability of the fluxes provided to the JDPD. Each of the four chips differs from the other in terms of circuit parameters, DC line types and arrangement of the latter. In addition to those, some chips present the so called "Mots", which are holes inside the superconducting layer that protect the chip from potential flux noise by exploiting the flux quantization of superconductors. Other elements inserted to improve the chip efficiency are the "Bridges", which are metallic layers that go above the feed-lines which connect the circuits to the pads. These components guarantee that the ground plane is nominally a zero for the voltage.

The fabrication of the various chips had been performed by SeeQC in the United States through photolithography process. Photolithography is a process used in microfabrication to pattern specified design on a thin film or the bulk of a substrate. It uses light to transfer a geometric pattern from a photomask to a photosensitive chemical photoresist on the substrate. Multiple copies of the different chips were later delivered to our lab in Naples, where it have been measured and analysed as

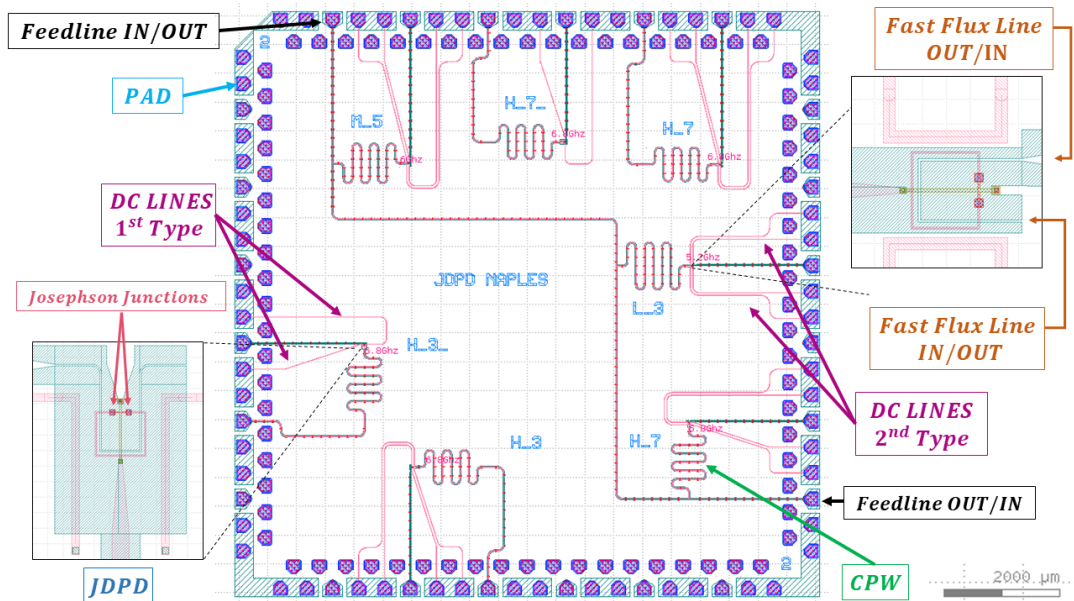


FIGURE 4.12: Layout of the chip #2 in Klayout environment. Each color represents a different layer that can belong to one of the following polarity: positive (red-purple), negative (green). Positive layers indicate area where the material is present; negative layers indicate areas where there is absence of the background material. Every circuit is composed of a CPW and a JDPD in series, which are coupled through an interdigitated capacitor to one of the pads on the border of the chip. The pads are consequently bonded to the electronic set-up of the cryostat that allows to create a connection with the VNA at room temperature. The pink lines on the sides of the JDPD represent the "DC lines" that drive the magnetic fluxes across the respective loop of the JDPD. The white lines inside the green layer represent the "fast flux lines", which go below the corresponding JDPD and couple with both its loops. Each circuit is labelled with a certain sequence of symbols. The letter indicate the resonance frequency of the CPW in the circuit. It is indicated by the letters: "H", "M" or "L" which respectively stand for "High" (6.8 GHz), "Medium" (6 GHz), "Low" (5.4 GHz), which are the values indicated in the simulations of Fig. 4.8. The numbers indicate the  $\beta$  ratio of the JDPD. The underscore at the end indicates if the DC lines are of 2<sup>nd</sup> type or not. The materials employed are the Niobium Nb for the superconducting parts (ground, Josephson junctions ends, feed-line core, lines), the Aluminum-Oxide AlOx as insulator for the Josephson junction barrier, the Niobium-Nitride NbNx which is a high inductance material used for the central inductor of the JDPD and Gold-Palladium Pd/Au for the pads.

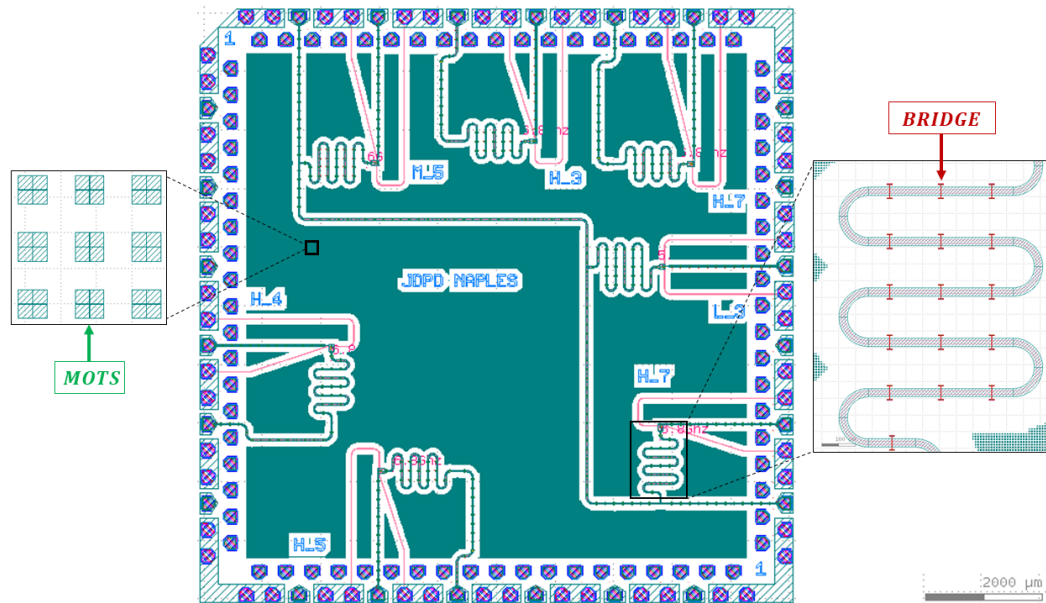


FIGURE 4.13: Layout of the chip #1 in Klayout. Differently from the fourth chip, the ground plane is covered of mots as highlighted by the zoom on the left. The zoom on the right shows the bridges that are arranged through one of the CPW in the chip.

described in the following sections. Some microscope images of the essential components upon the chips are shown in Fig. 4.14.

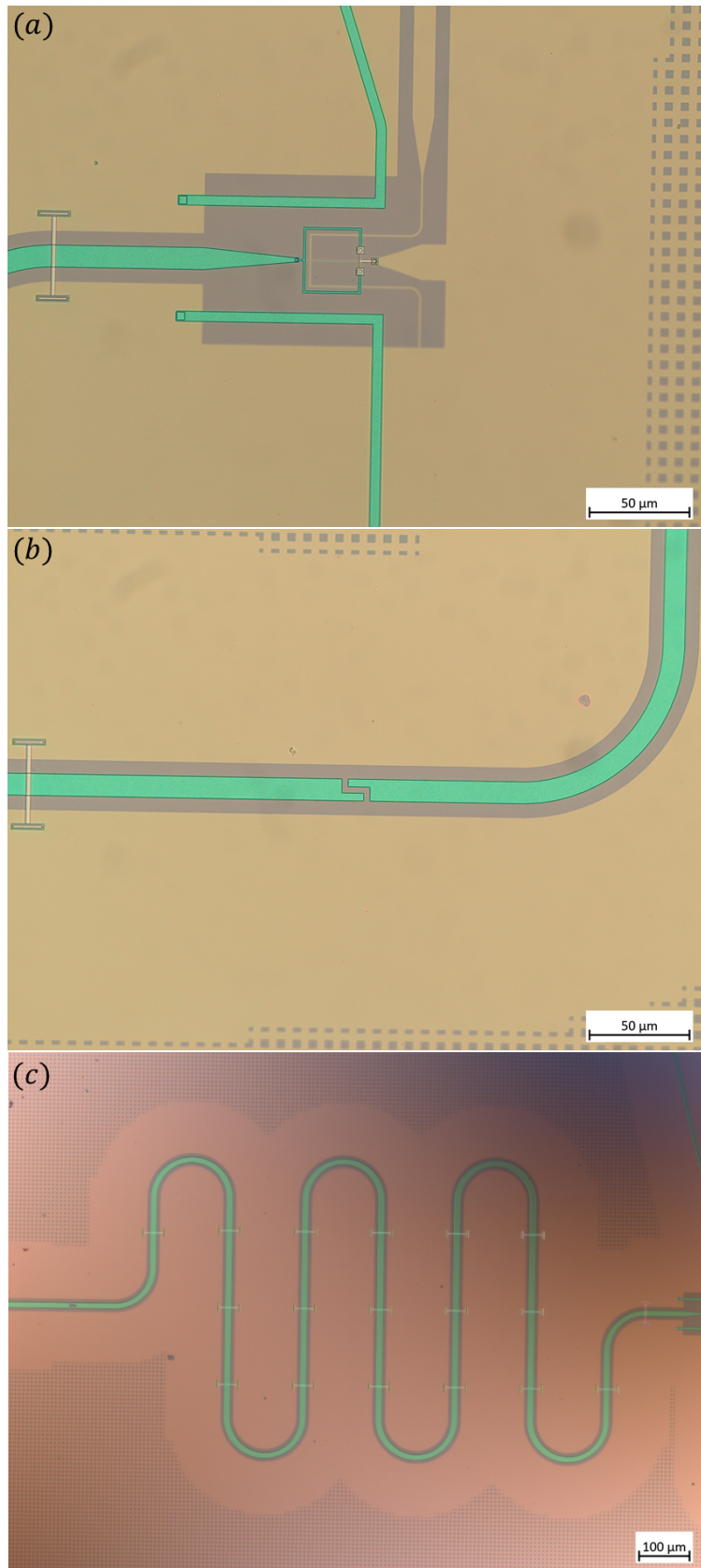


FIGURE 4.14: Images taken with ZEISS optical microscope of the JDPD (a), the coupling capacitor (b) and CPW (c) related to the H\_7\_circuit of Chip 2

## 4.4 Spectroscopy circuit and Josephson Digital Phase Detector dynamics

In this Section, additional Python simulations will be discussed with the aim of studying the spectroscopy behaviour of the designed circuits, schematically represented in Fig. 3.1. These simulations aim at providing some reference terms concerning the experimental measurements reported in the next Chapter, in order to create a direct link between the latter and the JDPD dynamics. The model used for the following simulations is based on the analogy between the circuits and an LC oscillator, described in Sec. 3.1. In particular it employs Eq. 3.1 to define the resonance frequency of the circuit, the potential energy definition in Eq. 2.20 to represent the JDPD dynamics and Eq. 3.3 to evaluate the contribution of the JDPD to the resonance frequency of the system. To provide the phase particle position, required by Eq. 3.3, I have assumed that the domain of positions coincides with the minima of the JDPD potential energy defined by Eq. 2.20. Therefore, in this model the passive inductance of the JDPD loops, the plasma oscillation of the phase particle [20], the coupling capacity and the passive capacitance of the Josephson junctions have been neglected as well as. Additionally, the Josephson junctions energy  $E_J$  and inductance  $L_J$  are assumed to be constant and thus insensitive to the external magnetic fields. These series of approximations are consistent with the features of the designed circuits where the inductance of the JDPD central inductor is much higher than the kinetic inductance of the other JDPD branches and the Josephson junctions in the circuit are characterised by a low capacitance.

This allows to evaluate the dynamics of the circuit for different values of the applied fluxes  $\Phi_{\pm}$  and  $\beta$  ratio. The first simulations that I have performed, in fact, aim at studying the dynamics of the JDPD phase particle for different values of  $\Phi_{+}$ . The phase particle represents the phase difference between the ends of the central linear inductor  $L$  in Fig. 2.8, which plays the role of the dynamical variable of the JDPD according to Eq. 2.19. The spectrum of the central inductor phase  $\varphi$  can be extracted by evaluating the minima in the potential energy curve for different values of  $\Phi_{+}$ , according to the model described in the introduction of this section. Assuming the JDPD potential energy is symmetric ( $\Phi_{-} = 0, I_{C1} = I_{C2}$ ), the outcome of this simulation for a JDPD with  $\beta = 7$  is reported in Fig. 4.15. The obtained results show that different values of  $\Phi_{+}$  correspond to different positions of the phase particle. In particular, to some values of the flux  $\Phi_{+}$  can correspond multiple distinct position of the phase particle, due to the multiple minima of the potential energy profile for those fluxes. This means that the application of the flux  $\Phi_{+}$  to tune the phase difference  $\varphi$  can provide different outcomes depending on the initial condition.

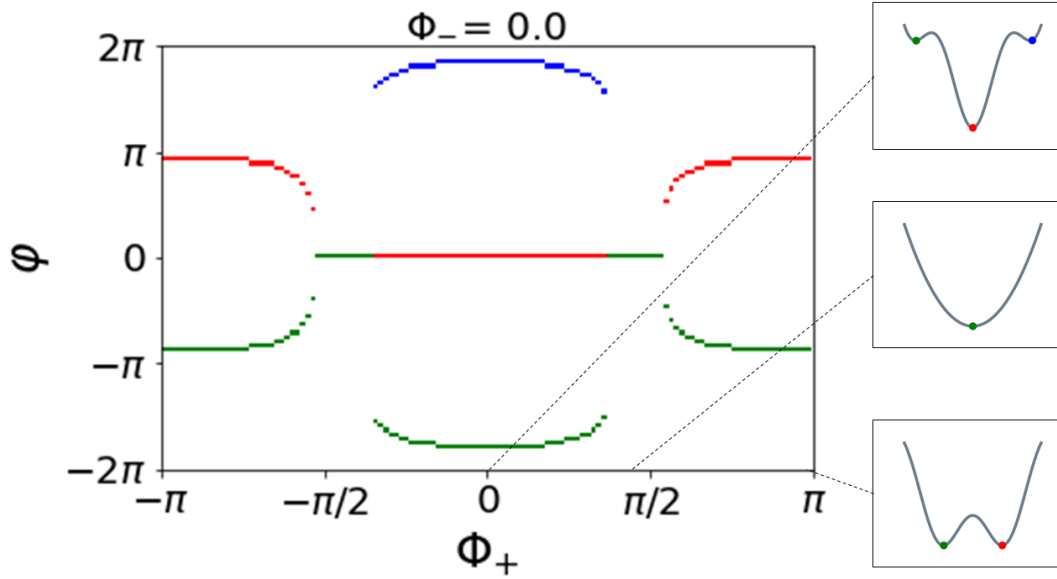


FIGURE 4.15: The graph on the left shows a sweep on the flux  $\Phi_+$  for  $\Phi_- = 0$  of the phase  $\phi$  across the JDPD central inductor. Each colour represent a position of the phase particle related to a different potential energy minima, as highlighted by the potential energy graphs on the right. In particular, the colours: green, red and blue are assigned to the first, second, third minimum found on the potential energy profile by going from  $-2\pi$  to  $2\pi$ , respectively. For these simulations, the circuit is assumed to have a ratio  $\beta = 7$  and no asymmetries between the Josephson junctions ( $I_{C-} = 0$ ). For  $\Phi_+$  near 0 the potential energy has three minima as in Fig. 2.9(a) and thus the phase particle can be trapped in three different positions. For  $\Phi_+$  near  $\pi/2$ , instead, the potential energy turns into the harmonic state of Fig. 2.9(b) where the phase particle is always near the origin. For  $\Phi_+$  larger than  $\pi/2$  the potential energy starts to show the bistable behaviour depicted in Fig. 2.9(d) where the phase particle falls in one of the two dips, leading to equal and opposite phases across the linear inductance.

In addition to  $\Phi_+$ , there are also other quantities that can be exploited to manipulate the JDPD dynamics. According to Eq. 2.20, there are the asymmetries  $\Phi_-$  and  $E_{J-}$ , which break the parity symmetry of the potential energy, and the  $\beta = 2E_J/E_L$  ratio. The latter parameter, which depends on the JDPD structural properties, such as the Josephson junctions energy  $E_J$  and the equivalent inductance  $L$ , is linked to the height of the potential well of the two minima in the bistable regime, as shown in Fig. 4.16. This feature allows to increase the separation between the two minima and to avoid "phase slips" (the phase particle can jump from one minimum to the other) between the two potential wells due to thermal escape or quantum tunneling events. From this point of view an increase of  $\beta$  seems to be convenient. On the other hand, some effects due to the backactions have to be considered. In this case the backaction

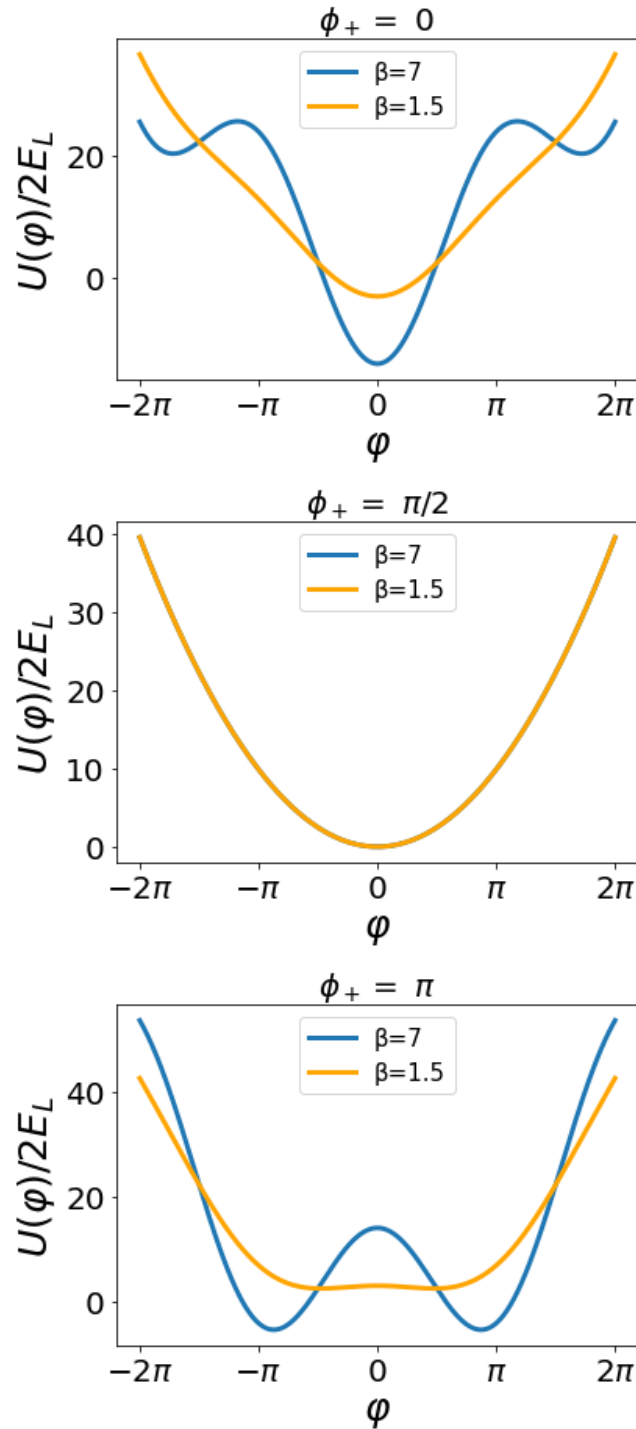


FIGURE 4.16: These plots show the JDPD potential energy behaviour for different  $\beta$  values, as reported in each panel, in the various states required in the read-out protocol. For  $\Phi_+ = 0$  the case with the highest  $\beta$  shows three different minima, while the other just one minima in 0. In the harmonic state the potential energy is defined just by the quadratic term that does not depend on  $\beta$  and thus the curves overlap. Finally, in the bistable state the potential energy profile with the highest  $\beta$  is characterised by the deeper dips and thus by the larger separation between the phase states related to the two minima.

is caused by the JDPD photons emission when the read-out is performed. In fact, the phase particle does not fall directly in the ground state of the selected potential well, but consecutively falls from the higher energy levels to the lower one in the well, producing a photon for each decay, like the JPM in Sec. 2.1.2. If the qubit under test is not transparent to the produced photons, the JDPD read-out can disturb the qubit state, lowering the fidelity of the read-out or making the read-out destructive. The best way to engineer the JDPD is thus to choose a  $\beta$  value such that the spectrum of the emitted photons from the JDPD is transparent to the qubit.

Accounting for the mentioned degrees of freedom that allow to manipulate the JDPD dynamics, I have executed various simulations in order to evaluate whether these "effects" have impact on the spectroscopic response of the system. In this context, starting from the "phase map" in Fig. 4.15, I have developed other numerical simulations in order to acquire the resonance frequency as a function of  $\Phi_+$  in different conditions. The results of these simulations for a JDPD with  $\beta = 7$ , is reported in Fig. 4.17, as a function of  $\Phi_+$  in the absence of asymmetries ( $E_{J-} = \Phi_- = 0$ ).

Without supplying magnetic fluxes to JDPD loops, the spectroscopy circuit can be defined by three different values of the resonance frequency, where each one is linked to one of the three different positions of the phase particle for  $\Phi_+ = 0$ . Due to the JDPD symmetry, the concavity of the minima on the sides (green and blue) is the same, leading to the same value of the resonance frequency according to Eq. 3.1, 3.3. Applying  $0 < \Phi_+ < \pi/2$  leads the potential energy to gradually converge to its harmonic regime for  $\Phi_+ = \pi/2$ , characterised by a single minimum. This manipulation is achieved with a continuous decrease of the central minimum concavity, that eventually goes to zero for  $\Phi_+$  slightly larger than  $\pi/2$ . Therefore, the resonance frequency follows the same trend as shown in Fig. 4.17. Successively, by further increasing  $\Phi_+$ , the potential energy profile evolves to a bistable curve characterized by two absolute minima, whose concavity continuously increases until  $\Phi_+ = \pi$ . Consequently, the resonance frequency of the system rises up again, reaching its maximum for  $\Phi_+ = \pi$ . These observations highlight the connection between the spectroscopy of the circuit in Fig. 3.1 and the dynamics of the JDPD. In Fig. 4.17, in fact, the JDPD state can be easily extracted by observing that in the unperturbed regime there are three archs where the red one is higher than the other two (green and blue in Fig. 4.17) which overlap and are related to the side minima, while in the bistable regime there are two overlapping archs which correspond to the two absolute minima in the potential energy curve. Nevertheless, in the experiments, there is no direct way to measure the actual  $\Phi_+$  that the JDPD experiences, and the only way to identify the JDPD state is through resonance frequency measurements. The height difference between the archs of the absolute minima in the unperturbed state and the bistable

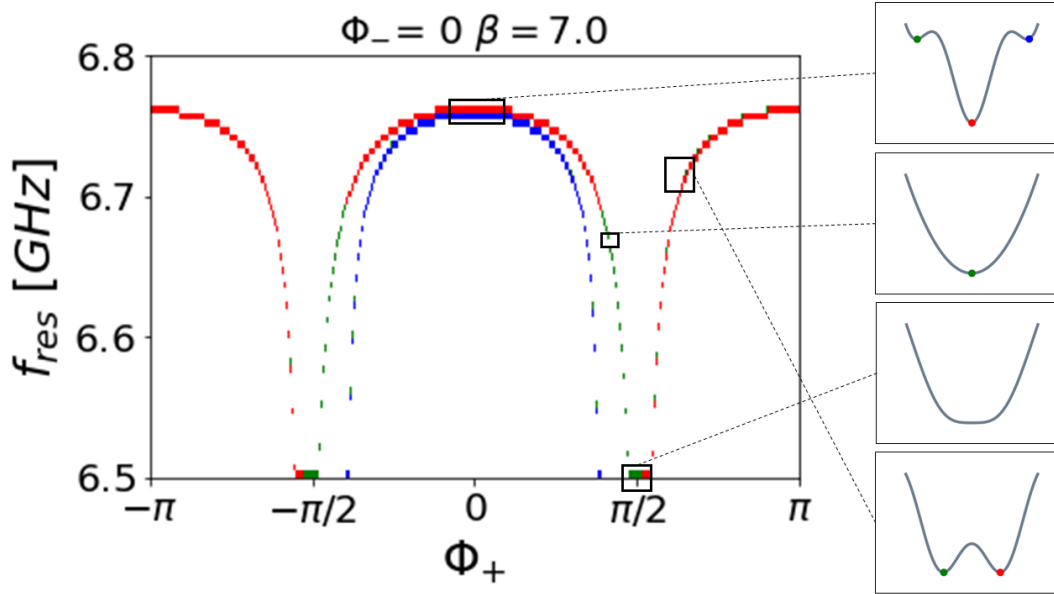


FIGURE 4.17: The graph on the left shows the resonance frequency of the JDPD device as a function of  $\Phi_+$ . The resonator in series with the JDPD is assumed to have a resonance frequency of  $f_0 = 6.8\text{GHz}$  and the JDPD to have a ratio  $\beta = 7$  and  $L = 200\text{pH}$ . The color map is equal to the one used in Fig. 4.15. The inductance exhibited by the JDPD is inversely proportional to the potential energy concavity related to the phase particle location on the potential energy profile. As a consequence, the resonance frequency of the system, defined by Eq. 3.1, is proportional to the concavity. This brings to the evolution shown in this figure, where the curves show similar value in all the range of  $\Phi_+$  except for  $\Phi_+$  near  $\pi/2$ , where during the transition from the harmonic to the bistable state, the potential energy will show a moment where the concavity of its absolute minima converges to 0.

state archs is of the order of  $0.6\text{MHz}$ , which is non discernible with the available experimental setup. This similarity creates an issue in the experimental measurements, since it is not possible to grasp which arch is related to the zero or to the bistable regime of the JDPD. It is thus necessary to make an initial guess and later verify its correctness through some specific protocols, introduced in Chapter 5, that allow to verify if the JDPD is in its bistable regime or not. Additionally, the symmetry of the potential energy in the bistable regime does not allow to distinguish in which well the phase particle is. In Chapter 5 I will describe the protocol employed to overcome this latter problem and to demonstrate the existence of the two wells.

As a next step I have studied the effects that other variables, such as  $\Phi_-$  and  $\beta$ , have on the resonance frequency of the circuit. First of all, I have analysed the effects of  $\Phi_-$  both on the JDPD potential energy and on the spectroscopy of the whole circuit. The results are reported in Fig. 4.18, where it is portrayed how the "phase map" in Fig. 4.15 change following the application of a  $\Phi_-$  on the system. Comparing the

plots in Fig. 4.15 and Fig. 4.18, it is possible to see that  $\Phi_-$  breaks the symmetry of the potential energy and tilt the potential in a direction that depends on the sign of  $\Phi_-$ . In particular  $\Phi_-$  can be employed to force the phase particle in certain positions through adequate tilt of the JDPD potential energy. This feature turns to be extremely useful in the context of the JDPD experimental validation where it allows to analyse the JDPD dynamics with different initial condition for the phase particle. Despite its usefulness in the preliminary experimental analysis of the JDPD, the tilt caused by  $\Phi_-$  is not something desired in the actual employment of the JDPD read-out protocol. The fidelity of the read-out protocol is sensitive to the possible asymmetries in the circuit because they create an absolute minimum in the bistable regime, as shown in the potential energy profiles of Fig. 4.18. This leads to a preference for the phase particle to fall in the deepest dip, which unavoidably disturbs the measurement. To overcome this problem, which in general can be caused by: trapped flux across the loops or fabrication issues ( $E_{J-} \neq 0$ ), an external  $\Phi_-^{sym}$  can be exploited. The tilt caused by unwanted asymmetries, in fact, can be corrected through an external  $\Phi_-^{sym}$  flux, which in principle can tilt back the potential energy profile in its symmetric regime. The mentioned tilt allowed by  $\Phi_-$  leads to some interesting effects on the spectroscopy response. In Fig. 4.19 the spectroscopy response of the circuit considered before is reported for different values of  $\Phi_-$ . The first feature that can be noted is that after a certain threshold, one of the three archs in the unperturbed state disappears. This happens due to the tilt on the potential energy profile, that avoids the trapping of the phase particle. Additionally, the height difference between the archs of the two minima in the bistable regime increases as  $\Phi_-$  increases. The application of  $\Phi_-$ , in fact, also leads to a symmetry break of the second derivative of the potential energy, that ultimately makes the spectroscopy archs related to the two minima in the bistable regime distinguishable. This latter feature is essential for the experimental validation of the JDPD bistable regime, therefore the protocol introduced in Chapter 5 will be based on this observation. Additionally,  $\Phi_-$  also change the widths of the spectroscopy archs. This is another consequence of the tilt on the JDPD potential energy that leads to a certain distance between the spectroscopy archs and thus to different widths. Despite the various effect of  $\Phi_-$  on the system spectroscopy, the height difference between the archs in the unperturbed state and the bistable regimes keeps being experimentally non discernible for any values of  $\Phi_-$ . The only case where it is expected a visible difference between the archs height is by decreasing the  $\beta$ , as shown in Fig. 4.22. The plots of Fig. 4.20, 4.21, 4.22 portray the simulations that I have performed of the circuit spectroscopy for different values of  $\beta$  and  $\Phi_-$ . The plots show that for extremely low values of  $\beta$  the height difference is around hundreds of  $MHz$  for  $\Phi_- = 0$ , which can be measured with the available

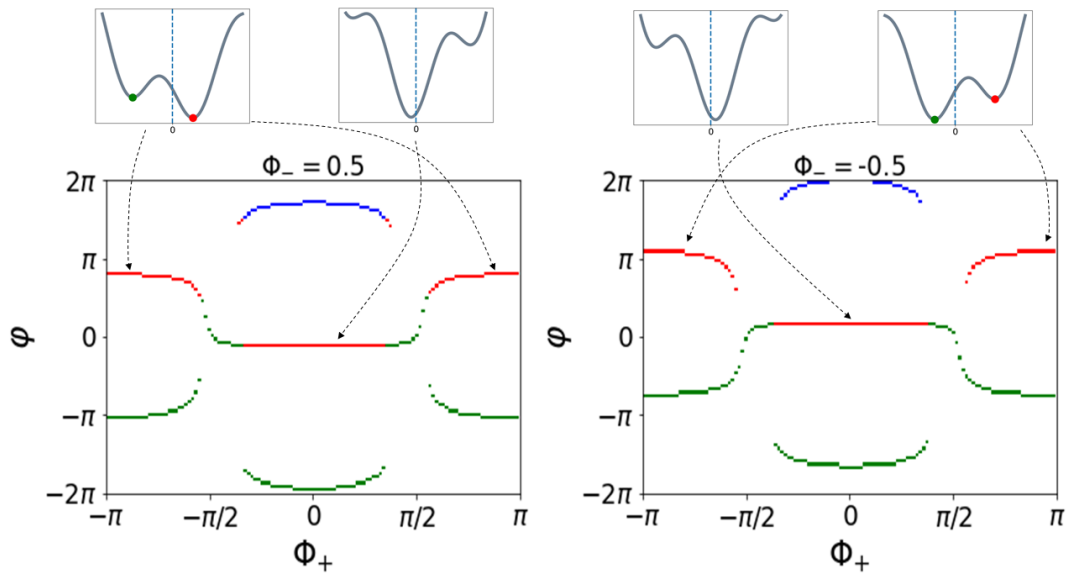


FIGURE 4.18: The graphs on the left and on the right show the spectrum of the possible JDPD phase state depending on  $\Phi_+$ , for  $\Phi_- = 0.5$  and  $\Phi_- = -0.5$  respectively, for  $L = 200 \text{ pH}$  and  $\beta = 7$ . Compared to the values for  $\Phi_- = 0$ , represented in Fig. 4.15, it is possible to see that  $\Phi_-$  shifts the spectra up or down on the y axis, for positive or negative values respectively. This is caused by the effect of  $\Phi_-$  on the JDPD potential energy in Eq. 2.19, where it introduces a shift in the cosine and sine argument that brings a shift on the whole potential energy as well as a tilt, due to the harmonic properties of the trigonometric functions. The tilt allows to have an absolute minima in the system for  $\Phi_+ = \pi$ , which leads the phase across the linear inductance to have a favored state.

experimental setup. This is a consequence of the Josephson junctions that have less and less effects on the JDPD dynamics as  $\beta$  decreases. The  $\beta$  ratio in Eq. 2.20, in fact, represents the magnitude of the periodic term in the JDPD potential energy definition, which comes from the Josephson junctions inside the system. The fading of this periodic term gradually leads to an harmonic potential energy profile for any  $\Phi_+$  applied to the system, and thus to a progressive disappearance of the bistable behaviour. In particular the concavity of the minima in the bistable regime is reduced, as shown in Fig. 4.16, which ultimately leads to archs of lower height compared to the one for  $\Phi_+ \in [-\pi/2, \pi/2]$ . Additionally, for such low  $\beta$  the height difference can also be tuned by providing an appropriate  $\Phi_-$  that decreases the height difference in the range  $[0, \pi]$  and increases it in the range  $[\pi, 2\pi]$ , as shown in Fig. 4.20. This is a consequence of the tilt that can change the concavity of the potential energy minima, as already observed for  $\beta = 7$  in Fig. 4.19.

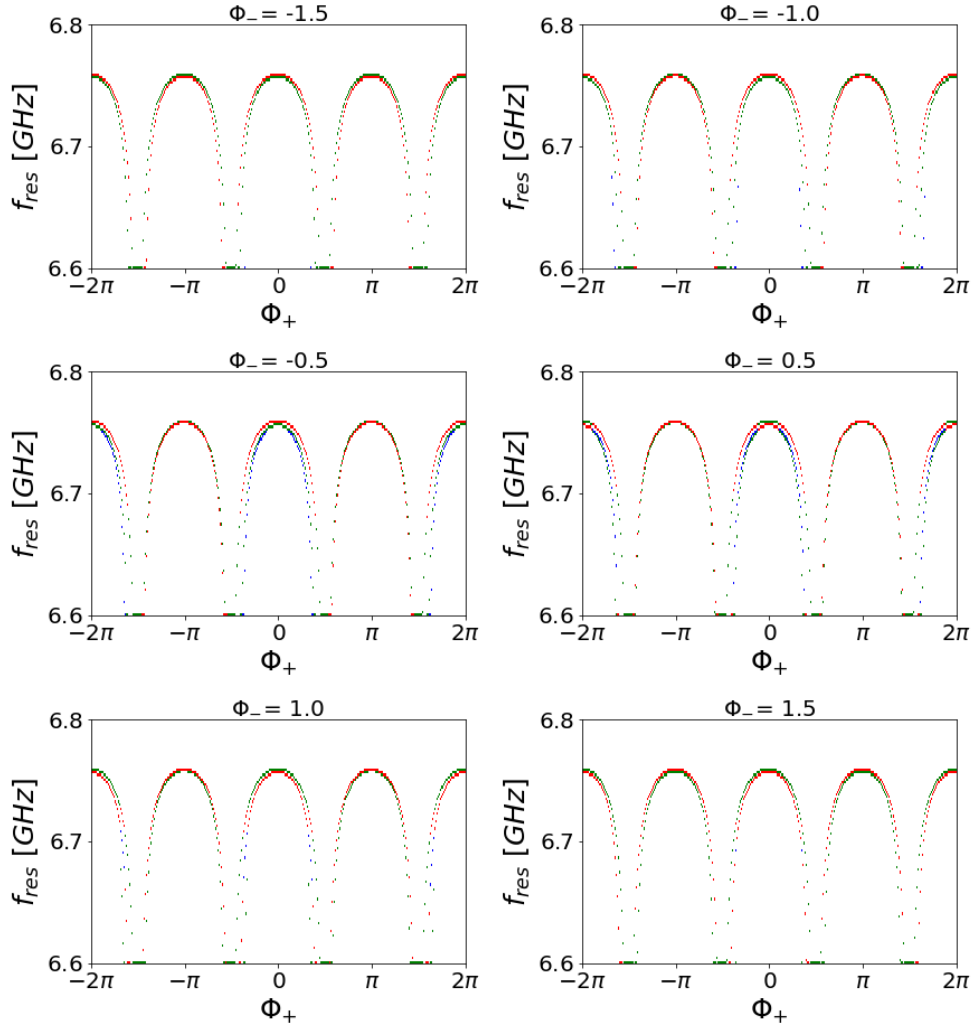


FIGURE 4.19: Expected resonance patterns for a sweep of  $\Phi_+$  in the range  $[-2\pi, 2\pi]$  and for different values of  $\Phi_-$ , as indicated on the top of each panel, for the spectroscopy circuit with a JDPD with  $\beta = 7$  and  $L = 200 \rho H$ . The colormap is analog to the one in Fig. 4.17. The results are consistent with the fact that in the bistable regime the red and green curves are inverted depending on the  $\Phi_-$  sign.

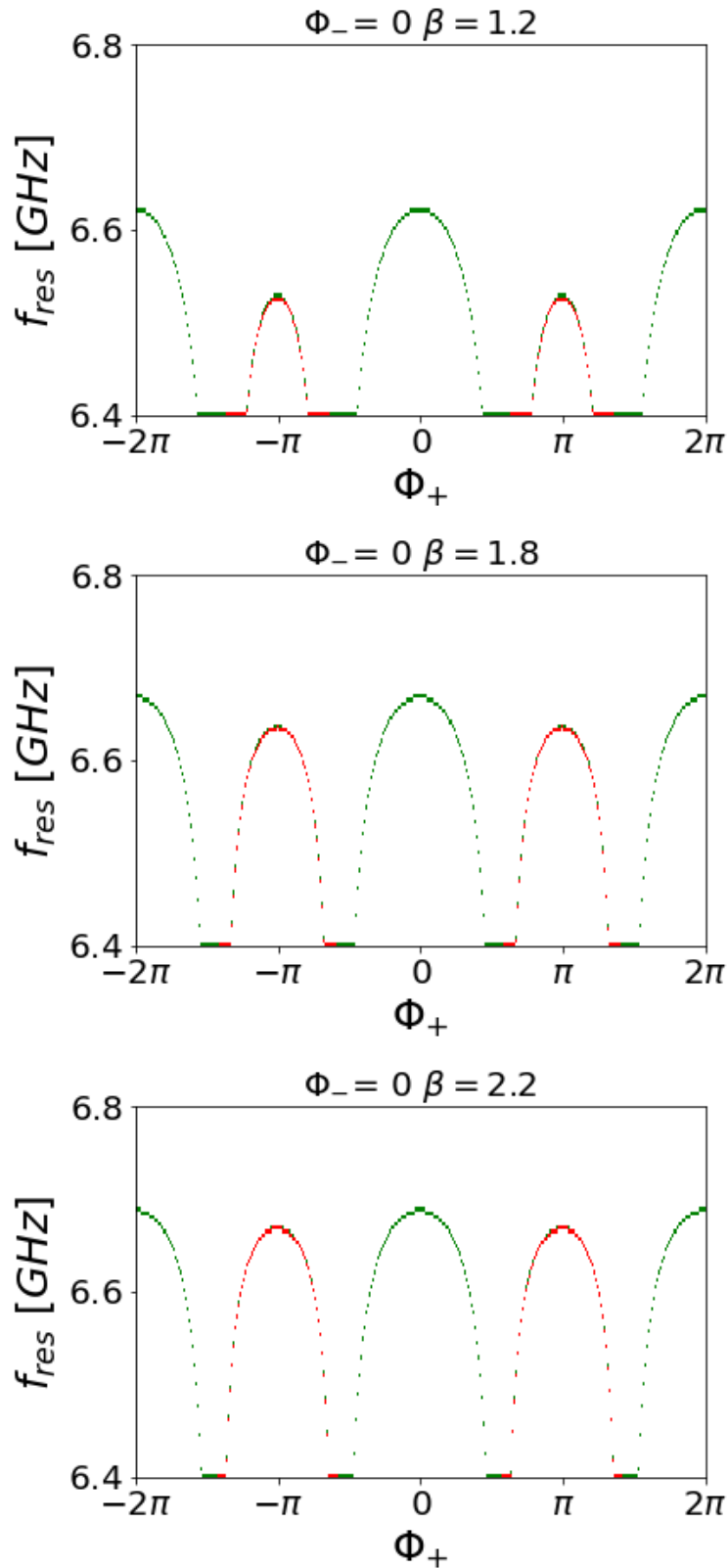


FIGURE 4.20: Theoretical spectroscopy behaviour of the circuit in Fig. 3.1 with a resonator of frequency  $f_0 = 6.8$  GHz, a JDPD with no geometrical asymmetries ( $J_- = 0$ ),  $L = 200$  pH and  $\beta = 1.2, 1.8, 2.2$ . Compared to the spectroscopy shown in Fig. 4.17 with  $\beta = 7$ , the system presents just one minimum instead of three for  $\Phi_+ = 0$  and also a difference in the resonance frequency between the harmonic state and the bistable state that is inversely proportional to the ratio  $\beta$  of the JDPD.

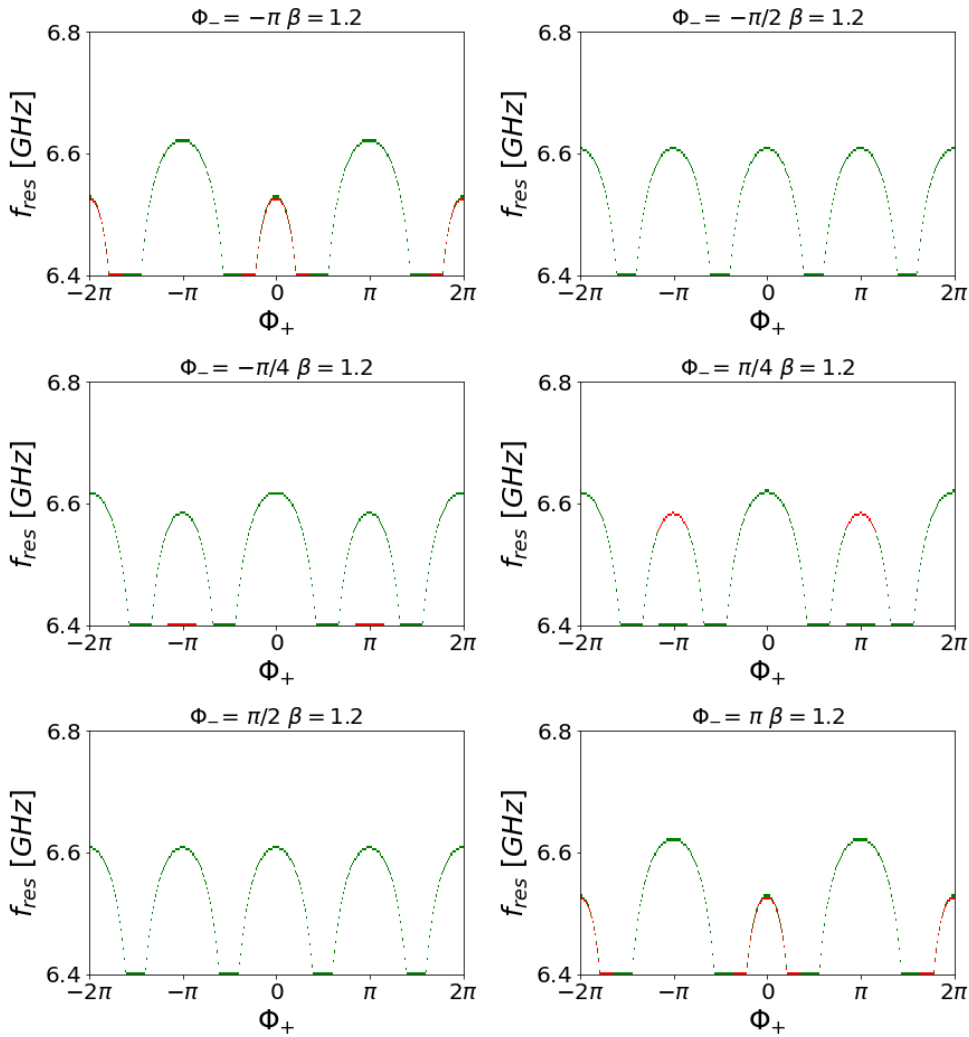


FIGURE 4.21: Theoretical spectroscopy behaviour of the circuit in Fig. 3.1 with a resonator of frequency  $f_0 = 6.8 \text{ GHz}$  and a JDPD with no geometrical asymmetries ( $J_- = 0$ ),  $L = 200 \text{ pH}$ ,  $\beta = 1.2$  for different values of  $\Phi_-$  indicated in the plots title. For  $\Phi_- = \pm\pi$  the archs related to the bistable state become the highest archs. In the range  $\Phi_- \in [-\pi, -\pi/2]$  the height difference between the archs gets closer and closer to zero, which is reached for  $\Phi_- = -\pi/2$ . Then for  $\Phi_- \in [-\pi/2, 0]$  the archs related to the bistable regime become the shortest ones, with a maximum height difference reached at  $\Phi_- = 0$ . In the positive range, for  $\Phi_- \in [0, \pi/2]$ , like in the range  $[-\pi, -\pi/2]$  the height difference gets closer and closer to zero, which is reached for  $\Phi_- = \pi/2$ . Successively, for  $\Phi_- \in [\pi/2, \pi]$  the archs related to the bistable state become again the highest ones. The circuit thus shows a periodic behaviour in terms of  $\Phi_-$ .

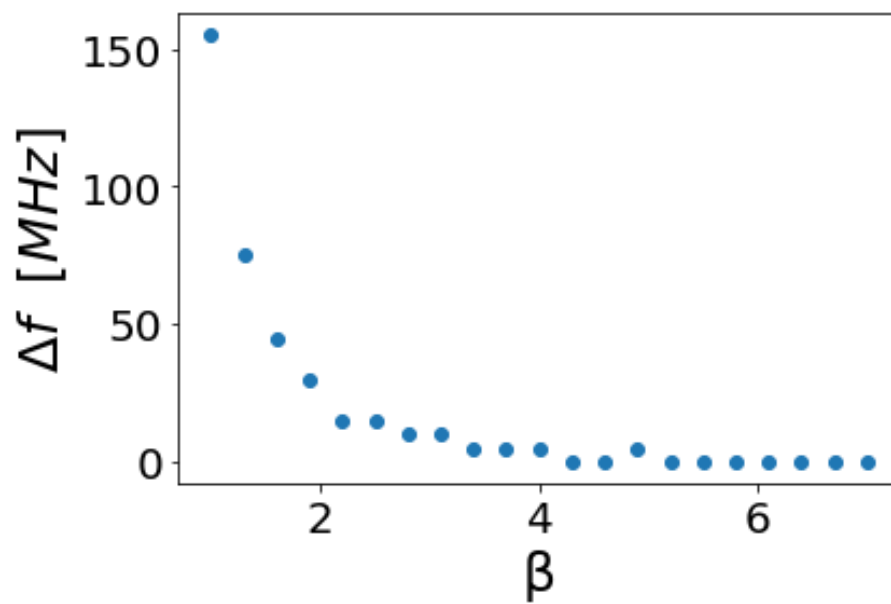


FIGURE 4.22: Expected height difference between the spectroscopy archs showed by the circuit in Fig. 3.1 with a resonator of frequency  $f_0 = 6.8 \text{ GHz}$  and a JDPD with no geometrical asymmetries ( $J_- = 0$ ),  $L = 200 \text{ pH}$  and different values of the  $\beta$  ratio.

## Chapter 5

# Experimental results

On the basis of the designs and simulations illustrated in the previous Chapter, the layout of the Josephson Digital Phase Detector (JDPD) has been sent to the company SeeQC and a first batch of devices has been fabricated in their labs in the United States. After several preliminary tests performed by SeeQC to assure the quality of the fabrication process, the samples have been sent to our lab for a comprehensive experimental characterization at  $10\text{ mK}$ . As mentioned in the previous chapters, the aim of the experimental measurements is to demonstrate if the JDPD is able, in principle, to perform the QND read-out protocol introduced in Sec. 2.2 and as specified below. To achieve this goal, different features relative to the spectroscopy circuit in Fig. 3.1 have been experimentally validated. The first one is the Josephson periodicity, namely the periodic arch-shaped trends of the circuit resonance shown in Fig. 4.17. The periodicity comes from the Josephson junctions employed in the JDPD that add the periodic term to the JDPD potential energy expression in Eq. 2.19. Regarding the JDPD read-out protocol validation the latter test is only a necessary condition towards the functioning of the read-out protocol because it does not give any hint about the number of potential energy minima. An essential step for the functioning of the read-out protocol is the ability to shape the potential of the circuit to a bistable a bistable regime that allows to distinguish the qubit state. Therefore, the second feature that has been experimentally analysed is the presence of two minima in the JDPD potential energy trend for an adequate value of  $\Phi_+$ , which represents the fundamental prerequisite to measure the phase offset of the microwave signal interacting with the resonator dispersively coupled to the qubit under test. The combination of these two tests demonstrates the JDPD capability of performing QND read-out of superconducting qubits.

In this chapter I will illustrate the main experimental steps to carry out these tests, as well as the obtained experimental results. We have measured two different circuits characterised by different properties. The first and second section of this chapter are dedicated to the experimental measurements of these devices, respectively. The same experimental measurements on different samples gives consistent results, which scale

with the JDPD properties, giving robustness to the whole approach and to the JDPD capability of performing QND read-out.

## 5.1 1<sup>st</sup> device

Chip #2, shown in Fig. 4.12, has been the first measured sample in the Triton dilution fridge, described in Sec. 3.2. The chip was located on the chip-holder in Fig. 3.4 that allows the connection to room-temperature electronics through the I/O ports. Among the different circuits and lines on the Chip #2, the following lines have been connected by using aluminium bonds:

- The central feed-line ends and the H\_7\_ circuit dedicated feed-line
- The DC lines and fast flux line of H\_7 connected to the central feed-line
- The DC lines and fast flux line of M\_5 connected to the central feed-line
- The DC lines and fast flux line of L\_3 connected to the central feed-line
- The DC lines and fast flux line of the standalone H\_7\_ circuit

The bonds to the feed-line pads allow to connect them to the VNA to perform reflectivity/transmittivity measurements and also to supply dc current to the fast flux lines. At the same time, the bonds to the DC line pads allow to supply dc current along the lateral flux lines of the JDPD. The chip-holder has been mounted to the copper L-shaped extension anchored to the mixing chamber of the Triton cryostat, as shown in Fig. 3.4, in order to cool it down to 10 *mK*. Before initiating the cool down, all the electrical connections have been checked by using the VNA and the Sourcemeter in order to test their functioning at room temperature. These preliminary measurements have shown that all the connections were fine and also that the resonances of the circuits corresponded to the expected ones.

As soon as the cryostat reached the base temperature, the first measurements were dedicated to evaluate the transmittivity and reflectivity of the circuits in the chip through the VNA of the Keysight Chassis in Fig. 3.5. These measurements have been performed to check if any problem occurred to the system by reaching this ultra-low temperature range and to test if the resonance frequencies of the various circuits were not affected in the cooling procedure. During these tests the transmittivity measurements were the ones less affected by noise. The transmittivity is evaluated from the  $S_{21}$  data acquired by the VNA by sending a microwave signal with defined power and frequency chosen to the first port connected to the fast flux

line pad of the circuit under test and evaluating the amplitude of the transmitted signal on the VNA second port connected to the feed-line pad. The data acquired in the frequency range  $[4 - 9]$  GHz and VNA attenuation of  $-20$  dBm are shown in Fig. 5.1. The outcomes show that the trends exhibit various ripples, which are an indica-

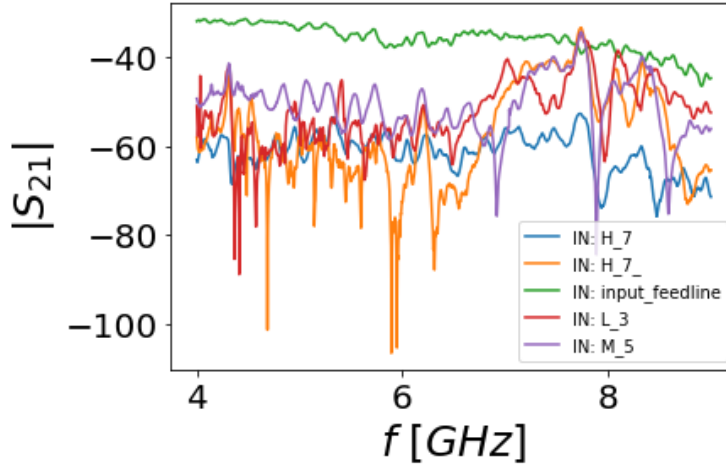


FIGURE 5.1: VNA measurements of the transmittivity with a room temperature attenuation of  $-20$  dBm. The figure portrays the amplitudes of  $S_{21}$  in the frequency range  $[4 - 9]$  GHz, namely the transmittivity of the different lines reported in the legend.

tion of impedance mismatch [34] between the signal source and the load, represented in this case by the VNA and the spectroscopy circuits, respectively. The impedance mismatch causes the bouncing back of a certain quantity of photons, leading to losses during the measurements. Impedance mismatch can be due to overlooked geometrical effects in the design or to fabrication flaws that can slightly modify the impedance of the circuit, with respect to the impedance of the VNA. In order to overcome this issue and identify the circuit resonance, the DC lines were employed. In fact, if a spike in the spectroscopy curves represents a resonance, it must move under the application of fluxes in the JDPD. These latter measurements have been prevented by a second issue, since most of the DC lines did not work properly at  $10$  mK, indicating some fabrication imperfections. By supplying a dc current to each fast flux line, in fact, the circuits spectroscopy appeared significantly disturbed, while by supplying the current to the DC lines there was no effect on it, except for one of the DC lines of the H\_7\_ circuit. As a consequence the measurements for this first run have been performed on device H\_7\_, whose layout allows to provide the fluxes  $\Phi_+$  and  $\Phi_-$  through the calibration procedure discussed in Sec. 3.5.1.

In the following sections I will illustrate the experimental results obtained from the analysis of the H\_7\_ circuit and their contribution to the validation of the JDPD read-out protocol. All the following spectroscopy measurements are performed by

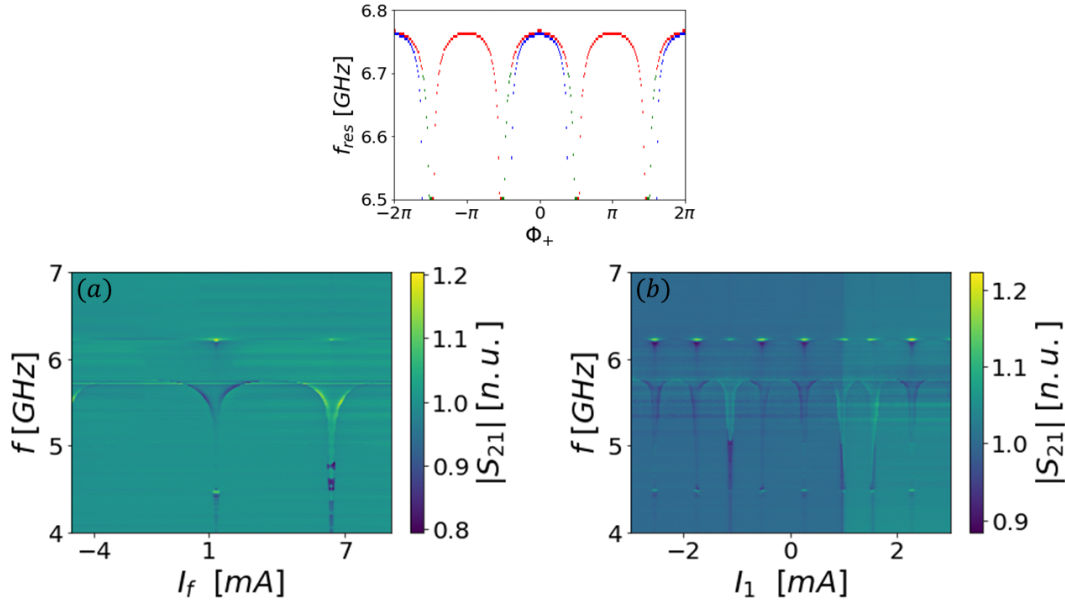


FIGURE 5.2: Plots of the transmissivity of the H\_7\_ circuit for current in the range of  $[-4, 8]$  mA across the fast flux line (a) and in the range of  $[-3, 3]$  mA for the DC line (b). The range has been chosen by taking care of the different resistance of the lines and of the possible heating effects in the cryogenic environment due to Joule heating. The upper Python plot shows what the expected evolution from the simulation.

evaluating the transmissivity of the circuit, namely  $S_{21}$ , since the measured signals are less affected by noise issues. In particular, to improve the quality of the measurements, the transmissivity data is normalized in post-acquisition by dividing all the  $S_{21}$  plot with respect to the frequency with the first acquired one.

### 5.1.1 Josephson periodicity

The first measurements on the H\_7\_ circuit were dedicated to evaluate the effect that the currents across the DC line  $I_1$  and the fast flux line  $I_f$  have on the system. Therefore, individual sweeps of  $I_1$  and  $I_f$  have been performed, and for each current value the VNA measured the correspondent transmissivity in the frequency range  $[4 - 7]$  GHz for different VNA power attenuations. The sweep on the VNA attenuation has been performed in order to find the optimal conditions in terms of visibility of the acquired signal. In Fig. 5.2 the best plots regarding the effect of  $I_1$  and  $I_f$  on the circuit spectroscopy are shown. Both plots, obtained with a  $-30$  dBm VNA attenuation, show the presence of archs in full agreement with the simulations in Sec. 4.4. These results prove the quality of the sample and that the model used for the simulations reported in Sec. 4.4 represents a good approximation of the real system, thus allowing to study the dynamics of the JDPD device from spectroscopy measurements. Comparing the results with the simulation reported in in Fig. 4.17, many relevant information can be

obtained about the circuit under study. The first feature is that the circuit characteristic resonance, represented by the height of the archs, has dropped to about  $5.75 \text{ GHz}$ , instead of the expected  $6.8 \text{ GHz}$ . This difference between the experimental resonance and the simulated one comes from having neglected the effect of superconductivity on the system spectroscopy due to the impossibility of the employed software program (QUCS, HFSS) to emulate the change that the superconducting state leads to the system. Additionally, the performed spectroscopy simulation did not take into account the whole circuit structure and thus some geometrical effects may have been overlooked. These artefacts happen in the design of a completely new device and are iteratively improved by using software and programs which can better reproduce all physical aspects of the circuit under investigation. A second peculiar discrepancy with the simulations is the presence of a  $|S_{21}|$  peak at the end of each arch in the data, for frequencies higher than the archs height. This phenomenon does not arise for higher VNA attenuation and is thus caused by the VNA signal that is able to force the phase particle to go in other minima of the potential energy profile with higher concavity values. Finally, focusing on the predicted Josephson periodicity, the plots in Fig. 5.2 show that depending on which line is employed to supply the fluxes to the JDPD, the whole circuit will have a different spectroscopy behaviour for the same dc current value. In particular, the spectroscopy response derived from the  $I_1$  sweep has a much smaller periodicity compared to the one measured by sweeping  $I_f$ . This difference is caused by the various attenuation stages along the RF lines that convey the electromagnetic signal  $I_f$  across the fast flux line, with respect to the current line connected to the dc current line  $I_1$ , that passes along a series of low pass filters. Beside this technical feature, there are also geometrical differences between the two flux supply methods, that show off in the different shape of the spectroscopy curves in Fig. 5.2. The archs obtained through  $I_1$  all have a similar shape that recalls the one from the simulations in Fig. 4.17, while the ones related to  $I_f$  sweep have a different width. This is due to a different coupling between the magnetic field generated by  $I_1$  and  $I_f$  with the loops of the JDPD. Considering Eq. 3.8, the current  $I_1$  provides simultaneously the fluxes  $\Phi_+$  and  $\Phi_-$  while the current  $I_f$  supplies the flux  $\Phi_+$ . This means that the left plot in Fig. 5.2 is the one that shows how the system behaves under different  $\Phi_+$  values as desired. Regarding the width difference between the archs in Fig. 5.2(a), according to the simulations in Fig. 4.19 it must be an effect brought by  $\Phi_-$ , that can come from unwanted trapped flux across one of the loops. This is a common artefact happening in superconducting circuits, that can disturb the dynamics of the system and thus the experimental measurements [25].

Once that the flux  $\Phi_+$  is correctly supplied through the fast flux line an explicit relation between the voltage  $V_+$ , supplied by the Sourcemeeter to the fast flux line, and

the flux  $\Phi_+$  provided to the JDPD inside the H\_7\_ circuit has been obtained. Despite the presence of a flux  $\Phi_-$ , the comparison between the simulations and the experimental trend in Fig. 5.2(a) allows to evaluate a correspondence between  $\Phi_+$  and  $V_+$ , defined by the following relation:

$$V_+ = \Phi_+ \frac{\Delta V}{2\pi} + V_{off} \quad (5.1)$$

where  $\Delta V$  is the Josephson period in units of Volt and  $V_{off}$  is the offset in the experimental trend in units of Volt. The  $V_+$  obtained by using Eq. 5.1 just work as initial guess that must be demonstrated through further checks capable of show off the regime in which the system is.

A sweep larger than the one in Fig. 5.2(a) has been applied in order to define the value  $\Delta V$  and  $V_{off}$  required by Eq. 5.1. The results of this measurement are shown in Fig. 5.3, where despite the losses that decrease the quality of the measurements, it is possible to observe that the system has a periodic behaviour in terms of  $V_+$ , and that the flux  $\Phi_+$  is supplied correctly through the fast flux line. Given the high  $\beta = 2E_J/E_L$  ratio of the JDPD in the circuit under study, each arch posses the same height of the others, as predicted by the simulations reported in Fig. 4.17. This feature makes the archs related to the different JDPD regime difficult to distinguish. Therefore, to define the value of  $V_{off}$ , it is necessary to make an initial guess about which archs are related to the regime with one absolute minimum and the regime with two absolute minima. The chosen guess is shown in the right plot of Fig. 5.3, where the dark blue and the orange dashed archs indicate the presumed zero and bistable regime archs, respectively. According to this choice, the offset is equal to  $V_{off} = -24.3 \text{ mV}$ , while the period, which can be extracted regardless of the mentioned assumption, is equal to  $\Delta V = 129.4 \text{ mV}$ . Inserting the extracted values into Eq. 5.1 allows to define an estimate of the  $V_+$  that the Sourcemeter must supply in order to provide a certain flux  $\Phi_+$  to the JDPD. The correctness of this evaluation is demonstrated in the following section, that focuses on the experimental steps performed to prove that, for an adequate combination of flux, the JDPD has the properties expected in the bistable regime.

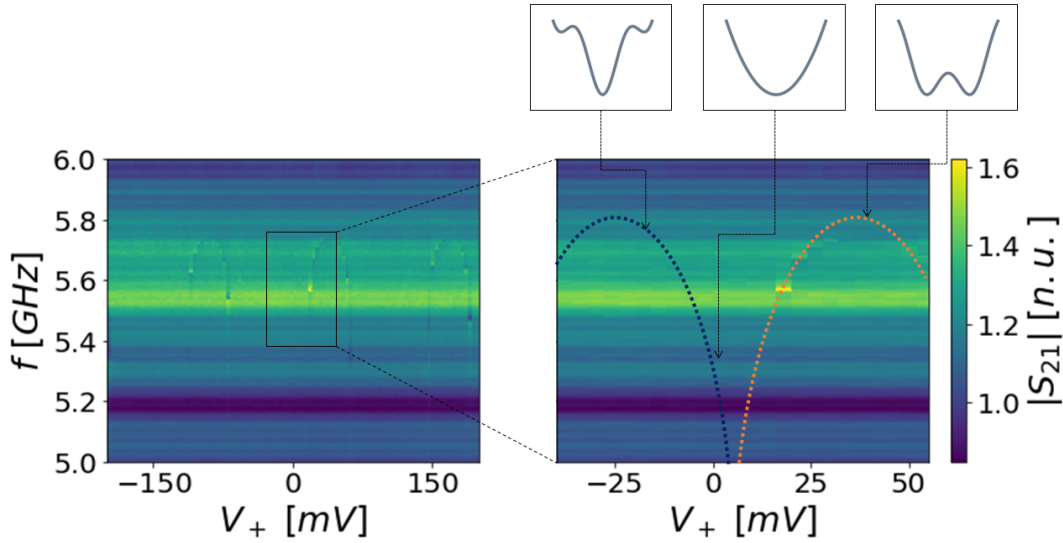


FIGURE 5.3: Results acquired from the VNA for different sweeps on the fast flux line voltage  $V_+$ . The graphs display the  $S_{21}$  pattern, namely the transmittivity of the system with respect to signals with frequencies in the range  $[5.0, 6.0]$  GHz for different values of  $V_+$  in the range  $[-200, 200]$  mV (Left) and  $[-40, 50]$  mV (Right). The voltage range in the left graph has been chosen in order to cover the widest possible region without heating the chip and thus the mixing chamber of the cryostat, while the right figure is a software zoom to focus on a small region around  $V_+ = 0$ . The dashed lines in the right graph represent the assumption about the alleged position of the JDPD spectroscopy archs in the  $V_+$  domain. The blue curve corresponds to the presumed unperturbed-harmonic state curve, while the orange one to the bistable regime arch.

### 5.1.2 Phase particle trapping

We now need to check whether the assumption of Fig. 5.3 about the position of the spectroscopy archs in the acquired data, it is now required to check this hypothesis. In order to test the JDPD capability of performing the read-out protocol, we have studied whether the JDPD enters a bistable regime by supplying an adequate voltage  $V_+$  to the fast flux line.

In the theoretical read-out protocol described in Sec. 2.2, the bistable behaviour of the JDPD shows up as a superconducting current across the central inductance of the JDPD, whose direction depends on the particular well in which the phase particle has fallen. With the available experimental setup, though, there is no way of measuring the superconducting current that passes along the central inductance. Consequently it is necessary to find a way to observe the bistable regime by using the spectroscopy measurement allowed by the VNA. As mentioned before, the main obstacle is the fact

that for JDPD with a high  $\beta$  ratio, the resonance frequency archs related to the JDPD regimes are indistinguishable from one another. This phenomenon is a consequence of the fact that the concavity of the JDPD potential energy profile in correspondence of its minima is the same in both regimes, leading to the same equivalent inductance in the circuit.

To overcome this experimental hurdle, a specific experimental protocol has been employed. The protocol takes inspiration from the hysteresis measurement performed in the work [14], and exploits both  $\Phi_+$ ,  $\Phi_-$  to adequately manipulate the JDPD potential energy. The protocol is based on the comparison between the experimental outcome of the two experimental procedures portrayed in Fig. 5.4. Assuming that the JDPD potential energy is defined by Eq. 2.19, the initial steps of the first (second) procedure, depicted in Fig. 5.4(a-e), force the phase particle to be in the deepest minimum on the left (right) of the potential energy trend in the tilted bistable regime, achieved by supplying the fluxes  $\Phi_+ = \pi; \Phi_- = -\pi/2$  ( $\Phi_+ = \pi; \Phi_- = \pi/2$ ). The deepest minimum is also the one characterised by the highest concavity, which is the measurable quantity in the experimental setup, thanks to Eq. 3.1, 3.3 that define a link with the circuit resonance frequency. At this point, by progressively increasing (lowering) the flux  $\Phi_-$ , the initial tilt slowly diminishes, providing a gradual decrease of the concavity related to the minimum where the phase particle is trapped, as portrayed in Fig. 5.4(f), which ultimately leads to a lowering of the resonance frequency. In conclusion, if the JDPD potential energy is in the bistable regime, predicted by Eq. 2.19 and thus allows to emulate the procedures just introduced, then by forcing the phase particle in two different initial conditions depicted in Fig. 5.4, the resonance frequency is lowered by sweeping  $\Phi_-$  in two opposite directions depending on the fixed initial condition. In a few words, depending on  $\Phi_-$  history, the system behaves differently, showing a hysteretic behaviour that is a direct consequence of the JDPD bistable behaviour.

The first step towards the experimental implementation of the hysteresis protocol is to find a way to simultaneously provide the fluxes  $\Phi_+$  and  $\Phi_-$  to the JDPD. In Eq. 3.8 it is shown that the DC line can be exploited together with the fast flux line to achieve this goal. Therefore, before applying the hysteresis protocol a further calibration of the fluxes provided by the simultaneous action of the DC line and the fast flux line has been done. According to the simulations reported in Fig. 4.19, in the case of JDPD with large  $\beta$  ratio, the effect of  $\Phi_-$  on the archs that characterise the transmittivity map of the circuit, is to slightly squeeze or enlarge their width. These preliminary measurements thus focused on analysing how the archs are shifted for different values of  $\Phi_-$  for a definite range of  $\Phi_+$  values. In Fig. 5.5 the data acquired by the VNA in well defined ranges of frequencies and  $V_+$  values are shown, for

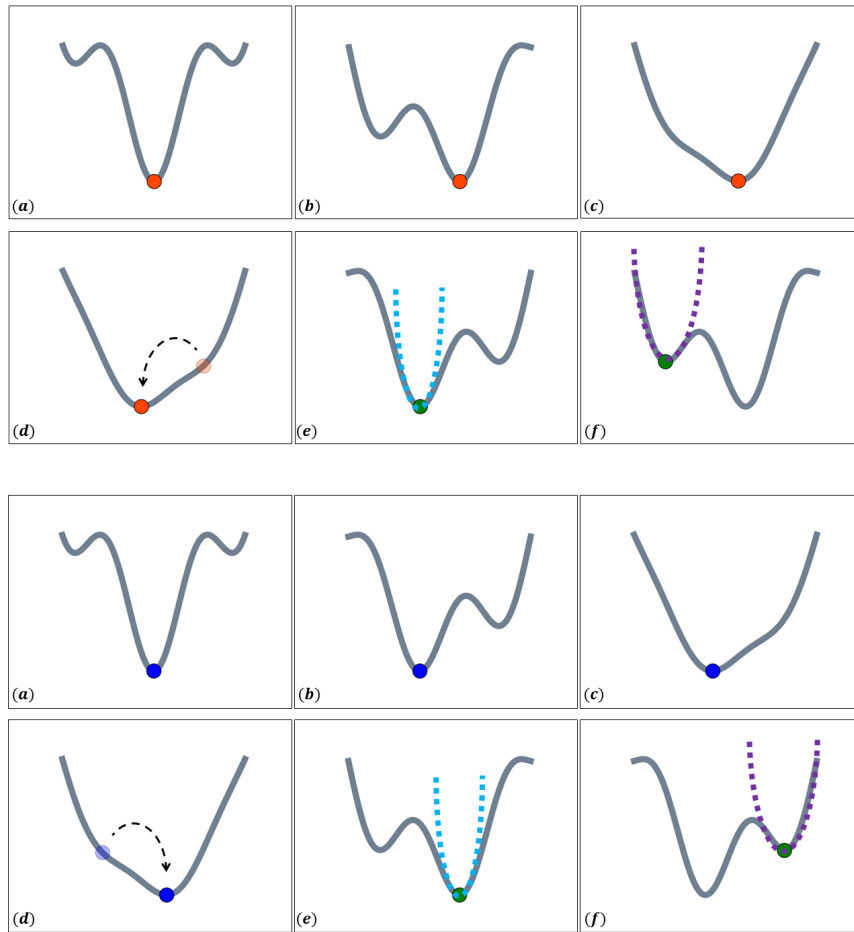


FIGURE 5.4: JDPD potential energy profile in the different steps of the first procedure (second protocol). (a)  $\Phi_+ = 0; \Phi_- = 0$ , the JDPD is in its unperturbed state. (b)  $\Phi_+ = 0; \Phi_- = -\pi/2$  ( $\Phi_+ = 0; \Phi_- = \pi/2$ ), the fluxes lead to a potential energy trend with an absolute minimum in order to set the state of the JDPD. (c-e)  $\Phi_+ = \pi; \Phi_- = -\pi/2$  ( $\Phi_+ = \pi; \Phi_- = \pi/2$ ), in the transition from  $\Phi_+ = \pi/2 - \varepsilon$  to  $\Phi_+ = \pi/2 + \varepsilon$  (c,d), where  $\varepsilon$  is a generic small value, the phase particle switches from one side to the other with respect to the origin and finally falls into the absolute minimum of the potential energy at  $\Phi_+ = \pi$  (e). The latter step is performed to guarantee that the phase particle is positioned in a predicted well, avoiding undesired trapping in non absolute minimum that could have happened during the first two steps. (f)  $\Phi_+ = \pi; \Phi_- = \pi/2$  ( $\Phi_+ = \pi; \Phi_- = -\pi/2$ ), the potential energy well containing the phase particle is tilted by the sign change of  $\Phi_-$  which brings the well higher in energy and simultaneously decrease the concavity, as shown by the dashed curves. The green phase particle indicate when the circuit is analysed through the VNA.

different values of the voltage  $V_-$  between the ends of the DC line. The results show that for different  $V_-$  the archs shift as a function of the current across the DC line, confirming that the flux  $\Phi_-$  is properly supplied to the JDPD in this way. According to Eq. 3.8 the current across the DC line supplies also a certain amount of  $\Phi_+$ . This means that if currents flow simultaneously through both lines, the flux  $\Phi_+$  depends on both lines, in disagreement with Eq. 5.1. Nevertheless, in the JDPD layout the DC line is much more coupled to the nearest loop of the circuit rather than the more distant one. This means that in the employed range of current the contribution of the fast flux line to  $\Phi_+$  is much more significant than the one coming from the DC line and, thus that the latter can be neglected in a good approximation. It is thus possible to simultaneously supply  $\Phi_+$  through the fast flux line and  $\Phi_-$  through the DC line, thus providing the physical and technical tools to perform to performing the mentioned hysteresis protocol.

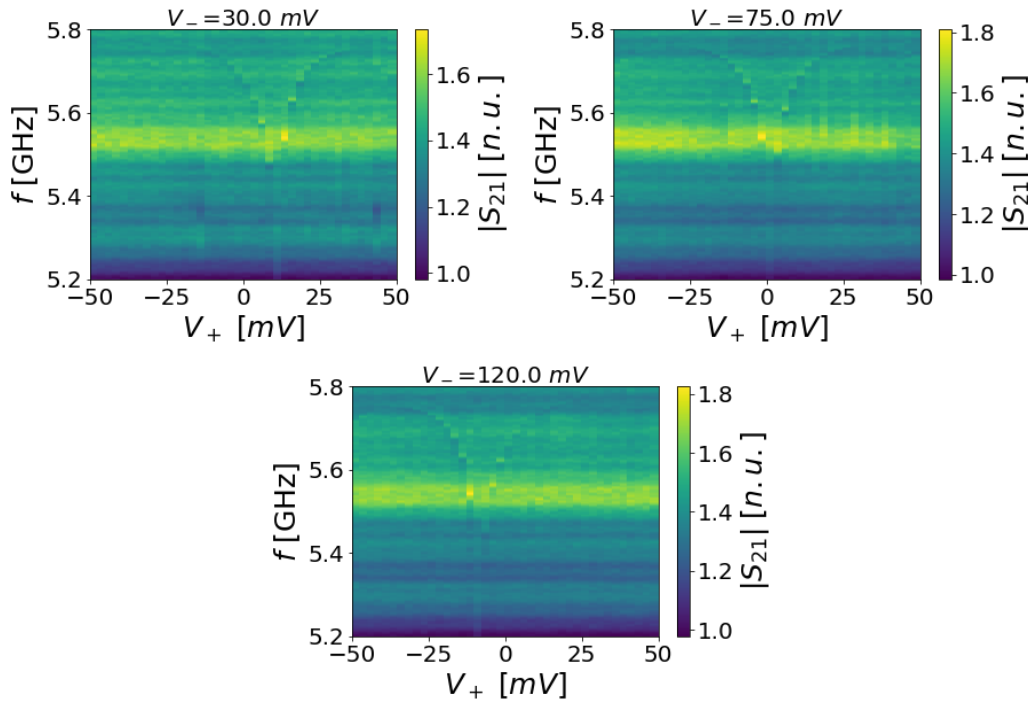


FIGURE 5.5: Transmittivity of the H\_7\_ circuit with a power attenuation of  $-50dBm$  in the range  $[-50, 50]$  mV of  $V_+$  for different values of  $V_-$  pointed out in the various plots. The results show that the archs that highlight the resonance of the circuit are shifted of a certain amount of  $V_+$  depending on the  $V_-$  provided by the Sourcemeeter.

In the last steps of the first (second) method, described in Fig. 5.4(e-f), the flux  $\Phi_-$  is shifted from  $\Phi_- = -\pi/2$  ( $\Phi_- = \pi/2$ ) to  $\Phi_- = \pi/2$  ( $\Phi_- = -\pi/2$ ), but the protocol works perfectly fine also for  $\Phi_- \neq \pm\pi/2$ , since it just leads to smaller tilts of the potential energy trend with respect to the one shown in Fig. 5.4. The protocol was thus performed by employing Eq. 5.1 to provide the appropriate value of  $\Phi_+$ ,

for different values of  $V_-$  and different VNA power attenuation in order to find the experimental settings that guarantee the best experimental execution of the hysteresis protocol. In Fig. 5.6 the data acquired by the VNA with a power attenuation of  $-50\text{ dBm}$  are shown, following the first (second) method performed by providing the flux  $\Phi_+$  according to Eq. 5.1, while setting initially  $V_- = -100\text{ mV}$  ( $V_- = 100\text{ mV}$ ) and gradually increasing (decreasing) it to  $V_- = 100\text{ mV}$  ( $V_- = -100\text{ mV}$ ). The  $V_-$  range has been chosen to explore the largest range of  $V_-$  values while avoiding the overheating of the cryostat due to the current passing across the DC line. In the first procedure test, in Fig. 5.6(a) by going from  $V_- = -100\text{ mV}$  to  $V_- = 100\text{ mV}$  the resonance profile initially decreases as expected until  $V_- = 25\text{ mV}$ , where there is a "jump" to a higher value. After the jump the resonance frequency profile inverts its slope and starts to increase as  $V_-$  increase, which is the opposite of its original behaviour. An analog evolution is observed in the experimental replica of the second procedure, in Fig. 5.6(b), where the jump is observed at  $V_- = -25\text{ mV}$  and the resonance follows an evolution similar to the one observed in Fig. 5.4(Up) but for inverted direction of the  $V_-$  sweep.

The physical explanation behind these resonance jumps, according to the potential energy trend depicted in Fig. 5.4, is that the phase particle has passed from one minimum to another in the potential energy profile. Additionally, the distance between the trends after and before the jump also shows that the final minimum is characterised by a concavity higher than the starting one. These phenomena may have different origins, such as the thermal escape or the macroscopic quantum tunneling [20] that for low enough energy separation between the minima can lead to a not negligible escape probability of the phase particle. Additionally there are also the transmitted photons coming from the VNA, that are able to excite the phase particle. Analysing the plots in Fig. 5.6, the fact that the resonance frequency of the system changes significantly indicates that the escape happens when the potential energy has an asymmetric shape with the minima characterised by different concavities. In addition to that, the fact that the jump happens always with the same amount of currents across the DC line, points out that the tilt of the potential energy trend with  $V_- = \pm 25\text{ mV}$  leads to a natural passage of the phase particle to another minimum in the potential energy trend. The slope inversion after the jump further proves that the jump is an indicator of the phase particle escape from one minimum to another in the potential energy trend. Focusing on the two minima of the potential energy trend in Fig. 5.4(e-f) it can be observed that a tilt of the potential energy trend leads to an increase of the concavity related to one minimum while decreasing the other, which is exactly what has been observed from the measurements shown in Fig. 5.6

Knowing that for  $V_- = \pm 25\text{ mV}$  the potential energy is tilted enough to induce

a phase particle jump, other protocol tests have been performed in the range of  $[-25, 25]$  mV in order to observe the hysteresis without incurring in phase particle escape from one minimum to another.

The results achieved by replicating the two methods in the mentioned range of  $V_-$  are shown in Fig. 5.7, acquired for a power attenuation of  $-60$  dBm of the VNA. The two plots show that following the  $V_-$  sweep direction indicated in the plots, the resonance frequency profile decrease as expected due to the concavity decrease of the potential energy profile shown in Fig. 5.4(e-f). In particular, the two profile, under the same excitation of  $V_-$ , exhibit two different values of the resonance frequency, demonstrating that the system has an hysteretic behaviour. The latter results prove that the JDPD is characterised by a bistable behaviour and thus that the QND read-out protocol in Sec. 2.2 can be executed.

Further replica of the latter measurements have been performed in order to check that the result is reproducible. These measurements show that the system behaves as expected under the same settings and in addition to that, it has been observed that by decreasing the VNA attenuation to  $-50$  dBm a phase particle escape similar to the one in Fig. 5.6 occurs, as shown in Fig. 5.8. Differently from the previous case, the switch of the phase particle from one minimum to another does not lead to a significant change of the circuit resonance but just to a slope inversion with respect to  $V_-$ , as shown in Fig. 5.8. The absence of a shift between the trends after and before the escape, points out that the potential energy trend is characterised by a more symmetric shape with respect to the one that it possesses in Fig. 5.6, and is consistent with the jump occurring near  $V_- = 0$ . The same phenomenon was observed in some cases with a VNA attenuation of  $-60$  dBm, proving that in this case the escape is caused by stochastic effects like the thermal escape and the macroscopic quantum tunnelling.

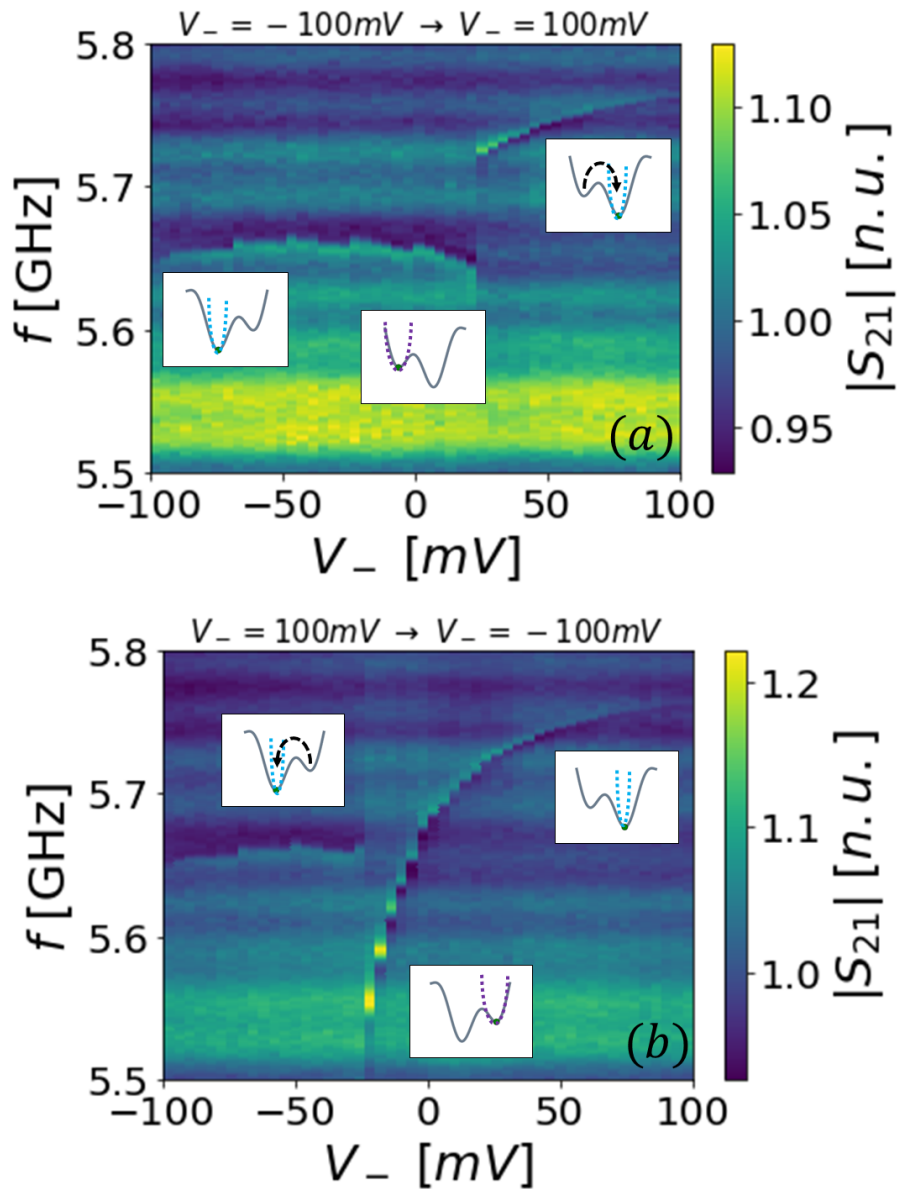


FIGURE 5.6: Transmittivity trend of the circuit from step (e) to step (f) of the first (a) and second (b) protocols reported in Fig. 5.4 with  $V_-$  spanned in the range  $[-100, 100]$  mV in the direction indicated in the plot title and for power attenuation of  $-60$  dBm. In correspondence of  $V_- = 25$  mV and  $V_- = -25$  mV there is a "jump" in the resonance trend of the first and second procedure, respectively. The jump is characterized by an inversion of the trend slope, pointing out that the phase particle has gone into another minimum of the potential energy.

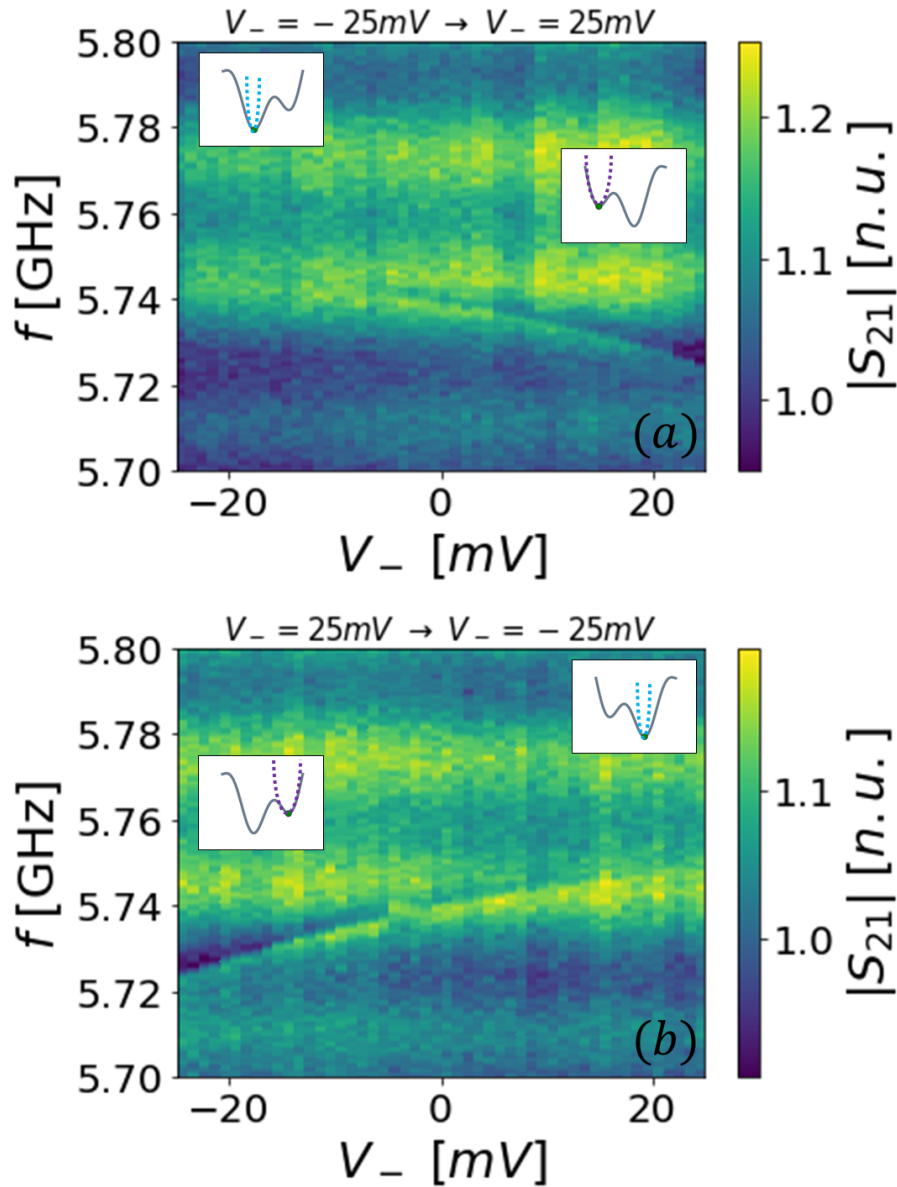


FIGURE 5.7: Transmittivity trend of the circuit from step (e) to step (f) of the first (a) and second (b) protocols reported in Fig. 5.4 with  $V_-$  spanned in the range  $[-25, 25]$  mV in the direction indicated in the plot title and for power attenuation of  $-60$  dBm. Depending on the procedure, and thus on the initial condition, the resonance frequency of the system has a different value for the same  $V_-$ , demonstrating the predicted hysteresis.

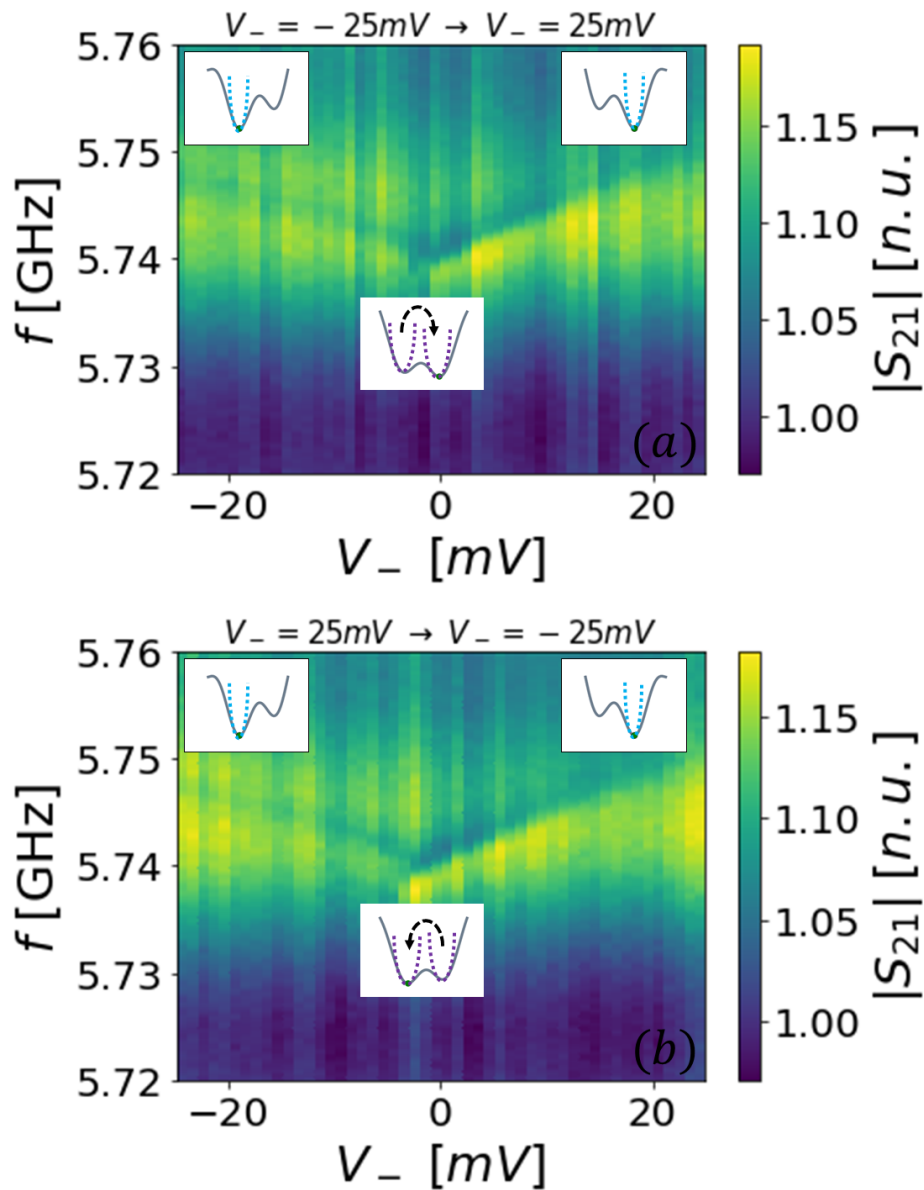


FIGURE 5.8: Transmittivity trend of the circuit from step (e) to step (f) of the first (a) and second (b) procedures depicted in Fig. 5.4 with  $V_-$  spanned in the range  $[-25, 25]$  mV in the direction indicated in the plot title and for power attenuation of  $-50$  dBm. Regardless of the initial condition, a phase particle escape is observed near  $V_- = 0$  in both cases. Differently from the escape observed in Fig. 5.6, in this case there is no frequency shift in the point of slope inversion, namely the phase particle passes to a minima in the potential energy trend which is characterised by the same concavity of the initial one.

## 5.2 2<sup>nd</sup> device

A second circuit with different properties has been analysed in order to test how its dynamics change. A different chip has been mounted on the mixing chamber of the dilution cryostat to be cooled down and analysed. The chosen sample is the Chip #1 in Fig. 4.13, that has the same circuitual arrangement of the previous one but differs from it in terms of the structural properties of the circuit. In this context it has been chosen to continue not studying the circuits coupled through the feed-line in a parallel configuration, and to focus on the JDPD inside a stand-alone circuit. In particular, the circuit that has been analysed is the H\_4 circuit in Fig. 4.13, which is characterised by a different DC lines configuration and a lower  $\beta$  ratio with respect to the previous H\_7\_.

The H\_4 circuit has been connected to the room temperature electronics to check the functioning and the spectroscopy of the circuit at room temperature. These preliminary measurements have shown similar results to the one acquired in the previous case, which further prove that the issues observed with the H\_7\_ device are not specific of the circuit but depend on the general design of the chip. Differently from the previous circuit, the use of all the DC lines has a visible effect on the circuit spectroscopy, which proves that all the lines work fine and no thermal effects disturb the connections between the chip pads and the chip-holder pads. Compared to the previous case, this result guarantees an additional degree of freedom that can be exploited to study the dynamics of the circuit. The functioning of all the lines allows to drive the fluxes  $\Phi_+$  and  $\Phi_-$  through the calibration described in Sec. 3.5.2.

### 5.2.1 Josephson periodicity

As before, the first measurements have been focused on the study of the effect of  $\Phi_+$  on the resonance frequency of the system. The main feature that differentiates the circuit H\_4 from the H\_7\_ device is that the JDPD is characterised by a lower  $\beta$  ratio. According to the simulations reported in Fig. 4.16 a lower  $\beta$ , in principle, leads to a more significant shift between the height of the archs that represent the circuit resonance frequency in the different regime of the JDPD.

To analyse the trasmissivity of the H\_4 circuit the Rohde&Schwarz VNA has been employed as well as the SourceMeters to supply currents across the DC lines and the fast flux line of the JDPD and analyse the trasmissivity for different values of the magnetic flux  $\Phi_+$ . For this measurements, I have written a Python library containing various routines able to set different features of the VNA and perform the required trasmissivity measurements. Regarding the supply of  $\Phi_+$  to the JDPD, Eq. 3.14 shows that  $\Phi_+$  can be provided both through the fast flux line and through the DC

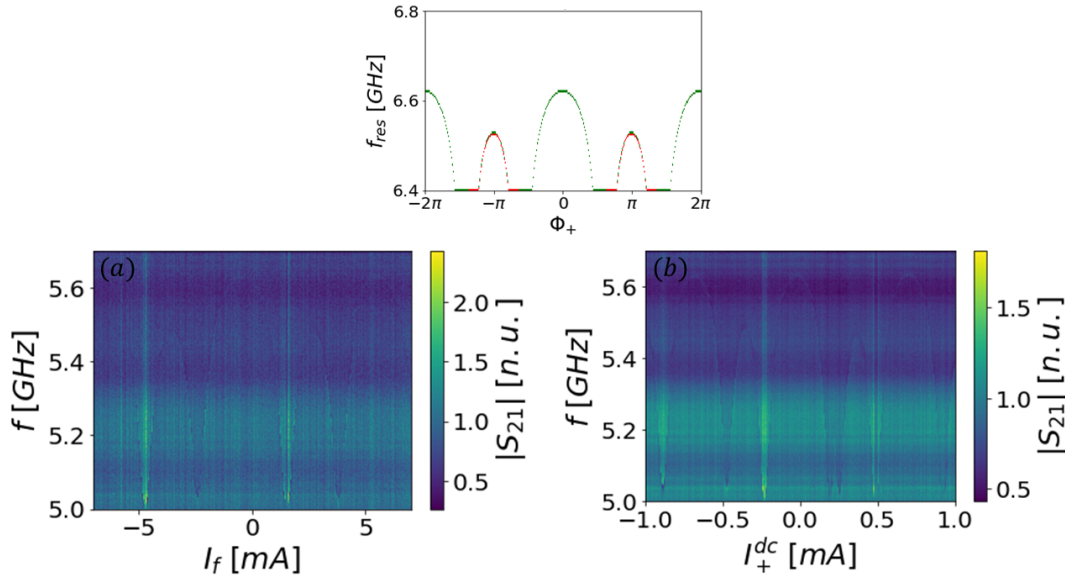


FIGURE 5.9: Plots of the H\_4 transmissivity in Chip #1 for different values of frequency and dc currents to provide  $\Phi_+$ . (a) Transmissivity of the circuit for different values of frequency and  $I_f$ , which is the current supplied to the fast flux line. (b) System spectroscopy for different values of frequency and  $I_+^{dc}$ , which is defined in terms of the current provided to the DC lines on the side as:  $I_+^{dc} = (I_1 - I_2)|_{I_1+I_2=0}$ . As previously observed, despite the current range covered with  $I_f$  is larger than the  $I_+^{dc}$  one, the two figures display the same transmissivity trend. This is a consequence of the attenuators across the RF line linked to the fast flux line, while the current lines connected to the DC lines just go through a series of low pass filters. Therefore, to have the same current across the fast flux line and the DC line it is required much more power across the RF line with respect to the current lines.

lines. In particular  $\Phi_+$  is linked both to  $I_f$ , which is the current supplied from the Sourcemeter to the fast flux line connection, and to  $I_+^{dc} = I_1 - I_2|_{I_1+I_2=0}$ , where  $I_1$  and  $I_2$  are the currents provided by the Sourcemeter to the DC line connections, respectively. Both these methods have been tested while also trying different VNA attenuation values, to check which combination of flux supply method and attenuation guarantees the better quality of the measurements outcome. The best data, displayed in Fig. 5.9, have been obtained with a power attenuation of  $-30$  dBm and  $-40$  dBm with the DC lines and the fast flux line, respectively.

First of all, we measure the same resonance frequency decrease observed before, with the same drop to  $5.75$  GHz, which is consistent with the explanation given in the previous case. A second visible feature is the presence of a periodicity in both plots as well as an height difference between the spectroscopy archs. As highlighted in Fig. 4.20, this latter feature is an indicator that the JDPD in the circuit is characterised by an extremely low  $\beta$  ratio. From the experimental data in Fig. 5.9 it was extracted an

experimental height difference of  $\Delta f = 15 \text{ MHz}$  between the archs, which compared with the simulation in Fig. 4.20 points out that the effective  $\beta$  of the system is  $\beta = 0.8$ . This unexpected decrease of the  $\beta$  ratio is linked to the JDPD layout, where the kinetic inductance of the JDPD superconducting branches, overlooked in the design simulation, lowers significantly the equivalent inductance of the system and thus the  $\beta$  ratio of the JDPD. Being the JDPD layout the source of this drastic decrease of the  $\beta$  ratio, an overestimate of the  $\beta$  ratio was probably made also for the previous circuit. In the context of the H\_7\_ circuit, though, this decrease has not been detected due to the higher critical current of the Josephson junction in the JDPD that keeps the  $\beta$  value high enough, therefore a significant height difference between the archs has not been observed.

In the context of the JDPD dynamics characterization, this feature allows to eliminate the "guess and check" step in order to distinguish the archs related to the different JDPD regimes. The only criteria that needs to be checked in this context is in fact that the flux  $\Phi_-$  provided to the JDPD due to external flux noise is not contained in the interval  $[\pi/2; \pi]$ , where the arch related to the bistable regime becomes the highest one, as shown by the simulations reporting in Fig. 4.16.

After checking that the flux  $\Phi_+$  can be controlled through the fast flux line and the DC lines, a second set of measurements has been dedicated to check if also  $\Phi_-$  can be provided to the JDPD through the relation in Eq. 3.14. In order to accomplish this check, various measurements similar to the previous ones have been performed under different  $\Phi_-$  provided to the system. Following Eq. 3.14, the fluxes  $\Phi_+$  and  $\Phi_-$  have been simultaneously provided through an adequate combination of currents across the DC lines. In particular,  $\Phi_+$  is linked to  $I_+ = I_1 - I_2$ , while  $\Phi_-$  to  $I_- = I_1 + I_2$ . Therefore, the currents actually supplied by the Sourcemeters are the solutions of the linear system with the chosen  $I_{\pm}$  as constant values. The data acquired from these measurements are displayed in Fig. 5.10 where it can be seen that for different values of  $I_-$  the height distance between the archs is different, as expected from the simulations in Fig. 4.16. The latter results thus guarantee that the flux  $\Phi_+$  and  $\Phi_-$  can be provided to the JDPD, separately or simultaneously, through the DC lines on the sides of the JDPD.

### 5.2.2 Phase particle trapping

The same protocol carried out in Sec. 5.1.2 for the first device, has been executed also on this second circuit, in order to confirm the JDPD capability, also for lower  $\beta$  ratio, of entering the bistable regime for an appropriate magnetic flux. In this case, the fluxes  $\Phi_+$  and  $\Phi_-$  have been simultaneously supplied to the JDPD through the

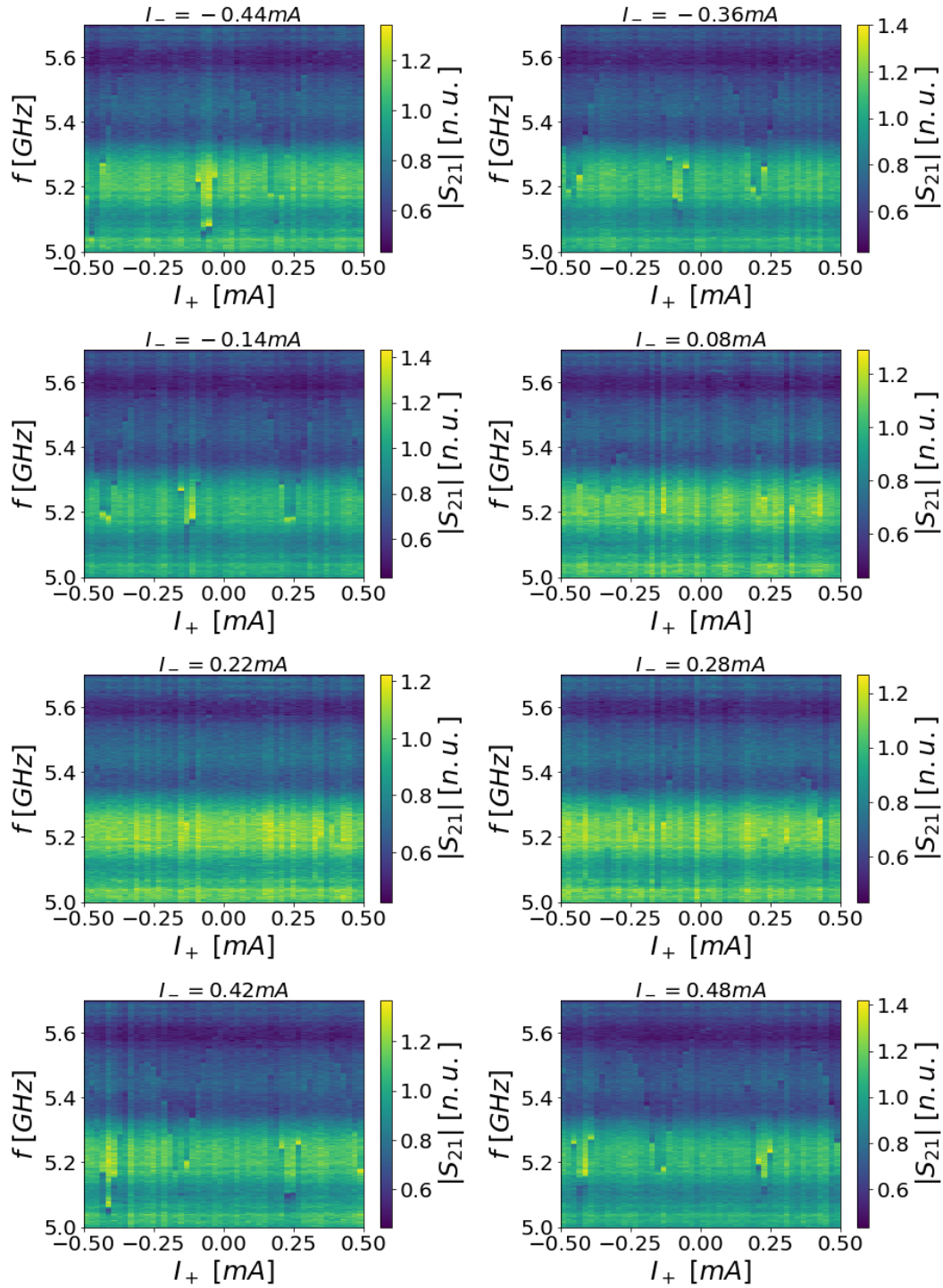


FIGURE 5.10: Plots of the transmittivity across the circuit H\_4 in respect to frequency as a function of  $I_+$  and  $I_-$  that are both defined by the DC lines on the sides of the JDPD. By going from negative to positive values of  $I_+$ , in the range  $[-0.44, -0.14] \text{ mA}$  the archs on the sides are the highest one and the height difference gradually goes to zero, which is reached for  $I_- = -0.14 \text{ mA}$ . After this range the central arch become the highest one and the height difference gradually increase until  $I_- = 0.28 \text{ mA}$ . After  $I_- = 0.28 \text{ mA}$  the side archs rise up, decreasing the height difference, that eventually goes to zero near  $I_- = 0.48 \text{ mA}$ .

DC lines on the sides by employing the same method used to perform the measurements in Fig. 5.10.

In order to choose the values of  $I_+$  and  $I_-$  required to perform the procedures reported in Fig. 5.4, the spectroscopy measurements displayed in the previous section have been compared with the simulations in Sec. 4.4, assuming that no trapped flux has modified significantly the circuit spectroscopy. In particular, to provide the required amount of  $\Phi_+$  to the JDPD, the measurements in Fig. 5.9(b), compared with the simulations in Fig. 4.20, have been taken as a reference, while for  $\Phi_-$  the measurements reported in Fig. 5.10 and the simulations of Fig. 4.20 have been used. In this way, to provide  $\Phi_+ = \pi$  the Sourcemeters must supply a current to the DC lines such that  $I_+ = 0.3 \text{ mA}$ ; while for  $\Phi_- = -\pi$  it is necessary to supply  $I_- = -0.5 \text{ mA}$ , which is the value where the spectroscopy trend returns to its original form. Starting from these considerations, multiple tests of the hysteresis protocol have been performed with different VNA power attenuation.

Differently from the previous case, no hysteresis has been observed between the two protocols in this case for any VNA power attenuation and after many tests of the magnetic fluxes provided through the DC lines. All the measurements displayed the trend shown in Fig. 5.11, where the resonance frequency of the circuit initially decreases and then rises up after a certain threshold value which is slightly different depending on the measurement protocol employed. The absence of trend difference between the plots in Fig. 5.11 shows that there is no hysteresis effect. The fact that the behaviour is similar by using both measurement protocols, can be linked to the fact that the phase particle is trapped in the same minima in both cases, and their concavity is independent from the  $\Phi_-$  sweep direction. This means that the potential energy trend of the JDPD under test is not characterised by a bistable behaviour under the provided current of  $I_+ = 0.3 \text{ mA}$ .

The cause of this result, compared with the successful results obtained with the previous circuit, can only be linked to the lower  $\beta$  ratio of the JDPD in the H\_4 circuit. Considering the plots in Fig. 4.16, it can be seen that in the bistable regime a lower  $\beta$  ratio leads to a lower energy separation between the two minima. According to the analytical model, in fact, for  $\beta < 1$  the JDPD does not show off a bistable behaviour, avoiding the possibility to perform the hysteresis protocol, as the experimental results prove. The conclusion is thus that the feasibility of the JDPD for QND read-out of superconducting qubits strongly depends on its  $\beta$  ratio that is related to the separation between the minima in the bistable regime of the JDPD.

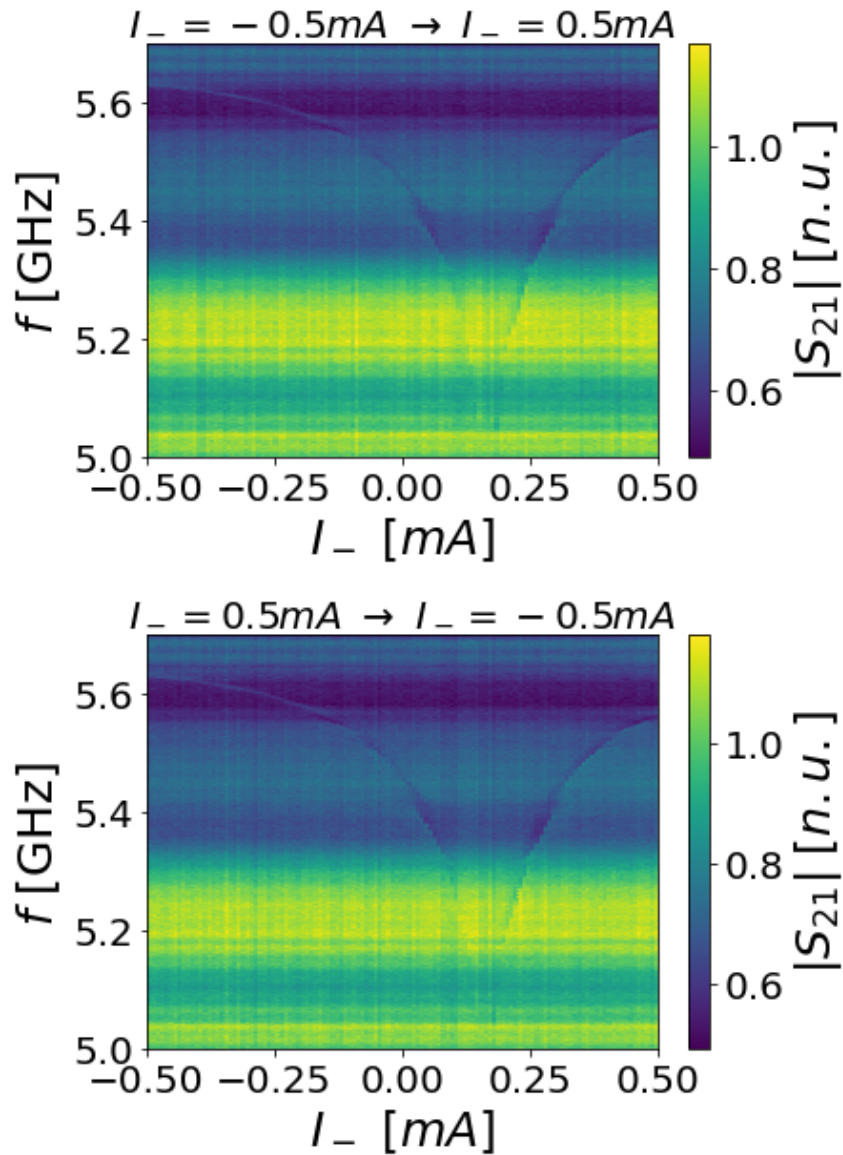


FIGURE 5.11: Transmittivity trend of the circuit from step (e) to step (f) of the first (a) and second (b) measurements protocol reported in Fig. 5.4 for a power attenuation of  $-20$  dBm with  $I_-$  spanned in the range  $[-0.5, 0.5]$  mA in the direction indicated in the plot title. No significant difference is observed between the plots except for a small shift.

# Conclusions

In this thesis I have presented the work made to study the dynamics of an innovative superconducting quantum circuit, called Josephson Digital Phase Detector (JDPD), with the aim to demonstrate that it is able to perform quantum non demolition read-out of superconducting qubits. The read-out is performed by following a specific protocol that is based on the tunability of the JDPD dynamics through external magnetic fields. This device leads to potential advantages in a quantum computer design. In addition to the non demolition read-out of the qubit state, the JDPD allows a significant scalability enhancement of quantum computer architecture thanks to its reduced dimensions, its suitability in parallel configurations and, more importantly, to the possibility to digitalize the read-out in the form of magnetic flux quanta. The latter feature in particular makes the JDPD compatible with superconducting electronics employing Rapid Single Flux Quantum (RSFQ) logic [3–6].

To demonstrate the feasibility of the JDPD as a qubit read-out device, its dynamics has been analysed with the specific aim of validating its capability of performing the non-destructive read-out protocol. I have simulated the JDPD with the PSCAN2 simulator to test if the device is able in principle to perform the read-out protocol. Then, I have characterised, through Python scripts and simulator softwares such as QUCS and HFSS, the various components of a circuit used to study the JDPD dynamics through spectroscopy measurements. This characterisation has allowed the design and the realization of various chips containing multiple JDPDs with different properties, where each of them can be analysed through the available instrumentation. Moreover, I have written some Python scripts, based on the analytical model describing the JDPD, with the aim of predicting the spectroscopy behaviour of the various circuits under different conditions. I have investigated how the circuits respond to a variation of the applied magnetic flux on the JDPD and how the response changes depending on the structural feature of the latter device. These simulations have been used to predict the behaviour of the chips and also to have some reference terms during the experimental measurements, in order to link the experimental spectroscopy measurements with the JDPD dynamics. I have then collaborated to the experimental measurements of the JDPD dynamics. The measurements are devoted to validate that the device follows the analytical model by comparing the experimental results with the simulations. Moreover, we have checked that the JDPD, for an

appropriate magnetic flux drive, enters into a bistable regime which is essential for the functioning of the read-out protocol. The outcome, that has been extracted by the acquired experimental data, is that the analytical model accurately describes the JDPD dynamics and that for the application of the latter device for qubit read-out, it must be given great attention to its structural properties. By comparing the results obtained from two JDPDs, that differ for the critical current of their Josephson junctions, it has been observed that if the product between the critical current and the equivalent inductance of the device is too low, the JDPD does not show a distinct bistable behaviour and it is thus not suitable for performing qubit read-out, as predicted by the analytical model.

In conclusions, the strong consistency between the experimental results and the analytical model confirms that the JDPD is able to execute the read-out protocol and thus of non-destructively reading the qubit state, in principle. The next natural steps towards the complete validation of the JDPD as a read-out device are an accurate analysis of its fidelity, given the sensitivity of the read-out protocol outcome to asymmetries in the system, and of the potential backaction issues that the device can give. After optimizing the device by minimizing the backaction and maximising the fidelity, the next step will be to test the read-out with an actual superconducting qubit. If the test returns positive results the further steps will be to optimize the implementation of the JDPD into a quantum computer based on RSFQ logic. The realization and the successful operation of the JDPD are not only a remarkable quantum technical achievement, but condense the quantum capabilities of superconducting circuits and Josephson junctions. It is a superb demonstration of how their functionality can be engineered and tuned to reveal and communicate quantum information.

# Appendix

## IQ mixing

An IQ mixer is essentially a 4 port device that takes in input two signals with the same intermediate frequency and opposite amplitude:

$$I(t) = a(t)\cos(\omega_{IF}t)$$

$$Q(t) = -a(t)\sin(\omega_{IF}t)$$

The  $I(t)$  and  $Q(t)$  signals are called respectively the "In phase" and "Quadrature" components of a signal with  $\omega_{IF}$  frequency, and represent the real and imaginary part of the latter in the complex plane. Along with these two, a third signal with unitary amplitude called "local oscillator" or "carrier signal" is added to the mixer:

$$L(t) = \cos(\omega_{LO}t)$$

This last signal is split in two signals that share a phase difference of  $\frac{\pi}{2}$  through an Hybrid Coupler. Consequently these two signals are then respectively coupled with the  $I$  and  $Q$  component and added together, obtaining the following output signal:

$$RF(t) = a(t)\cos(\omega_{IF}t)\cos(\omega_{LO}t) - a(t)\sin(\omega_{IF}t)\sin(\omega_{LO}t) = a(t)\cos[(\omega_{IF} + \omega_{LO})t]$$

Therefore to obtain an input signal of a certain frequency  $\omega_d$  it is possible to feed to the IQ mixer two signal with frequencies  $\omega_{IF}$  and  $\omega_{LO}$ , such that  $\omega_d = \omega_{IF} + \omega_{LO}$ . Using the same logic it's possible to carry out a down conversion too. If the I and Q port of a second IQ mixer are probed to the output of the previous mixer, using the same local oscillator it is possible to effectively down convert the output signal and make it readable for standard electronic devices.

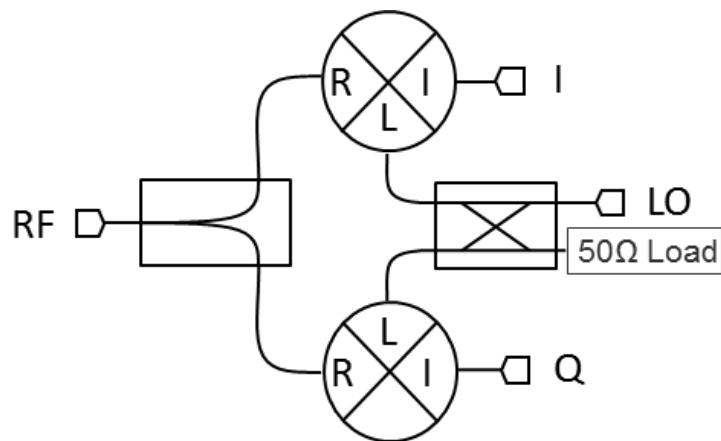


FIGURE 5.12: Block diagram of an IQ mixer. The right ports indicate the four input necessary to perform the IQ mixing. The I and Q port are related to the "In phase" and "Quadrature" component of the input signal, respectively, the LO port is the "Local Oscillator" and the  $50\ \Omega$  load port is an idle port of the system. The left port is the RF output of the mixer, where the radio frequency signal up-converted or down-converted is sent to the rest of the circuit.

## Josephson Digital Phase Detector: Potential energy

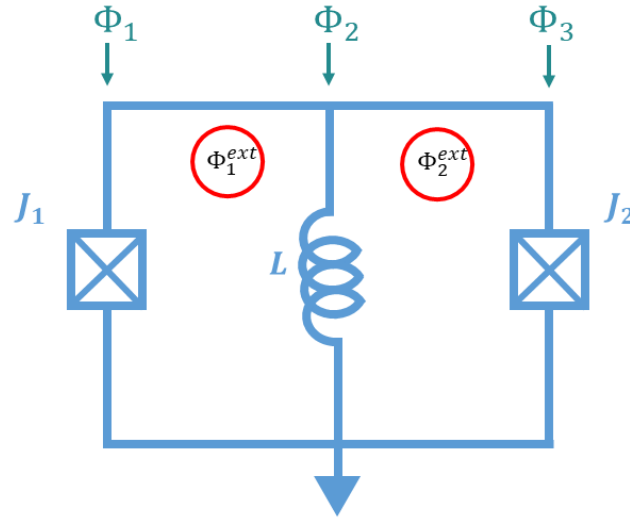


FIGURE 5.13: Schematic representation of the Josephson Digital Phase Detector. The flux convention adopted in this section is indicated in the figure.

To define the potential energy of the Josephson Digital Phase Detector (JDPD), let's consider its circuitual representation in Fig. 5.13. Following the Lagrangian treatment of electromagnetic circuits in Sec. 1.1, the system can be described by assigning a flux to each branch of the circuits, following the convention portrayed in Fig. 5.13. The fluxes will be the position-like degree of freedom of the circuit, whose Lagrangian is defined by the underlying expression:

$$\mathcal{L} = E_{J1} \cos\left(2\pi \frac{\Phi_1}{\Phi_0}\right) - \frac{\Phi_2^2}{2L} + E_{J2} \cos\left(2\pi \frac{\Phi_3}{\Phi_0}\right) \quad (5.2)$$

Considering the fluxes  $\Phi_1^{ext}$  and  $\Phi_2^{ext}$  provided by the external current lines to the JDPD loops, the fluxes  $\Phi_1, \Phi_2, \Phi_3$  across the branches have to respect the following condition:

$$\Phi_1 - \Phi_2 = \Phi_1^{ext} \quad (5.3)$$

$$\Phi_2 - \Phi_3 = \Phi_2^{ext}$$

The latter conditions leads to relations between the phases across the superconducting branches of the circuit. By applying the flux-phase relation in Eq. 1.17, the expressions in Eq. 5.3 can be rewritten in the following way:

$$\left(\frac{\Phi_0}{2\pi}\right) \varphi_1 - \left(\frac{\Phi_0}{2\pi}\right) \varphi_2 = \Phi_1^{ext} \rightarrow \varphi_1 - \varphi_2 = \left(\frac{2\pi}{\Phi_0}\right) \Phi_1^{ext} \quad (5.4)$$

$$\left(\frac{\Phi_0}{2\pi}\right)\varphi_2 - \left(\frac{\Phi_0}{2\pi}\right)\varphi_3 = \Phi_2^{ext} \rightarrow \varphi_2 - \varphi_3 = \left(\frac{2\pi}{\Phi_0}\right)\Phi_2^{ext}$$

To take advantage of the latter relations, let's rewrite the Lagrangian in Eq. 5.2 in terms of the phases:

$$\mathcal{L} = E_{J1}\cos(\varphi_1) - \left(\frac{\Phi_0}{2\pi}\right)^2 \frac{\varphi_2^2}{2L} + E_{J2}\cos(\varphi_3) \quad (5.5)$$

The two conditions in Eq. 5.4 allow to rewrite the Lagrangian of the whole circuit in terms of only one variable. Therefore, the Lagrangian of the JDPD becomes a one variable function that depends parametrically on the external fluxes  $\Phi_1^{ext}$  and  $\Phi_2^{ext}$ . Taking the phase across the central linear inductor as the dynamical variable of the system, and denoting  $\Phi_1^{ext} = \Phi_1$ ,  $\Phi_2^{ext} = \Phi_2$ ,  $\varphi_2 = \varphi$ ,  $E_L = \left(\frac{\Phi_0}{2\pi}\right)^2 \frac{1}{L}$ , the Lagrangian of the JDPD can be rewritten as follow:

$$\mathcal{L} = E_{J1}\cos\left(\varphi + \left(\frac{\Phi_0}{2\pi}\right)\Phi_1\right) - E_L \frac{\varphi^2}{2L} + E_{J2}\cos\left(\varphi - \left(\frac{\Phi_0}{2\pi}\right)\Phi_2\right) \quad (5.6)$$

Applying the trigonometric addition and subtraction rules the Lagrangian can be rewritten:

$$\begin{aligned} \mathcal{L} = E_{J1} & \left[ \cos\varphi \cos\left(\frac{2\pi}{\Phi_0}\Phi_1\right) - \sin\varphi \sin\left(\frac{2\pi}{\Phi_0}\Phi_1\right) \right] - E_L \frac{\varphi^2}{2L} + \\ & + E_{J2} \left[ \cos\varphi \cos\left(\frac{2\pi}{\Phi_0}\Phi_2\right) + \sin\varphi \sin\left(\frac{2\pi}{\Phi_0}\Phi_2\right) \right] \end{aligned} \quad (5.7)$$

To extract a more compact expression of the JDPD Lagrangian it is convenient to introduce the following flux quantity:

$$\Phi_{\pm} = \frac{\pi}{\Phi_0} (\Phi_1 \pm \Phi_2) \quad (5.8)$$

By replacing the single fluxes  $\Phi_1$  and  $\Phi_2$  with the sum and difference fluxes  $\Phi_+$  and  $\Phi_-$ , the Lagrangian in Eq. 5.7 is rewritten by the underlying expression:

$$\begin{aligned} \mathcal{L} = & E_{J1} [\cos\varphi\cos(\Phi_+ + \Phi_-) - \sin\varphi\sin(\Phi_+ - \Phi_-)] - E_L \frac{\varphi^2}{2L} + \\ & + E_{J2} [\cos\varphi\cos(\Phi_+ + \Phi_-) - \sin\varphi\sin(\Phi_+ + \Phi_-)] \end{aligned} \quad (5.9)$$

Applying the trigonometric addition and subtraction rules twice, we get to the underlying definition of the Lagrangian:

$$\begin{aligned} \mathcal{L} = & E_{J1} [\cos\Phi_+\cos(\varphi + \Phi_-) - \sin\Phi_+\sin(\varphi + \Phi_-)] - E_L \frac{\varphi^2}{2L} + \\ & + E_{J2} [\cos\Phi_+\cos(\varphi + \Phi_-) + \sin\Phi_+\sin(\varphi + \Phi_-)] \end{aligned} \quad (5.10)$$

The Lagrangian of the JDPD is made up of terms that depends only on the phase across the central linear inductor, which is the position-like degree of freedom of the system. This means that the Lagrangian of the system is equal to the opposite of its potential energy. By introducing  $E_{J\pm} = E_{J1} \pm E_{J2}$  we get to the final definition of the potential energy of the JDPD in Eq. 2.19:

$$U(\varphi) = \frac{E_L\varphi^2}{2} - E_{J+}\cos(\Phi_+)\cos(\varphi + \Phi_-) - E_{J-}\sin(\Phi_+)\sin(\varphi - \Phi_-) \quad (5.11)$$

## Python programs

In this appendix I have reported the Python codes used to study the JDPD dynamics.

### JDPD potential energy

This script allows to portray how the tuning of  $\Phi_+$ ,  $\Phi_-$  and  $\beta$  affects the JDPD potential energy profile.

---

```

"""
@author: Pasquale Mastrovito
"""

import numpy as np
from matplotlib import pyplot as plt
from matplotlib.widgets import Slider

phi_0 = 2.0*1e-15
L = 200e-12
E_l = phi_0**2 / (4.0 * np.pi**2 * L)
beta = 7
betap = beta*2
betam = 0
Icp = np.pi*E_l*betap/phi_0
Icm = np.pi*E_l*betam/phi_0
Ic_1 = (Icp + Icm)*0.5
Ic_2 = (Icp - Icm)*0.5
Ejp = phi_0 * Icp / (2.0 * np.pi)
Ejm = phi_0 * Icm / (2.0 * np.pi)
p = np.linspace(-2.0*np.pi, 2.0*np.pi, 1001)
k = phi_0/(np.pi*E_l)
phi_p = 0
phi_m = 0
u = ((p**2) - k*(Icp*np.cos(phi_p)*
            np.cos(p+phi_m) +
            Icm * np.sin( p + phi_m)*
            np.sin(phi_p)))

fig, ax = plt.subplots()
plt.subplots_adjust(left=0.25,
```

```

        bottom=0.25)
l, = plt.plot(p, u, lw=2)
plt.ylim(-30,40)
plt.axis('off')
ax.margins(x=0)
axcolor = 'lightgoldenrodyellow'
axfluxp = plt.axes([0.25, 0.15,
                    0.07, 0.03], facecolor=axcolor)
axfluxm = plt.axes([0.55, 0.15,
                    0.07, 0.03], facecolor=axcolor)
axbeta = plt.axes([0.85, 0.15,
                   0.07, 0.03], facecolor=axcolor)

#Slider range of phi_+, phi_-, beta
sfluxp = Slider(axfluxp, '$\Phi_+$', 0.0, 2*np.pi,
                valinit=0, valstep=np.pi/31)
sfluxm = Slider(axfluxm, '$\Phi_-$', -2*np.pi, 2*np.pi,
                valinit=0, valstep=np.pi/31)
senp = Slider(axbeta, r'$\beta$', 2, 10,
              valinit=0, valstep=1)

def update(val):
    phi_p = sfluxp.val
    phi_m = sfluxm.val
    beta = senp.val
    Icm = 0
    betap = beta*2
    E1 = phi_0**2 / (4.0 * np.pi**2 * L)
    Icp = np.pi*E1*betap/phi_0

    k = phi_0/(np.pi*E_1)

    pot = (p**2) - k*(Icp*np.cos(phi_p)*
                    np.cos(p+phi_m) +
                    Icm * np.sin( p + phi_m)*
                    np.sin(phi_p))

    l.set_ydata(pot)
    fig.canvas.draw_idle()

```

```
sfluxp.on_changed(update)
sfluxm.on_changed(update)
senp.on_changed(update)
plt.show()
```

---

## Spectroscopy circuit simulation

This script shows the expected resonance frequencies of the spectroscopy circuit for different values of  $\Phi_+$  applied to the JDPD. The  $\beta$  ratio of the JDPD and the flux  $\Phi_-$  applied to it can be set by the user.

---

```
"""
@author: Pasquale Mastrovito
"""

import numpy as np
from matplotlib import pyplot as plt
import matplotlib.colors as colors
from scipy.signal import find_peaks
plt.close('all')

# Constants
phi_0 = 2.0*1e-15
L = 200*1e-12
E_l = phi_0**2 / (4.0 * np.pi**2 * L)

def u(p, icp, icm, pp, pm):
    pot = 0.5*(p**2)*E_l - phi_0*(icp*np.cos(p + pm)*np.cos(pp)
        + icm*np.sin(pp)*np.sin(p+pm))/np.pi

    return pot

def duddp(p, icp, icm, pp, pm):
    pot2 = E_l + (phi_0*(icp*np.cos(p + pm)*np.cos(pp)
        - icm*np.sin(pp)*np.sin(p+pm)))/np.pi

    return pot2

# Resonator
f_0 = 6.8e9
```

```

C_r = 1/(2*np.pi*50*f_0)
L_r = 50*50*C_r

#Beta ratio
beta = 7
betap = beta*2
betam = 0

#Critical current for fixed beta and L
icp = np.pi*E_l*betap/phi_0
icm = np.pi*E_l*betam/phi_0
Ic_1 = (icp+icm)*0.5
Ic_2 = (icp-icm)*0.5

#Fluxes and phase values
n = 500
p = np.linspace(-2*np.pi, 2*np.pi, n)
pp_values = np.linspace(-np.pi, np.pi, n)
pm = 0
f_res = []

for i,pp in enumerate(pp_values):

    U = u(p,icp,icm,pp,pm)
    min_ind, _ = find_peaks(-U, distance=1)
    min_p = p[min_ind]
    min_u = u(min_p,icp,icm,pp,pm)
    f_0_ar = []

    for p_min in min_p:
        L = pow(phi_0/(2*np.pi),2)/(duddp(p_min,icp,icm,pp,pm))
        f_0 = 1/(2*np.pi*pow((L_r + L)*C_r,1/2))*1e-9
        f_0_ar.append(f_0)

    f_res.append(np.array(f_0_ar))
nf = 201 #Grid thickness
f_sort = [np.sort(item) for item in f_res]
f_values = np.linspace(6.4,6.8,nf)

```

```

f_graph = np.zeros((pp_values.size,f_values.size))

for o,item in enumerate(f_res):
    for y,elem in enumerate(item):
        index = np.where(f_values > elem)[0][0]
        f_graph[o,index] = y+1

pp_mesh,f_mesh = np.meshgrid(pp_values,f_values)

plt.figure(1)
plt.xlabel(r"\Phi_{+}",size=15)
plt.ylabel("$f_{res}$"+" $[GHz]$",size=15)
plt.title(r'\Phi_{-}$= ' + str(round(pm,2)) + ' r\beta=$'
          + str(beta))
cmap = colors.ListedColormap(['white', 'green', 'red', 'blue'])
boundaries = [0, 1, 2, 3, 4]
norm = colors.BoundaryNorm(boundaries, cmap.N, clip=True)
plt.pcolormesh(pp_mesh, f_mesh, np.transpose(f_graph), cmap=cmap
              , norm=norm)
tick_pos = np.linspace(-np.pi,np.pi,5)
labels = ['$-\pi$', '$-\pi/2$', '$0$', '$\pi/2$', '$\pi$']
plt.xticks(tick_pos,labels)
plt.show()

```

---

## Height difference of the spectroscopy archs

This script evaluates the difference between the resonance frequency of the spectroscopy circuit for  $\Phi_+ = 0$  and  $\Phi_+ = \pi$  applied to the JDPD.

---

```
"""
```

```
@author: Pasquale Mastrovito
```

```
"""
```

```

import numpy as np
from matplotlib import pyplot as plt
import matplotlib.colors as colors
from scipy.signal import find_peaks
plt.close('all')

```

```

# Constants
phi_0 = 2.0*1e-15
L = 200*1e-12
E_l = phi_0**2 / (4.0 * np.pi**2 * L)

def u(p, icp, icm, pp, pm):
    pot = 0.5*(p**2)*E_l - phi_0*(icp*np.cos(p + pm)*np.cos(pp)
        + icm*np.sin(pp)*np.sin(p+pm))/(np.pi)
    return pot

def duddp(p, icp, icm, pp, pm):
    pot2 = 1*E_l + (phi_0*(icp*np.cos(p + pm)*np.cos(pp)
        + icm*np.sin(pp)*np.sin(p+pm))/np.pi)
    return pot2

# Resonator
f_0 = 6.8e9
C_r = 1/(2*np.pi*50*f_0)
L_r = 50*50*C_r

# Range of values for the beta ratio
beta_start = 1
beta_stop = 7
beta_values = np.linspace(beta_start, beta_stop, 21) #

df = []

for beta in beta_values:

    betap = beta*2
    betam = 0

    # Critical current for fixed beta and L
    icp = np.pi*E_l*betap/phi_0
    icm = np.pi*E_l*betam/phi_0
    Ic_1 = (icp+icm)*0.5

```

```

Ic_2 = (icp-icm)*0.5

#Fluxes and phase values
n = 500
p = np.linspace(-2*np.pi, 2*np.pi, n)
pp_values = np.linspace(-np.pi, np.pi, n)
pm = 0
f_res = []

for i,pp in enumerate(pp_values):
    U = u(p,icp,icm,pp,pm)
    min_ind, _ = find_peaks(-U, distance=1)
    min_p = p[min_ind]
    min_u = u(min_p,icp,icm,pp,pm)
    f_0_ar = []

    for p_min in min_p:
        L = pow(phi_0/(2*np.pi),2)/(duddp(p_min,icp,icm,pp,pm))
        f_0 = 1/(2*np.pi*pow((L_r + L)*C_r,1/2))*1e-9
        f_0_ar.append(f_0)

    f_res.append(np.array(f_0_ar))
nf = 201 #Grid thickness
f_sort = [np.sort(item) for item in f_res]
f_values = np.linspace(6.0,6.8,nf)
f_graph = np.zeros((pp_values.size,f_values.size))

for o,item in enumerate(f_res):
    for y,elem in enumerate(item):
        index = np.where(f_values > elem)[0][0]
        f_graph[o,index] = y+1

pp_mesh,f_mesh = np.meshgrid(pp_values,f_values)

#First arch height
try:
    f_p_pi = max(np.array([f_values
                           [np.where(f_graph[0,:])

```



```
f_p_0 = max(np.array([f_values
                    [np.where(f_graph[int(n/2),:]
                               ==1)[0][0]]
                    ,f_values
                    [np.where(f_graph[int(n/2),:]
                               ==2)[0][0]]]))

except:
    try:
        f_p_0 = f_values[np.where(f_graph[int(n/2),:]
                                   ==1)[0][0]]

    except:
        f_p_0 = f_values[np.where(f_graph[int(n/2),:]
                                   ==2)[0][0]]

delta_freq = f_p_0 - f_p_pi
df.append(delta_freq)
print(beta)
print(delta_freq)

plt.figure()
plt.scatter(beta_values, np.array(df)*1e+3)
plt.ylabel(r"$\Delta f$ " + " $[MHz]$", size = 25)
plt.xlabel(r'$\beta$', size = 25)
plt.rc('xtick', labels=20)
plt.rc('ytick', labels=20)
```

---

# Bibliography

- [1] F. Arute, K. Arya, R. Babbush, D. Bacon, J. C. Bardin, R. Barends, R. Biswas, S. Boixo, F. G. Brandao, D. A. Buell, *et al.*, “Quantum supremacy using a programmable superconducting processor,” *Nature*, vol. 574, no. 7779, pp. 505–510, 2019.
- [2] M. H. Devoret and R. J. Schoelkopf, “Superconducting circuits for quantum information: an outlook,” *Science*, vol. 339, no. 6124, pp. 1169–1174, 2013.
- [3] K. K. Likharev and V. K. Semenov, “Rsfq logic/memory family: A new josephson-junction technology for sub-terahertz-clock-frequency digital systems,” *IEEE Transactions on Applied Superconductivity*, vol. 1, no. 1, pp. 3–28, 1991.
- [4] P. Bunyk, K. Likharev, and D. Zinoviev, “Rsfq technology: Physics and devices,” *International journal of high speed electronics and systems*, vol. 11, no. 01, pp. 257–305, 2001.
- [5] O. A. Mukhanov, “Energy-efficient single flux quantum technology,” *IEEE Transactions on Applied Superconductivity*, vol. 21, no. 3, pp. 760–769, 2011.
- [6] R. McDermott, M. Vavilov, B. Plourde, F. Wilhelm, P. Liebermann, O. Mukhanov, and T. Ohki, “Quantum–classical interface based on single flux quantum digital logic,” *Quantum science and technology*, vol. 3, no. 2, p. 024004, 2018.
- [7] J. Preskill, “Fault-tolerant quantum computation,” in *Introduction to quantum computation and information*, pp. 213–269, World Scientific, 1998.
- [8] M. Tinkham, *Introduction to Superconductivity*. International series in pure and applied physics, McGraw Hill, 1996.
- [9] T. Heikkilä, *The Physics of Nanoelectronics: Transport and Fluctuation Phenomena at Low Temperatures*. Oxford Master Series in Physics, OUP Oxford, 2013.
- [10] J. M. Martinis, “Superconducting phase qubits,” *Quantum Information Processing*, vol. 8, no. 2, pp. 81–103, 2009.

- [11] E. Lucero, R. Barends, Y. Chen, J. Kelly, M. Mariantoni, A. Megrant, P. O'Malley, D. Sank, A. Vainsencher, J. Wenner, *et al.*, "Computing prime factors with a josephson phase qubit quantum processor," *Nature Physics*, vol. 8, no. 10, pp. 719–723, 2012.
- [12] M. D. Reed, L. DiCarlo, B. R. Johnson, L. Sun, D. I. Schuster, L. Frunzio, and R. Schoelkopf, "High-fidelity readout in circuit quantum electrodynamics using the jaynes-cummings nonlinearity," *Physical Review Letters*, vol. 105, Oct 2010.
- [13] X. Gu, A. F. Kockum, A. Miranowicz, Y.-x. Liu, and F. Nori, "Microwave photonics with superconducting quantum circuits," *Physics Reports*, vol. 718-719, p. 1–102, Nov 2017.
- [14] A. Opremcak, I. Pechenezhskiy, C. Howington, B. Christensen, M. Beck, E. Leonard, J. Suttle, C. Wilen, K. Nesterov, G. Ribeill, *et al.*, "Measurement of a superconducting qubit with a microwave photon counter," *Science*, vol. 361, no. 6408, pp. 1239–1242, 2018.
- [15] J. Aumentado, "Superconducting parametric amplifiers: The state of the art in josephson parametric amplifiers," *IEEE Microwave Magazine*, vol. 21, no. 8, pp. 45–59, 2020.
- [16] U. Vool and M. Devoret, "Introduction to quantum electromagnetic circuits," *International Journal of Circuit Theory and Applications*, vol. 45, no. 7, pp. 897–934, 2017.
- [17] C. Poole, H. Farach, R. Creswick, and R. Prozorov, *Superconductivity*. Elsevier Science, 2010.
- [18] A. S. Kristian Fossheim, *Front Matter*. John Wiley and Sons, Ltd, 2004.
- [19] R. Kleiner, W. Buckel, and R. Huebener, *Superconductivity: An Introduction*. Wiley, 2016.
- [20] F. Tafuri, *Fundamentals and Frontiers of the Josephson Effect*, vol. 286. Springer Nature, 2019.
- [21] A. Barone and G. Paternò, *Weak Superconductivity — Phenomenological Aspects*. John Wiley and Sons, Ltd, 1982.
- [22] *Dynamics of Josephson Junctions and Circuits*. Taylor & Francis, 1986.

- [23] M. Kjaergaard, M. E. Schwartz, J. Braumüller, P. Krantz, J. I.-J. Wang, S. Gustavsson, and W. D. Oliver, “Superconducting qubits: Current state of play,” *Annual Review of Condensed Matter Physics*, vol. 11, pp. 369–395, 2020.
- [24] D. P. DiVincenzo, “The physical implementation of quantum computation,” *Fortschritte der Physik*, vol. 48, p. 771–783, Sep 2000.
- [25] P. Krantz, M. Kjaergaard, F. Yan, T. P. Orlando, S. Gustavsson, and W. D. Oliver, “A quantum engineer’s guide to superconducting qubits,” *Applied Physics Reviews*, vol. 6, no. 2, p. 021318, 2019.
- [26] M. A. Nielsen and I. L. Chuang, *Quantum Computation and Quantum Information: 10th Anniversary Edition*. USA: Cambridge University Press, 10th ed., 2011.
- [27] M. H. Devoret, A. Wallraff, and J. M. Martinis, “Superconducting qubits: A short review,” *arXiv preprint cond-mat/0411174*, 2004.
- [28] W. D. Oliver and P. B. Welander, “Materials in superconducting quantum bits,” *MRS Bulletin*, vol. 38, no. 10, p. 816–825, 2013.
- [29] N. Didier, E. A. Sete, M. P. da Silva, and C. Rigetti, “Analytical modeling of parametrically modulated transmon qubits,” *Physical Review A*, vol. 97, no. 2, p. 022330, 2018.
- [30] J. Koch, T. M. Yu, J. Gambetta, A. A. Houck, D. I. Schuster, J. Majer, A. Blais, M. H. Devoret, S. M. Girvin, and R. J. Schoelkopf, “Charge-insensitive qubit design derived from the cooper pair box,” *Physical Review A*, vol. 76, Oct 2007.
- [31] L. S. Bishop, *Circuit quantum electrodynamics*. Yale University, 2010.
- [32] J. Preskill, “Fault-tolerant quantum computation,” in *Introduction to quantum computation and information*, pp. 213–269, World Scientific, 1998.
- [33] H. M. Wiseman and G. J. Milburn, *Quantum measurement and control*. Cambridge university press, 2009.
- [34] D. M. Pozar, *Microwave engineering; 3rd ed.* Hoboken, NJ: Wiley, 2005.
- [35] C. J. Howington, “Digital readout and control of a superconducting qubit,” 2019.
- [36] A. Wallraff, D. I. Schuster, A. Blais, L. Frunzio, R.-S. Huang, J. Majer, S. Kumar, S. M. Girvin, and R. J. Schoelkopf, “Strong coupling of a single photon

- to a superconducting qubit using circuit quantum electrodynamics,” *Nature*, vol. 431, p. 162–167, Sep 2004.
- [37] L. S. Bishop, J. M. Chow, J. Koch, A. A. Houck, M. H. Devoret, E. Thuneberg, S. M. Girvin, and R. J. Schoelkopf, “Nonlinear response of the vacuum rabi resonance,” *Nature Physics*, vol. 5, p. 105–109, Dec 2008.
- [38] Y.-x. Liu, C. P. Sun, and F. Nori, “Scalable superconducting qubit circuits using dressed states,” *Physical Review A*, vol. 74, Nov 2006.
- [39] M. A. Sillanpää, J. I. Park, and R. W. Simmonds, “Coherent quantum state storage and transfer between two phase qubits via a resonant cavity,” *Nature*, vol. 449, p. 438–442, Sep 2007.
- [40] L. C. G. Govia, E. J. Pritchett, S. T. Merkel, D. Pineau, and F. K. Wilhelm, “Theory of josephson photomultipliers: Optimal working conditions and back action,” *Physical Review A*, vol. 86, Sep 2012.
- [41] M. Asif Khan, A. Bhattarai, J. Kuznia, and D. Olson, “High electron mobility transistor based on a gan-al x gal- x n heterojunction,” *Applied Physics Letters*, vol. 63, no. 9, pp. 1214–1215, 1993.
- [42] T.-K. Nguyen, C.-H. Kim, G.-J. Ihm, M.-S. Yang, and S.-G. Lee, “Cmos low-noise amplifier design optimization techniques,” *IEEE Transactions on Microwave Theory and Techniques*, vol. 52, no. 5, pp. 1433–1442, 2004.
- [43] Y.-C. Liang, Y.-H. Yeh, P. E. M. F. Mendonça, R. Y. Teh, M. D. Reid, and P. D. Drummond, “Quantum fidelity measures for mixed states,” *Reports on Progress in Physics*, vol. 82, p. 076001, Jun 2019.
- [44] Y. Harada, E. Goto, and N. Miyamoto, “Quantum flux parametron,” in *1987 International Electron Devices Meeting*, pp. 389–392, IEEE, 1987.
- [45] J. Majer, J. Chow, J. Gambetta, J. Koch, B. Johnson, J. Schreier, L. Frunzio, D. Schuster, A. A. Houck, A. Wallraff, *et al.*, “Coupling superconducting qubits via a cavity bus,” *Nature*, vol. 449, no. 7161, pp. 443–447, 2007.
- [46] A. Blais, R.-S. Huang, A. Wallraff, S. M. Girvin, and R. J. Schoelkopf, “Cavity quantum electrodynamics for superconducting electrical circuits: An architecture for quantum computation,” *Physical Review A*, vol. 69, no. 6, p. 062320, 2004.
- [47] “Rohde and schwarz vector network analyzer: Operating manual,”

- [48] T. Davis and E. Natarajan, "Algorithm 907: Klu, a direct sparse solver for circuit simulation problems.," *ACM Trans. Math. Softw.*, vol. 37, 01 2010.
- [49] S. V. Polonsky, V. K. Semenov, and P. N. Shevchenko, "PSCAN: personal superconductor circuit analyser," *Superconductor Science and Technology*, vol. 4, pp. 667–670, nov 1991.
- [50] S. Polonsky, P. Shevchenko, A. Kirichenko, D. Zinoviev, and A. Rylyakov, "Pscan'96: New software for simulation and optimization of complex rsfq circuits," *IEEE transactions on applied superconductivity*, vol. 7, no. 2, pp. 2685–2689, 1997.
- [51] N. R. Werthamer, "Nonlinear self-coupling of josephson radiation in superconducting tunnel junctions," *Phys. Rev.*, vol. 147, pp. 255–263, Jul 1966.
- [52] A. Odintsov, V. Semenov, and A. Zorin, "Specific problems of numerical analysis of the josephson junction circuits," *IEEE Transactions on Magnetics*, vol. 23, no. 2, pp. 763–766, 1987.
- [53] M. Brinson and V. Kuznetsov, "Qucs-0.0.19s: A new open-source circuit simulator and its application for hardware design," in *2016 International Siberian Conference on Control and Communications (SIBCON)*, pp. 1–5, May 2016.
- [54] M. E. Brinson and V. Kuznetsov, "Extended behavioural device modelling and circuit simulation with qucs-s," *International Journal of Electronics*, vol. 0, no. 0, pp. 1–14, 2017.
- [55] R. N. Simons, *Coplanar Waveguide Circuits, Components, and Systems*. Wiley series in microwave and optical engineering, Newark, NJ: Wiley, 2001.
- [56] M. Goppl, A. Fragner, M. Baur, R. Bianchetti, S. Filipp, J. Fink, P. Leek, G. Puebla, L. Steffen, and A. Wallraff, "Coplanar waveguide resonators for circuit quantum electrodynamics," *Journal of Applied Physics*, vol. 104, pp. 113904 – 113904, 01 2009.
- [57] A. Megrant, C. Neill, R. Barends, B. Chiaro, Y. Chen, L. Feigl, J. Kelly, E. Lucero, M. Mariantoni, P. J. J. O'Malley, and et al., "Planar superconducting resonators with internal quality factors above one million," *Applied Physics Letters*, vol. 100, p. 113510, Mar 2012.
- [58] K. J. Latimer, J. W. Evans, M. A. Cowell, and P. K. Wright, "Modeling of interdigitated electrodes and supercapacitors with porous interdigitated electrodes," *Journal of The Electrochemical Society*, vol. 164, no. 4, pp. A930–A936, 2017.

- 
- [59] O. Kamigaito, “Circuit-model formulas for external-q factor of resonant cavities with capacitive and inductive coupling,” 2020.
- [60] R. Igreja and C. Dias, “Analytical evaluation of the interdigital electrodes capacitance for a multi-layered structure,” *Sensors and Actuators A: Physical*, vol. 112, no. 2, pp. 291–301, 2004.